Ion Coulomb crystals: An exotic form of condensed matter

Giovanna Morigi

Theoretische Physik, Universität des Saarlandes, D-66123 Saarbrücken, Germany

John Bollinger

Time and Frequency Division, National Institute of Standards and Technology, Boulder, Colorado, USA

Michael Drewsen

Department of Physics and Astronomy, University of Aarhus, Aarhus, Denmark

Daniel Podolsky

Department of Physics, Technion, Haifa 32000, Israel

Efrat Shimshoni

Department of Physics, Bar-Ilan University, Ramat-Gan 52900, Israel

(published 5 August 2026)

Ion Coulomb crystals are ordered structures formed by laser-cooled ions in traps that are characterized by interparticle distances of several micrometers and energy scales on the order of μeV. Their crystalline structure emerges from the interplay between Coulomb repulsion and the external confining potential, which can be readily tuned. Moreover, individual ions can be precisely manipulated with lasers and imaged via resonance fluorescence. These unusual and unique properties make ion crystals a powerful platform for studying phases of matter in the strongly correlated regime and at low temperatures where their dynamics is manifestly quantum mechanical. This review examines the theoretical framework and experimental characterization of ion Coulomb crystals from a condensed-matter perspective. Their dynamical and thermodynamic properties are discussed in one, two, and three dimensions, and recent investigations into their out-of-equilibrium behavior are reviewed. An outlook on future directions for exploring novel condensed-matter phenomena with trapped-ion crystals, as well as for exploiting these features for scientific and technical applications, is provided.

DOI: 10.1103/tn8k-r4w8

CONTENTS

I. Introduction 1
A. Historical framework and conditions for crystallization 2
B. Ion Coulomb crystals in a laboratory 3
1. rf trap 3
2. Penning trap 6
C. Laser cooling 8
D. Ion-trap arrays and optical dipole traps 9
II. Ion Coulomb Crystals: From One to Three Dimensions 10
A. Linear geometries: The ion chain 10
1. Ground-state configuration 10
2. Normal modes of the ion chain 11
3. Thermodynamics of the ion chain 13
4. The linear-zigzag transition 14
5. The quantum linear-zigzag transition 17
B. Planar geometries 20
1. Trap configurations 20
2. Ground-state configuration 21
3. Normal modes 22
4. Structural instability of the planar geometry 24
C. Three-dimensional crystals 26
1. Ground-state configuration 26
2. Metastable and perturbation-induced structures 30
3. Normal modes of three-dimensional crystals 32
III. Out-of-Equilibrium Dynamics of Ion Coulomb Crystals 34
A. Equilibrium and temperature 35
B. Transport in trapped-ion chains 36
C. Topological defects and metastability 37
D. Slow quenches and the Kibble-Zurek mechanism 39
E. Stick-slip motion and nanofriction 40
F. Kink dynamics and quantum sliding 43
IV. Concluding Remarks and Outlook 45
Acknowledgments 46
Data Availability 46
References 46

I. INTRODUCTION

In a seminal article from 1934, Eugene Wigner predicted that conduction electrons in a metal at low densities can

crystallize (Wigner, 1934). This is a peculiar situation in condensed matter, where otherwise crystallization is expected at high densities, and it results from the decay of the Coulomb interactions as the inverse of the interparticle distance a. For this reason, in an unscreened environment, the Coulomb interactions scale with the charge density $n \sim a^{-3}$ as $E_{\rm pot} \sim n^{1/3}$. By comparison, the typical scale of the kinetic energy in a degenerate free electron gas is $E_{\rm kin} \sim h^2/2ma^2 \sim n^{2/3}$ (Kittel, 1991). As a result, at low densities the Coulomb interactions are dominant over the kinetic energy, leading to crystallization. More generally, at low densities the Wigner crystal phase is favored regardless of the particle statistics since the overlap of single-particle wave functions is small.

Wigner crystallization, here broadly defined as the formation of ordered arrays of particles that interact through Coulomb repulsion, can occur in a variety of systems. It is expected to occur in the interior of white dwarfs and in the outer crust of neutron stars (Van Horn, 1991). It has been experimentally observed with electrons trapped on the surface of liquid helium (Grimes and Adams, 1980) and in low-dimensional solid-state devices including GaAs/GaAlAs heterojunctions (Andrei *et al.*, 1988) and carbon nanotubes (Shapir *et al.*, 2019). The stability of Wigner crystalline islands formed in quantum dots was analyzed by Koulakov and Shklovskii (1998); Wigner molecular crystals have been reported in semiconductor moiré superlattices (Yannouleas and Landman, 2007; Li *et al.*, 2024). Ordered arrays of charged solid particles have been experimentally studied with dusty plasmas (Thomas *et al.*, 1994; Piacente, Peeters, and Betouras, 2004; Liu and Goree, 2005) and colloidal suspensions of polystyrene spheres in water (Van Winkle and Murray, 1986; Bechinger, Brunner, and Leiderer, 2001). Wigner crystallization is being pursued through the formation of ultracold neutral plasmas of atomic ions immersed in a background of photoionized electrons (Bergeson *et al.*, 2019; Langin, Gorman, and Killian, 2019). In many of these examples, the Coulomb repulsion of the charged objects is screened by a polarizing medium in which the objects are suspended.

Wigner crystallization has also been observed in the laboratory through laser cooling of atomic and molecular ions stored in radio frequency (rf) Paul traps (Diedrich *et al.*, 1987; Wineland *et al.*, 1987; Drewsen *et al.*, 1998), in Penning traps (Gilbert, Bollinger, and Wineland, 1988), and in ion storage rings (Birkl, Kassner, and Walther, 1992). From the point of view of many-body physics, Wigner crystals of trapped ions are unusual examples of solid phases with interparticle distances of ∼5–10 μm and energy scales below ∼1 μeV (∼10 mK). Crystallization is the result of the interplay between the Coulomb repulsion and the trap potential, and the crystal's properties are significantly influenced by the confining environment. The ions interact via the unscreened long-range Coulomb repulsion, giving rise to dynamical and thermodynamical properties that differ from those of typical crystals in condensed matter. This unconventional condensed phase is the focus of this review.

Wigner crystals of trapped ions, often called ion Coulomb crystals, have been acquiring increasing importance for quantum technological applications (Häffner, Roos, and Blatt, 2008; Blatt and Roos, 2012; Bruzewicz *et al.*, 2019; Monroe *et al.*, 2021) thanks to advances in cooling and trapping (Eschner *et al.*, 2003; Johanning, Varón, and Wunderlich, 2009; Schneider, Porras, and Schaetz, 2012). These advances rely on a detailed knowledge and experimental control of the microscopic dynamics of these strongly correlated phases of matter (Johanning, Varón, and Wunderlich, 2009; Schneider, Porras, and Schaetz, 2012). This review reports on the progress on the characterization of the equilibrium and out-of-equilibrium dynamics of ion Coulomb crystals, which has enabled this progress and has, in turn, unveiled the properties of an exotic form of condensed matter.

Our starting point is the knowledge summarized in the review by Dubin and O'Neil (1999) on the plasma phase and its transition to crystallization. We set our focus on the crystallized phase and discuss the insights gained over two decades of theoretical and experimental investigations. The content complements recent overviews on ion Coulomb crystals (Drewsen, 2015; Thompson, 2015) and a wide-ranging review on strongly coupled Coulomb systems (Mihalcea *et al.*, 2023).

A. Historical framework and conditions for crystallization

In 1977, Malmberg and O'Neil explained how collections of a single species of trapped charges (ions or electrons) are ideal one-component plasmas (OCPs) (Malmberg and O'Neil, 1977). OCPs have been the subject of detailed theoretical investigations for understanding correlations in a diverse range of physical systems (Brush, Sahlin, and Teller, 1966; Baus and Hansen, 1980; Ichimaru, 1982; Ichimaru, Iyetomi, and Tanaka, 1987). They consist of a collection of identical point charges that interact through Coulomb repulsion and are immersed in a uniform neutralizing background of given density n_0 that is assumed to be continuous and nonpolarizable. In equilibrium the point charges match their density to that of the neutralizing background. Malmberg and O'Neil showed that the forces that confine ions in a Penning trap are mathematically equivalent to a uniform neutralizing background. More specifically, in a frame rotating with the collection of ions (or electrons) confined in a Penning trap (see Sec. I.B.2), the static thermodynamic properties of the trapped ions are the same as those for an OCP. The argument can be straightforwardly extended to ions confined in radio frequency traps in the so-called pseudopotential approximation; see Sec. I.B.1.

The thermodynamic properties of the classical OCP are determined by a single dimensionless parameter, typically called the Coulomb coupling constant Γ, defined by

$$\Gamma \equiv \frac{1}{4\pi\epsilon_0}\frac{Q^2}{a_{\rm WS}k_{\rm B}T}. \tag{1}$$

In Eq. (1) ϵ_0 is the permittivity of the vacuum, Q is the charge of the ion, T is the temperature of the ion, $k_{\rm B}$ is Boltzmann's constant, and $a_{\rm WS}$ is the Wigner-Seitz radius, which is determined by the neutralizing background density n_0 through the relation

$$\tfrac{4}{3}\pi a_{\mathrm{WS}}^3 = 1/n_0. \tag{2}$$

The coupling constant Γ is a measure of the ratio of the Coulomb potential energy between nearest-neighbor ions (or, more generally, point charges) to the average kinetic energy of an ion and is sufficient to determine the phase of an OCP in three dimensions. Plasmas with $\Gamma > 1$ are called strongly coupled. For a bulk (that is, infinite) OCP, the onset of fluidlike behavior, which is characterized by short-range oscillations in the pair correlation function, is predicted at $\Gamma \sim 2$. These oscillations become more pronounced with increasing Γ, and the system is predicted to undergo a first-order, liquid-solid phase transition to a body-centered-cubic lattice at a critical Γ (Pollock and Hansen, 1973; Slattery, Doolen, and DeWitt, 1982; Ogata and Ichimaru, 1987; Dubin, 1990). The best estimates of Γ_{crit} lie in the range $\Gamma_{\mathrm{crit}} \approx$ 173–175 (Farouki and Hamaguchi, 1993; DeWitt and Slattery, 1999; Dubin and O'Neil, 1999; Potekhin and Chabrier, 2000).

The classical OCP in two dimensions consists of systems of point charges that interact with the $1/r$ Coulomb repulsion but are restricted to move on a plane in a neutralizing background. The coupling constant Γ is now determined using the Wigner-Seitz radius in two dimensions, which is given by $a_{\mathrm{WS,2D}} = (\pi n)^{-1/2}$, where n is now the number of point charges per unit area. Here a liquid-solid phase transition at $\Gamma \approx 131(7)$ was measured (Grimes and Adams, 1980), in agreement with theory (Gann, Chakravarty, and Chester, 1979). We note that the Mermin-Wagner theorem (Mermin and Wagner, 1966; Hohenberg, 1967), which prohibits full-fledged crystallization in two and fewer dimensions, does not apply for unscreened Coulomb repulsion, where the energy is nonadditive and the interactions stabilize the ordered structure against fluctuations (Campa, Dauxois, and Ruffo, 2009).

In ion Coulomb crystals, kinetic energy can be reduced through laser cooling, thus increasing the coupling constant Γ to achieve crystallization. The dimensionality of the crystal is determined by the relative strength of the confinement of the trap in different directions. In this way ordered structures can be realized that are one, two, or three dimensional. Moreover, the transition between structures of different dimensions can be experimentally studied by adjusting the relative strength of the confining potential in different directions. See Secs. II.A.4 and II.B.4 for a detailed discussion.

The temperature required for crystallization can be estimated from Eq. (1). We take the three-dimensional case and use typical trapped-ion densities of 10^{15} m^{-3} and $T = 1$ K as a reference,

$$\Gamma \approx 2.69 Z^2 \left(\frac{n_0}{10^{15}\ \mathrm{m}^{-3}}\right)^{1/3} \left(\frac{T}{1\ \mathrm{K}}\right)^{-1}, \tag{3}$$

where Z is the charge (in units of elementary charges) of the trapped ion. For singly charged ions ($Z = 1$), the critical coupling parameter $\Gamma_{\mathrm{crit}} \approx 174$ for the predicted liquid-solid phase transition for a bulk OCP is obtained with temperatures of ~15 mK, which is more than 1 order of magnitude higher than the limit of conventional laser-cooling techniques (so-called Doppler laser cooling; see Sec. I.C).

We emphasize that, owing to the long-range nature of the Coulomb interactions, boundary effects can significantly affect the resulting spatial correlations. For example, theoretical calculations indicate that observing a body-centered-cubic structure predicted for the bulk OCP may require $N > 10^5$ ions (Dubin, 1989; Hasse and Avilov, 1991; Tan *et al.*, 1995); see Sec. II.C.1.

Temperatures close to the quantum zero-point motion can be reached with more refined laser-cooling techniques; see Sec. I.C. In this regime the crystals' vibrations are quantum mechanical, but the ground-state configuration is classical to a good approximation since the typical ion densities are far from the conditions at which quantum fluctuations can melt the crystal. We now provide an estimate for the density required to melt an ion Coulomb crystal and note that this estimate is closely related to the problem of tunneling in a two-ion-crystal chain (Yin and Javanainen, 1995). With the ion plasma frequency defined as $\omega_p = (Q^2 n_0/\epsilon_0 m)^{1/2}$, an approximate estimate of the zero-point energy of an ion localized in the crystalline phase is $\hbar\omega_p/2$. Quantum melting is expected to occur when

$$\frac{\hbar\omega_p}{2} \gtrsim \frac{1}{4\pi\epsilon_0}\frac{Q^2}{a_{\mathrm{WS}}}, \tag{4}$$

where the right-hand side provides an estimate of the energy barrier impeding an ion from hopping to the neighboring sites of the Wigner crystal. Equation (4) sets an upper bound on the mean interparticle distance (here expressed in terms of a_{WS}) for the ion crystal to melt,

$$a_{\mathrm{WS}} \lesssim \frac{\hbar^2}{mQ^2/(4\pi\epsilon_0)}. \tag{5}$$

Maximum densities that can be achieved in current rf or Penning traps are less than 10^{16} m^{-3}, resulting in Wigner-Seitz radii a_{WS} that are orders of magnitude larger than the criteria set by Eq. (5). Recent proposals and experimental efforts for unveiling manifestations of the quantum statistics of trapped ions utilize highly symmetric ion crystals in a ring-trap geometry to attempt to realize an effective particle exchange operator, thereby measuring the symmetry of the wave function (Noguchi *et al.*, 2014; Li *et al.*, 2017; Roos *et al.*, 2017; Urban *et al.*, 2019).

B. Ion Coulomb crystals in a laboratory

It is not possible to disentangle any discussion on ion Coulomb crystals from their environment, the ion trap. Confining one-component plasmas in a laboratory requires one to either apply oscillating electric fields or combine static electric and magnetic fields. Equilibrium, in the thermodynamic sense, can be challenging to achieve; see Sec. III.A. We now review the basics of Paul (or rf) and Penning traps, which are the most frequently used experimental platforms.

1. rf trap

According to Earnshaw's theorem (Earnshaw, 1842), it is impossible to confine charged particles in vacuum exclusively

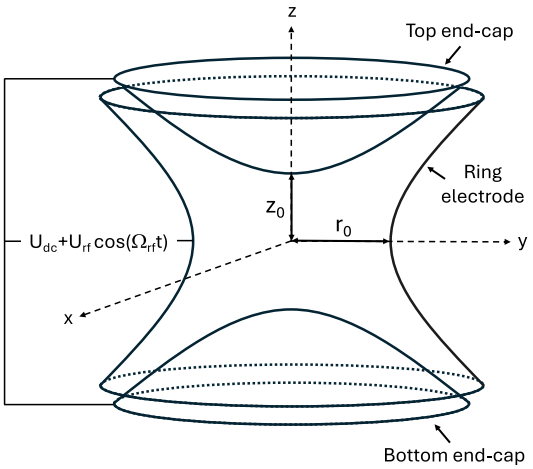

FIG. 1. Schematics of the standard three-dimensional rf trap (Paul trap). The trap consists of a central ring electrode and two so-called end-cap electrodes (with the top and bottom end-caps marked appropriately). All three electrodes have hyperboloid-shaped surfaces surrounding the trap center. They produce an electrical quadrupole field when the voltage difference $U_{\rm dc} + U_{\rm rf}\cos(\Omega_{\rm rf}t)$ is applied between the ring and the end caps. The strength of the quadrupole field depends on the distances r_0 and z_0. A perfect quadrupole field is generated when $r_0 = \sqrt{2}z_0$.

by static electric fields generated from voltages applied to external electrodes. However, by introducing time-varying electric fields, it is possible to realize spatially localized minima of the effective potential energy. For atomic and not particularly heavy molecular species, fields in the rf regime are most often applied to achieve strong confining forces as well as deep effective trap potentials, as we later detail. Hence, such traps are often referred to as rf traps.

The standard rf trap is named after Nobel Prize laureate Wolfgang Paul, who invented the principle for two-dimensional confinement (Paul and Steinwedel, 1953). It is sketched in Fig. 1 and is based on three electrodes machined to have three-dimensional hyperbolic surfaces in order to create the perfect boundary conditions for an electrical quadrupole field with respect to the line of cylindrical symmetry of the electrodes (the z axis in Fig. 1). With reference to the parameters defined in Fig. 1, the time-dependent electrical potential in the cylindrical coordinates reads

$$\phi(z,\rho,t) = \frac{1}{2}[U_{\rm dc} + U_{\rm rf}\cos(\Omega_{\rm rf}t)]\frac{2z^2-\rho^2}{r_0^2}, \qquad (6)$$

where $\rho = \sqrt{x^2+y^2}$ is the distance from the symmetry axis. Newton's equations of motion for a single charged particle read

$$\frac{d^2u}{d\tau^2} + [a_u - 2q_u\cos(2\tau)]u = 0 \qquad (u = z,\rho), \qquad (7)$$

with the dimensionless parameters

$$\tau = \frac{\Omega_{\rm rf}}{2}t, \qquad (8)$$

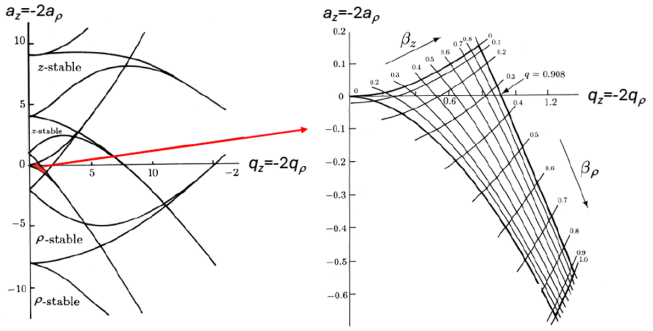

FIG. 2. Stability diagrams for a standard rf trap. Left panel: diagram showing that the confined motion of a charged particle can happen only when its stability parameters $a_{z,\rho}$ and $q_{z,\rho}$ lie within common areas of stable motion (that is, they are z and ρ stable). Right panel:enlargement of the largest area of common stability (marked in red in the left panel). The parameters β_j represent the ratio between the main motional frequencies of the trapped particle along the j direction ($j = z,\rho$) and the rf frequency $\Omega_{\rm rf}/2$. From Ghosh, 1995.

$$a_z = -2a_\rho = \frac{4QU_{\rm dc}}{mz_0^2\Omega_{\rm rf}^2}, \qquad (9)$$

$$q_z = -2q_\rho = \frac{2QU_{\rm rf}}{mr_0^2\Omega_{\rm rf}^2}. \qquad (10)$$

Equation (7) provides examples of the so-called Mathieu equations. They can lead to spatially confined motion whenever the parameters $a = |a_u|$ and $q = |q_u|$ lie within the areas of combined stability, as illustrated in Fig. 2. The motion within this so-called stability diagram is generally complex. However, for $a, q \ll 1$ the solution to the equation of motion can be well approximated by the trajectory

$$u(t) = u_0\left(1 - \frac{q_u}{2}\cos(\Omega_{\rm rf}t)\right)\cos(\omega_u t), \qquad (11)$$

with ω_u given by

$$\omega_u = \frac{1}{2}\sqrt{a_u + \frac{q_u^2}{2}}\Omega_{\rm rf}. \qquad (12)$$

Equation (11) describes harmonic motion at frequencies $\omega_{z,\rho}$ superimposed with a much faster quiver motion at $\Omega_{\rm rf}$. The quiver motion is often referred to as *micromotion* and has a small amplitude proportional to the distance of the harmonic (secular) motion from the origin; see Fig. 3. In many experimental situations, one can neglect the micromotion and is essentially left with pure harmonic motion. In such situations the term proportional to q_u in Eq. (11) can be discarded, and one assigns a potential energy to the trap, often referred to as the *pseudopotential*, which reads

$$\phi_{\rm pseu}(z,\rho) = \tfrac{1}{2}m(\omega_z^2 z^2 + \omega_\rho^2\rho^2). \qquad (13)$$

The types of rf traps most used in experiments with ion Coulomb crystals are linear quadrupole rf traps (Prestage,

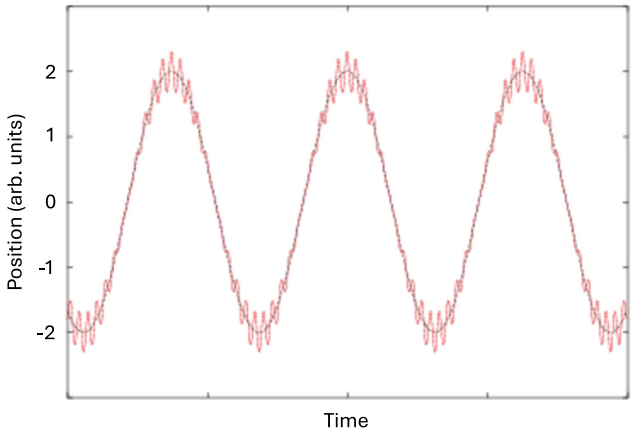

FIG. 3. Motion of a trapped particle in a standard rf trap. The trajectory of a trapped ion along one of the principal directions (x, y, z) is shown for $a_z = 0.0$ and $q_z = 0.3$. The oscillatory solid red curve represents the full solution to Eq. (7), while the dashed dark blue curve is the solution obtained using the harmonic pseudopotential of Eq. (13). The difference between the two curves is the so-called micromotion at the oscillation frequency Ω_{rf}.

Dick, and Maleki, 1989). Ideally, a linear quadrupole rf trap consists of four rods with hyperbolic cross sections arranged in a parallel configuration to create a perfect two-dimensional quadrupole field for confinement in the cross-section plane; see Fig. 4(a). Along the rod axis, confinement is obtained by applying dc voltages either to two additional electrodes placed along the central axis between the rods or to the eight endpieces after sectioning the rods into three pieces; see Figs. 4(b) and 4(c).

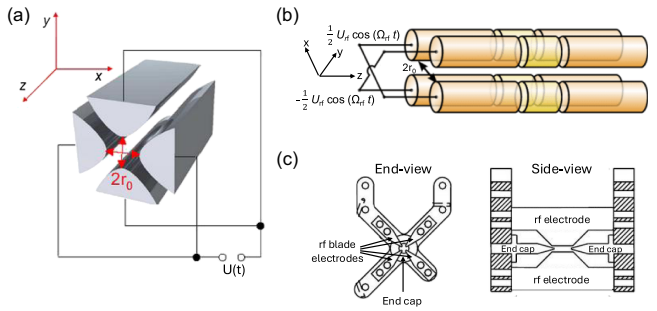

FIG. 4. Linear trap geometries. (a) Ideal electrode geometry with hyperbolic-shaped electrodes achieving two-dimensional trapping in the x-y plane via a perfect electrical quadrupole field. This ideal geometry is often used in quadrupole mass spectrometers. From Splatt, 2009. (b) Example of a three-dimensional linear rf trap with cylindrically shaped electrodes. One realizes a confinement in the x-y plane as in (a) by applying the same rf voltage to each of the three sections of the electrodes. Axial confinement along the z axis is achieved through application of the same dc voltage U_{end} to all the orange-colored electrode sections. From Poulsen, Miroshnychenko, and Drewsen, 2012. (c) Linear trap based on rf electrodes shaped like blades. This design creates a smaller effective value of r_0 and hence achieves higher trap frequencies in the x-y plane at a given rf voltage; see Eqs. (12) and (14)–(17). The built-in anharmonicity of this geometry eventually limits its use to one-dimensional ion Coulomb crystals or to small structures of two or three dimensions. From Schindler *et al.*, 2013.

For the trap geometry of Fig. 4, the equations of motion of a charged particle have the same form as Eq. (7), but now with $u = (x, y, z)$ and

$$a_z = \frac{4Q\kappa U_{\mathrm{end}}}{mr_0^2\Omega_{\mathrm{rf}}^2}, \tag{14}$$

$$a_x = \frac{4Q(U_{\mathrm{dc}} - \kappa U_{\mathrm{end}}/2)}{mr_0^2\Omega_{\mathrm{rf}}^2}, \tag{15}$$

$$a_y = \frac{4Q(-U_{\mathrm{dc}} - \kappa U_{\mathrm{end}}/2)}{mr_0^2\Omega_{\mathrm{rf}}^2}, \tag{16}$$

$$q_x = -q_y = 2\frac{QU_{\mathrm{rf}}}{mr_0^2\Omega_{\mathrm{rf}}^2}, \tag{17}$$

$$q_z = 0. \tag{18}$$

When a voltage U_{end} is applied to all eight end electrodes, U_{dc} is applied to all sections of the rods in the x-z plane and $-U_{\mathrm{dc}}$ is applied to all sections of the rods in the y-z plane. κ is a geometrical factor that depends on the length of the central section of the rods.

For $U_{\mathrm{dc}} = 0$ the stability criteria for the x and y motion become identical, and one can construct a stability diagram for $a = a_x = a_y = -a_z/2$ and q, as presented in Fig. 5. In this case, when $a, q \ll 1$, one can establish the same approximate solutions to the equation of motion as Eqs. (11) and (12) for the standard rf trap and can define a pseudopotential of the form shown in Eq. (13) with $\rho = \sqrt{x^2 + y^2}$ and $\omega_\rho = \omega_x = \omega_y$.

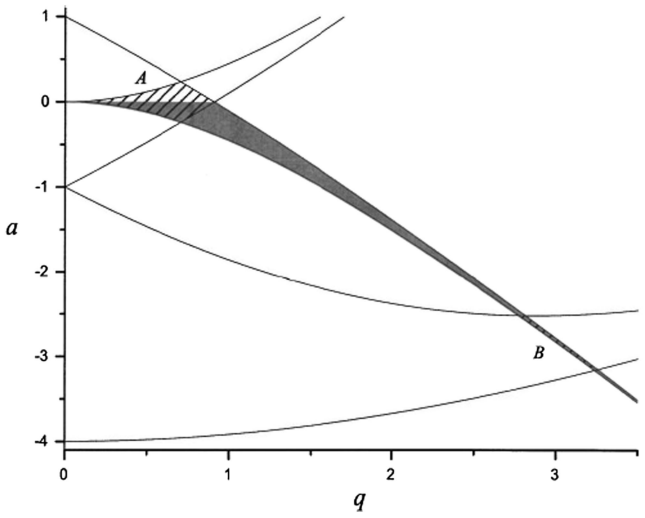

FIG. 5. Stability diagram for a linear rf trap. The gray shaded area represents the stability region for the specific case of $U_{\mathrm{dc}} = 0$, for which $a_x = a_y = a = -a_z/2$ and $q_x = -q_y = q$ according to Eqs. (14)–(17). The area of the stability diagram is significantly larger than that of the two-dimensional confinement of the quadrupole mass filter (the hatched areas A and B) and of the three-dimension stable trapping of the standard rf trap; see Fig. 2. From Drewsen and Brøner, 2000.

The fact that all quadrupole traps close to the center give rise to an effective harmonic potential is an important feature. Only such potentials will lead to a uniform particle density of three-dimensional Coulomb crystals, like traditional crystal structures known from solid-state physics. In this case, for the previously presented linear rf trap, the ion number density is given by

$$n_0 = \frac{\epsilon_0 U_{\rm rf}^2}{m r_0^4 \Omega_{\rm rf}^2}. \tag{19}$$

For trap parameters $U_{\rm rf} \sim 100$–1000 V, $r_0 \sim 1$–5 mm, and $\Omega_{\rm rf} \sim 2\pi \times 10$ MHz, one typically reaches ion densities $n_0 \sim 10^{14}$–10^{15} m^{-3}.

The linear rf trap has two obvious advantages over the standard rf trap when it comes to experiments with ion Coulomb crystals. First, this trap configuration is more open for introducing laser beams for carrying out laser cooling needed for ion crystallization; see Sec. I.C. Second, the entire line defined by the z axis is free of rf fields.

Confinement of ions in higher-order rf traps leads to new possibilities and challenges. A good review on the trapping of charged particles in multipole rf traps was given by Gerlich (1992). rf traps of order $2l$ lead in general to an effective pseudopotential of order $2l-2$, and hence to a much shallower potential than the harmonic potential, as well as to less micromotion at positions close to the trap center. The last feature has been exploited for decades in experiments involving buffer gas cooling of dilute ensembles of molecular ions (Gerlich, 1995). In the context of Coulomb crystallization, multipole traps are expected to realize three-dimensional crystals with nonuniform ion densities; see the theoretical studies of Champenois (2009) and Champenois *et al.* (2010) and the experimental realization of Okada *et al.* (2009). The current lack of high-quality experimental results is due mainly to limitations in the ability to operate perfect multipole traps. Lower-order perturbations significantly distort the effective potential, with the result of more local effective potential minima (Pedregosa-Gutierrez *et al.*, 2018). The effect of the anharmonicity in the effective potential on rf-induced heating for dense ion ensembles is still unclear.

2. Penning trap

In contrast to rf traps, Penning traps (and the closely related Penning-Malmberg traps) employ both static electric and magnetic fields to confine charged particles (Dubin and O'Neil, 1999; Vogel, 2018). A set of electrodes, frequently a coaxially aligned array of cylindrical electrodes, as sketched in Fig. 6, generates an electrostatic trap potential ϕ_T that has symmetry about the common axis of the cylinders, as denoted by the $\hat{z}$ axis. With a positive potential applied to the end cylinders relative to the central cylinder, ϕ_T provides axial confinement for positively charged ions. However, the Laplace equation $\nabla^2 \phi_T = 0$ implies that the electric field near the center of the Penning trap is anticonfining in the radial direction. Radial confinement is then obtained by immersing the trap in a strong uniform magnetic field $\mathbf{B} = B\hat{z}$ directed along the symmetry axis of the trap.

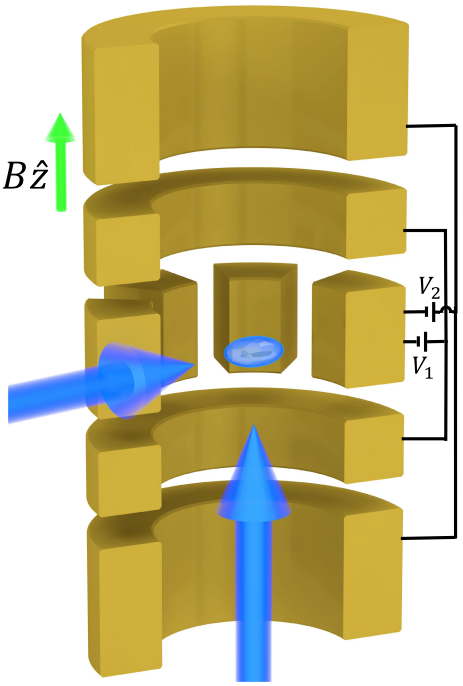

FIG. 6. Cross-section sketch of a Penning trap that employs cylindrical electrodes, similar to that used by Britton *et al.* (2012). The thick arrows represent Doppler laser-cooling beams that cool ion motion parallel and perpendicular to the magnetic field. The spheroid they are pointing at is an ion crystal in the center of the trap. For trapping of positively charged ions, the outer electrodes are biased with a positive potential with respect to the central electrode, typically with $V_2 > V_1 > 0$. The central electrode is segmented to enable the application of a rotating wall potential. See the text. Not shown are light collection optics that image ion fluorescence both parallel and perpendicular to the magnetic field.

In more detail, ions in the trap undergo an $\mathbf{E} \times \mathbf{B}$ drift that, owing to the radial electric field of the trapping potential, is a rotation of the ion crystal about the symmetry axis of the trap. Rotation in the presence of the strong axial magnetic field produces a Lorentz force directed radially inward, providing radial confinement. Theoretical and experimental work shows that, for a trap with axial symmetry and in the absence of external forces, a collection of charged particles confined in a Penning trap evolves to a thermal equilibrium state characterized by rigid rotation (Brewer *et al.*, 1988; Driscoll, Malmberg, and Fine, 1988; Dubin and O'Neil, 1999; Davidson, 2001). Throughout this review we use ω_r to denote the rotation frequency of the ion crystal. Note that the energy of an ensemble of ions in a Penning trap is lowered when the ions in the crystal move radially outward. Radial confinement in a Penning trap is therefore not an energetic confinement. It can be understood in terms of the conservation of the canonical angular momentum about the symmetry axis of the trap (Dubin and O'Neil, 1999). This motivates the construction of Penning traps with good axial symmetry.

Penning traps have been employed for mass spectroscopy and precision measurements in atomic physics for many decades. Typically, the number of trapped charges is modest and the characteristic size of the collection of charged particles

is small compared to the dimensional size of the trap electrode structure. In this case the trap potential ϕ_T can be expanded in a Taylor series about the center of the trap,

$$Q\phi_T(\rho,z) \approx \frac{1}{2}m{\omega_z}^2\left(z^2-\frac{\rho^2}{2}\right), \tag{20}$$

where z and ρ are axial and cylindrical coordinates, m is the mass of the ion, and Q is the charge of the ion. The trap frequency ω_z characterizes the strength of the axial confinement: it scales as the square root of the potential difference between the end and central electrodes and inversely with the size of the trap. For a trap with two end electrodes and one central electrode,

$$\omega_z = \sqrt{\frac{QV_0}{md_T^2}}, \tag{21}$$

where V_0 is the voltage applied between the end and central cylinders and d_T is a characteristic distance describing the trap. The volume over which Eq. (20) is a good approximation can be increased by employing trap electrodes with hyperboloid shapes (Brown and Gabrielse, 1986).

It is frequently convenient to describe the dynamics of an ion crystal in a Penning trap in a frame rotating with rotation frequency ω_r of the ion crystal. In this rotating frame, the radially deconfining trap potential of Eq. (20) turns into an effective, radially confining potential

$$Q\phi_R(x,y) = \tfrac{1}{2}m{\omega_z}^2(z^2+\beta\rho^2), \tag{22}$$

where $\beta = \omega_r(\Omega_c-\omega_r)/\omega_z^2 - 1/2$. In Eq. (22) $\Omega_c = QB/m$ is the ion cyclotron frequency and the term proportional to $\omega_r\Omega_c$ is due to the Lorentz force generated by the rotation of the ion crystal in the presence of the strong magnetic field. The parameter β, which is sometimes called the trap anisotropy parameter, characterizes the relative strength of the radial confinement compared to the axial confinement.

So-called Penning-Malmberg traps (deGrassie and Malmberg, 1977, 1980) are employed in non-neutral plasma physics for studying nonequilibrium dynamics and the transport of particles and energy across magnetic field lines, and for the long-term confinement of antimatter (Murphy and Surko, 1992; Andresen *et al.*, 2011; Gabrielse *et al.*, 2012). Here the central cylindrical section of the trap (the segmented central electrode in Fig. 6) is a cylinder whose length is large compared to its diameter. In Penning-Malmberg traps, the number of trapped charged particles can be large ($> 10^8$), filling a volume where Eq. (20) is no longer a good approximation. For a discussion of other configurations of trap electrodes, see Vogel (2018).

The formation of ion Coulomb crystals in the laboratory requires low temperatures ($T \lesssim 10$ mK). At these low temperatures, the density n_0 of an ion crystal in a Penning trap is constant and determined by the rotation frequency (SI units),

$$n_0 = \frac{2\epsilon_0}{Q^2}m\omega_r(\Omega_c-\omega_r), \tag{23}$$

where ϵ_0 is the permittivity of the vacuum. In contrast to rf traps, this result is independent of the details of the trapping potential ϕ_T. Specifically, even if the trapping potential [Eq. (20)] contains higher-order terms $(z^4, \rho^4, z^2\rho^2, \ldots)$, the three-dimensional density of the ion crystal is constant and is given by Eq. (23). The density is maximized at $\omega_r = \Omega_c/2$, known as the Brillouin density limit (Brillouin, 1945). Typical densities n_0 demonstrated in the laboratory range from 10^{13} to 10^{16} m^{-3} (Huang, Bollinger, Mitchell, Itano, and Dubin, 1998; Dubin and O'Neil, 1999).

To date, the formation of Coulomb ion crystals has been demonstrated with modest numbers of ions ($<10^6$) (Tan *et al.*, 1995; Itano *et al.*, 1998; Mavadia *et al.*, 2013; Ball *et al.*, 2019), where the dimensional size of the ion crystal is small compared to the size of the trap electrodes. In this case the quadratic trapping potential of Eq. (20) is a good approximation, resulting in some simplifications. In particular, bounded equilibrium crystals [corresponding to $\beta > 0$ in Eq. (22)] are obtained for rotation frequencies in the range

$$\omega_m < \omega_r < \Omega_c - \omega_m, \tag{24}$$

where $\omega_m = \Omega_c/2 - \sqrt{(\Omega_c/2)^2 - \omega_z^2/2}$ is usually called the magnetron frequency. It is the frequency at which a single trapped ion undergoes a circular motion about the center of the trap owing to $\mathbf{E}\times\mathbf{B}$ drift. In addition, in the limit that the uniform density ion crystal can be treated as a uniformly charged fluid (valid for ion crystals with dimensions more than a few interparticle spacings), the low-temperature equilibrium shape of the fluid (or crystal) is a uniform density spheroid with an aspect ratio $\alpha = Z_p/R_p$ determined by ω_r, Ω_c, and ω_z through the parameter β. Here $2Z_p$ is the axial extent and $2R_p$ is the diameter of the spheroid. The detailed functional dependence was discussed by Bollinger *et al.* (1993) and Dubin and O'Neil (1999) and is in good agreement with experimental measurements (Brewer *et al.*, 1988; Bollinger *et al.*, 1993).

Figure 7 illustrates the qualitative dependence of the ion-crystal density and shapes obtained as a function of the rotation frequency ω_r for fixed ω_z and Ω_c. For ω_r slightly greater than ω_m, the crystal consists of a single plane corresponding to $\alpha \approx 0$. As ω_r is increased, the radius of the ion crystal decreases owing to the increasing radial confinement and at some rotation frequency ions move out of the $z=0$ plane, forming a three-dimensional crystal. Further increases in ω_r raise the aspect ratio α as well as the ion density n_0. The largest α and highest density n_0, known as the Brillouin limit, is obtained for $\omega_r = \Omega_c/2$. For $\omega_r > \Omega_c/2$ the centrifugal acceleration weakens the radial confinement, resulting in a decreasing ion-crystal aspect ratio and ion density. For ion crystals with small numbers of ions, the radial confinement with $\omega_r \sim \Omega_c/2$ can be made sufficiently strong compared to the axial confinement such that the ions form a one-dimensional crystal along the symmetry axis of the trap (Mavadia *et al.*, 2013). These structural phase transitions [from two to three dimensions (Mitchell, Bollinger, Dubin *et al.*, 1998) and from three to one dimension (Mavadia *et al.*, 2013)] have been observed in the laboratory.

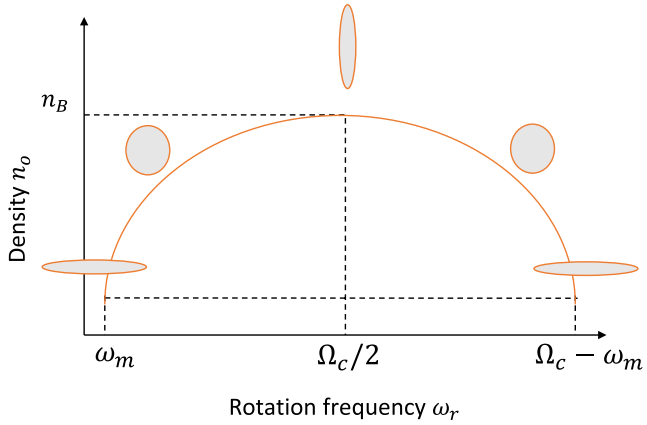

FIG. 7. Simple qualitative sketch of the ion number density n_0 and different spheroidal crystal shapes obtained as a function of the ion-crystal rotation frequency ω_r in a Penning trap. The maximum density n_B, called the Brillouin limit, occurs for $\omega_r = \Omega_c/2$.

Precise control of the ion-crystal rotation frequency ω_r is important for controlling and maintaining a stable crystal whose shape and density are constant in time. Without this control ω_r will slowly decrease in time owing to the influence of torque from small asymmetries in the confining fields of the trap. In the laboratory ω_r is precisely controlled through the use of a rotating electric field, frequently called a rotating wall. Rotating wall electric fields were first investigated by the non-neutral plasma physics community (Huang *et al.*, 1997) and then borrowed by the atomic physics ion-trap community, where its use with low-temperature ion crystals enables precise, phase-locked control of the ion-crystal rotation (Huang, Bollinger, Mitchell, and Itano, 1998; Huang, Bollinger, Mitchell, Itano, and Dubin, 1998). Rotating electric fields with different azimuthal symmetries can be employed. However, a frequently used geometry is the rotating quadrupole potential,

$$Q\phi_W(\rho,\phi,t) = \tfrac{1}{2}m\omega_W^2\rho^2\cos\left[2(\phi+\omega_r t)\right], \tag{25}$$

where ϕ is the azimuthal angle in the laboratory frame. In a frame rotating clockwise about the $\hat{z}$ axis at a frequency ω_r, Eq. (25) describes a static quadrupole potential

$$Q\phi_W = \tfrac{1}{2}m\omega_W^2(x_{\rm rot}^2 - y_{\rm rot}^2). \tag{26}$$

In Eq. (26) the frequency ω_W characterizes the strength of the quadrupole potential and $x_{\rm rot}$ and $y_{\rm rot}$ are rotating frame coordinates along the strong and weak axes of the rotating quadrupole potential. The rotating quadrupole potential breaks the symmetry of the trap potential and changes the shape of the ion crystal, providing a restoring force that controls the azimuthal orientation of the ion crystal in the frame of the rotating potential.

C. Laser cooling

The low temperature required for the formation of the ion Coulomb crystal is typically reached by means of laser cooling (Chu, 1998; Cohen-Tannoudji, 1998; Phillips, 1998). This mechanism is based on scattering of laser light and uses the mechanical effects of radiation to transfer energy from the ions' motion to the modes of the electromagnetic field. As such, the stationary state of the ions results from the dynamical equilibrium of scattering processes that heat and cool the motion. The width of the stationary energy distribution is determined by the characteristic linewidth of the scattering processes and is often associated with a temperature. See Sec. III.A for a detailed discussion. Laser cooling allows ions to be prepared at temperatures ranging from hundreds of millikelvins down to fractions of a microkelvin, depending on the technique that is employed and the ion species.

Laser cooling of ion crystals typically employs techniques that are appropriate for cooling individual ions. In fact, multiple photon-scattering events are rare because the ion crystals are optically thin. In this limit each ion of the crystal is effectively an independent scatterer (Morigi and Eschner, 2001, 2003). Nevertheless, there are some challenges to consider when applying laser-cooling protocols to ion ensembles. One important challenge is that processes that heat in general become increasingly important with the number of ions in the crystal. Another major challenge consists in the fact that the noninertial forces of the trap cannot be neglected for the ions located away from the symmetry axes. This makes it difficult to ensure that the sample is uniformly cooled at the same temperature. We discuss the implications on studies of thermalization in Sec. III. In the following we provide a review of the state of the art in preparing ion ensembles at low temperatures. For a comprehensive review of laser cooling with trapped ions, see Eschner *et al.* (2003).

The most commonly used laser-cooling technique is Doppler laser cooling, which can produce temperatures on the order of 1 mK or lower (Wineland and Itano, 1979; Stenholm, 1986; Eschner *et al.*, 2003). Doppler laser cooling has been used to prepare one-dimensional (1D), linear chain crystals of up to ~100 ions in linear rf traps (see Sec. II.A) and two-dimensional (2D), single-plane crystals of ions of up to ~500 ions in both Penning and rf ion traps (see Sec. II.B). Much larger three-dimensional (3D) ion crystals have been formed through Doppler laser cooling in both Penning ($>10^5$ ions) and rf ion traps ($>10^4$ ions); see Sec. II.C.

Once formed, 1D and 2D ion crystals are cooled to temperatures well below the millikelvin regime by means of so-called sub-Doppler-cooling techniques. Examples of sub-Doppler-cooling techniques include polarization-gradient cooling (Birkl *et al.*, 1994; Joshi *et al.*, 2020; Li *et al.*, 2022), sideband cooling (Diedrich *et al.*, 1989; Monroe *et al.*, 1995), and electromagnetically induced transparency (EIT) cooling (Morigi, Eschner, and Keitel, 2000; Roos *et al.*, 2000). For completeness we also mention protocols for simultaneously cooling the vibrational modes of an ion chain to the ground state that are based on designing the chain spectrum by means of an external field (Wunderlich, Morigi, and Reiß, 2005; Fogarty *et al.*, 2016). These sub-Doppler-cooling techniques can prepare the crystal close to the zero-point motion. Sideband cooling is routinely used to sequentially cool the vibrational modes of an ion chain in a linear Paul trap to near

the quantum mechanical ground state (Eschner *et al.*, 2003). Moreover, in Penning traps small crystals with fewer than ten ions have been successfully sideband cooled (Stutter *et al.*, 2018).

EIT cooling has been demonstrated to be particularly efficient for cooling crystals of ions to the ground state, thanks to the Fano-like profile of the scattering processes (Morigi, 2003), which permits several vibrational modes of the crystal to be cooled simultaneously (Schmidt-Kaler *et al.*, 2001). In a linear Paul trap, ion chains ranging from a few ions (Lin *et al.*, 2013) to the transverse motion of a chain of 18 ions (Lechner *et al.*, 2016) and 40 ions (Feng *et al.*, 2020) have been EIT cooled to near the ground state. EIT cooling has also been employed to simultaneously cool the out-of-plane modes of single-plane crystals to near the ground state of the vibrational motion in Penning traps (Jordan *et al.*, 2019; Shankar *et al.*, 2019) and rf traps (Kiesenhofer *et al.*, 2023; Guo *et al.*, 2024).

While 1D and 2D crystal formation has been limited to a few hundred ions, Doppler laser cooling has been used to prepare much larger, mesoscopic, 3D crystals in both Penning and rf traps. Laser cooling may play a role in determining the size of ion crystals that can be produced in the laboratory. We now discuss experimental demonstrations of some of the largest trapped-ion crystals that have been prepared in the laboratory.

Penning traps employ static confining fields, and the nonthermal motion of ions in the trap is a rigid body rotation that is not readily shared with the thermal degrees of freedom. Therefore, the implementation of Doppler cooling of rotating ion ensembles in Penning traps is relatively straightforward, although Doppler shifts due the ion-crystal rotation can produce temperatures that are slightly elevated from standard Doppler-cooling limits (Torrisi *et al.*, 2016). Three-dimensional crystals with $N \sim 5 \times 10^5$ ions have been Doppler cooled in Penning traps to millikelvin temperatures ($\Gamma > 200$), where a body-centered-cubic (bcc) lattice structure in the crystal's interior was observed (Tan *et al.*, 1995; Itano *et al.*, 1998). Doppler cooling has been demonstrated to be effective for larger ensembles: non-neutral plasmas of $N \sim 10^8$ Mg^+ ions in Penning-Malmberg traps have been prepared at temperatures less than 50 mK (Anderegg *et al.*, 2009, 2010). Here the ions are strongly correlated ($\Gamma \sim 20$), but have a temperature above that for crystal formation. The lack of crystal formation is not understood. Its origin is probably due to the scaling with N of heating processes. For example, the potential energy stored in the ion crystal increases with N, and in Penning traps small imperfections in the construction of the trap can drive a slow radial expansion of the ion crystal that converts potential energy to kinetic energy (Dubin and O'Neil, 1999; Jensen, Hasegawa, and Bollinger, 2004).

Cooling large ion ensembles in rf traps is challenging because of the time-dependent potential. In fact, the rf-driven micromoton can be converted into thermal motion by the Coulomb interactions, thereby heating the crystal. This heating rate increases as the temperature is lowered and the number of ions increases, thus giving rise to chaotic dynamics and limiting the cooling efficiency (Blümel *et al.*, 1989; Prestage *et al.*, 1991; Nam, Jones, and Blümel, 2014; Poindron, Pedregosa-Gutierrez, and Champenois, 2023). Therefore, the formation of large ion crystals in rf traps requires large laser-cooling powers. Despite these difficulties, large crystals composed of 10^4 or up to 10^5 ions have been prepared in rf traps (Drewsen *et al.*, 1998; Hornekær and Drewsen, 2002; Mortensen *et al.*, 2006). It has been observed that once the ion crystal forms, the rf heating can be significantly reduced. A lower limit on the Coulomb coupling parameter of $\Gamma \gtrsim 70$ has been estimated from the observed structure of these large ion crystals in rf traps. Direct measurements of the ion temperature are challenging with 3D crystals in rf traps because of the large driven micromotion. We conclude this section by noting that, to date, sub-Doppler laser-cooling techniques have not been demonstrated on large 3D ion crystals.

D. Ion-trap arrays and optical dipole traps

In this review we focus on ion crystals that form at low temperatures in a configuration resulting from the interplay of a common ion-trap potential and the Coulomb repulsion. In this section we provide an outlook on other kinds of trapping potentials that have been discussed in the literature and that are based on mechanisms other than those discussed in the rest of this review. One such alternative approach uses an array of trapping potentials where each cell stores a single ion (Schmied, Wesenberg, and Leibfried, 2009). This approach enables the generation of arbitrary lattice geometries. Ion-trap arrays are being pursued with both rf ion traps (Mielenz *et al.*, 2016; Lysne *et al.*, 2024; Niedermeyer *et al.*, 2025) and Penning traps (Jain *et al.*, 2020, 2024). Currently, the number of ions stored in an ion-trap array is small (up to $N \sim 4$).

A further approach employs optical dipole traps for ions with optical dipole transitions. A major motivation is to avoid the boundary effects that are significant in Penning and Paul traps, thereby ideally realizing strings of equidistant ions. The micromotion due to the coupling of the charge monopole to the fast laser oscillations at the optical frequency is negligible and the potential the ions experience is essentially the same as the potential experienced by neutral atom scattering in the visible spectrum (Cormick, Schaetz, and Morigi, 2011). Optical trapping of ion Coulomb crystals is challenging because of the strength of the Coulomb repulsion of closely spaced ions, which requires large laser powers. Experimental demonstrations have included the trapping of linear strings of up to 6 ions by a single beam optical dipole trap (Schmidt *et al.*, 2018) and confinement of a few ions in a one-dimensional optical lattice (Hoenig *et al.*, 2023). An alternative approach is to use an array of optical tweezers (Mazzanti *et al.*, 2021). Studies have indicated that this architecture could provide a scalable approach for fault-tolerant digital quantum computation and analogue quantum simulations with ion arrays (Arias Espinoza *et al.*, 2021; Mazzanti *et al.*, 2021; Schwerdt *et al.*, 2024).

Somewhat less demanding in laser power is the use of optical dipole forces to modify the normal-mode spectrum of a trapped ion crystal. See Sec. III.E for an extensive discussion.

II. ION COULOMB CRYSTALS: FROM ONE TO THREE DIMENSIONS

Trapped ions can crystallize in different structures determined by the geometry of the confining potential and their number. Linear, planar, and up-to-cubic-centered structures have been realized in the laboratory. In this section we review the equilibrium properties of the crystals from one- to three-dimensional spatial arrangements of the ions. We start with the linear chain, on which an extensive number of studies have been performed, then review planar structures, and finally report on the crystalline properties of three-dimensional structures. Unlike previous reviews, we set the focus on the dynamical and thermodynamical properties for the purpose of establishing a direct link with condensed-matter systems.

A. Linear geometries: The ion chain

Figure 8 is the image of an experimentally realized ion chain composed of more than 100 ions (Pagano *et al.*, 2018). The interparticle distances are on the order of several micrometers, and the individual ions can be imaged on a CCD camera via fluorescence light emitted during laser excitation. Ion chains typically form at Doppler-cooling temperatures. The first experimental demonstrations were in quadrupole traps (Birkl, Kassner, and Walther, 1992; Raizen *et al.*, 1992; Waki *et al.*, 1992). More recently, linear chains have also been realized in Penning traps (Mavadia *et al.*, 2013) and ring geometries (Li *et al.*, 2017). The ion chain has been the workhorse of the ion-trap quantum computer for the versatility in controlling the individual components, such as the interactions between the electronic and the vibrational degrees of freedom at the quantum level (Cirac and Zoller, 1995).

Chains of ions are a laboratory realization of a one-dimensional Debye crystal (Ashcroft and Mermin, 1976). Owing to the unscreened Coulomb interactions, this realization constitutes a peculiar one-dimensional structure. We now review salient dynamic and thermodynamic properties, emphasizing analogies with and fundamental differences from textbook examples of condensed-matter systems.

1. Ground-state configuration

Ion chains are the stationary configurations of anisotropic, elongated potentials. In typical setups the ions are at distances of several micrometers and the ground state is fully characterized by the configuration that minimizes the potential energy V, which consists of the Coulomb repulsion and the external trap potential. For N ions the equilibrium positions are the solution of the coupled nonlinear equations $\boldsymbol{\nabla}_j V = 0$, with $\boldsymbol{\nabla}_j$ the gradient for the particle at position $\mathbf{r}_j = (x_j, y_j, z_j)$ and $j = 1, \ldots, N$.

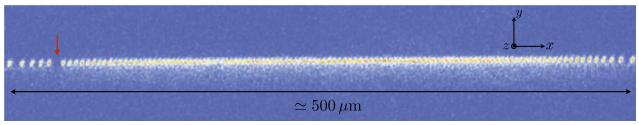

FIG. 8. Linear chain of 121 $^{171}Yb^{+}$ ions in a cryogenic linear Paul trap with $\omega_y/2\pi = 1.5$ MHz and $\omega_x/2\pi = 35$ kHz. The red arrow marks a lone $^{171}Yb^{+}$ ion that is in a state that does not fluoresce. This dark ion retained its position after more than 4 h, suggesting that the chain kept its ordered structure and never melted despite collisions with the background gas. From Pagano *et al.*, 2018.

For a linear Paul trap with cylindrical symmetry about the chain axis, the potential takes the form

$$V = \frac{1}{2}\sum_{j=1}^{N} m[\nu^2 x_j^2 + \nu_t^2(y_j^2 + z_j^2)] + \frac{1}{2}\sum_{i\neq j}^{N} \frac{Q^2}{|\mathbf{r}_i - \mathbf{r}_j|}, \quad (27)$$

where m is the mass, Q is the charge, and ν and ν_t are, respectively, the trap axial frequency and the transverse trap frequencies in the pseudopotential approximation, such that $\nu < \nu_t$. The linear chain is stable for ν_t/ν exceeding a critical value, as we soon detail.

The equilibrium positions of the ions in a linear Paul trap are typically determined numerically (Schiffer, 1993; James, 1998). An approximate analytical expression can be found in the limit of large N by means of the local density approximation. In this limit the linear density $n(x)$ is a smooth function of the position x along the axis. It takes the shape of the Thomas-Fermi distribution (Dubin, 1997),

$$n(x) = \frac{3}{4}\frac{N}{L}\left(1 - \frac{x^2}{L^2}\right), \quad (28)$$

with $|x| \leq L$, and vanishes otherwise. The parameter L is the chain half length at equilibrium and is determined by means of a variational ansatz, such that to leading order in an expansion in $\log N$, it reads (Dubin, 1997)

$$L(N) = [N \log N(3Q^2/(m\nu^2)]^{1/3}. \quad (29)$$

At the chain center, the density varies slowly about the value $n(0) \sim N/L$, where the interparticle distance is minimal, $a(0) = 1/n(0)$. Figure 9 shows that Eq. (28) gives a good estimate of the charge distribution sufficiently far from the chain edges. Equation (28) has been experimentally validated for chains composed of more than 100 ions and has been used to determine the number of trapped ions without counting the individual components (Kamsap *et al.*, 2017).

Like solid-state systems, a thermodynamic limit is identified by scaling N and L, leaving $n(0)$ constant. Owing to the dependence of L on ν and N, this imposes that the axial trap frequency will scale with N as (Morigi and Fishman, 2004a)

$$\nu(N) \sim \omega_0 \sqrt{\log N}/N, \quad (30)$$

with the reference frequency

$$\omega_0^2 = Q^2/(4\pi\epsilon_0 m a_0^3), \quad (31)$$

and $a_0 = a(0)$ the interparticle distance at the chain center.

This analysis ignores thermal and quantum fluctuations, which tend to suppress long-range order in one dimension. Strictly speaking, a perfectly ordered linear chain is unstable in the thermodynamic limit ($L \to \infty$). In practice, however, under suitable conditions the crystalline order can persist over

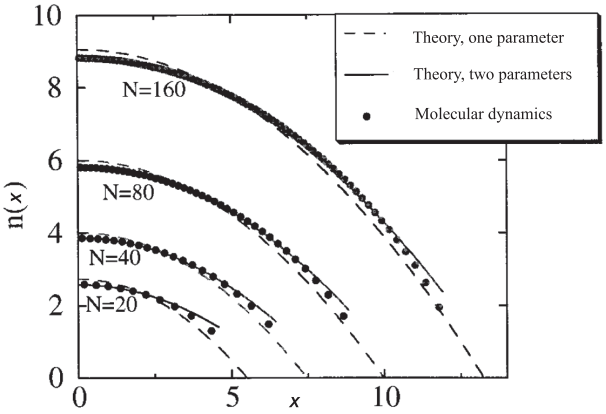

FIG. 9. Density of charges per unit length $n(x)$ as a function of position x from the center of the chain for different numbers N of ions in a linear Paul trap. The dots are the equilibrium positions determined by molecular dynamics simulation for a finite number of ions N. The lines are obtained using the method of trial variational functions with two parameters. The dashed lines are the one-parameter function of Eq. (28). Both x and $n(x)$ are scaled to $(Q^2/m\nu^2)^{1/3}$. From Dubin, 1997.

sufficiently large length scales such that the chain effectively appears to be fully ordered. Stability against quantum fluctuations was studied by Schulz (1993) by means of a treatment based on bosonization showing that at zero temperature the density-density correlations of a one-dimensional Wigner crystal decay with the distance x as $\exp(-c\sqrt{\log x})$, with c a constant (Schulz, 1993). This is an extremely slow decay: any large (but finite) chain can be considered crystallized. Stability against thermal fluctuations requires $Q^2 \log N/(4\pi\epsilon_0 a_0) \gg \kappa_B T$ (namely, the potential energy scale is larger than the thermal fluctuations), where T is the temperature and the classical equipartition theorem has been used (Morigi and Fishman, 2004b). This shows that, for sufficiently large chains, the long-range Coulomb correlations dominate over thermal disorder.

2. Normal modes of the ion chain

At laser-cooling temperatures, the ions perform vibrations about the equilibrium positions with displacements of the order of tens of nanometers, and thus about 3 orders of magnitude smaller than the equilibrium interparticle distance. In this regime the restoring forces are harmonic and the ion chain is a one-dimensional harmonic crystal. Figure 10 displays Stokes sidebands measured in the resonance fluorescence of a chain of 24 ions. The measured spectra are reproduced by theoretical models that approximate the potential of Eq. (27) by keeping the quadratic terms only in the displacements about the equilibrium position.

In the following we focus on ion chains in a linear Paul trap and in the pseudopotential approximation. We note that the analysis will also apply to linear chains in Penning traps (Mavadia *et al.*, 2013) at the so-called Brillouin limit, where the effective magnetic field is zero. See Lin *et al.* (2009), Home *et al.* (2011), and Cartarius, Cormick, and Morigi (2013) for studies of the normal modes of ion chains in anharmonic traps.

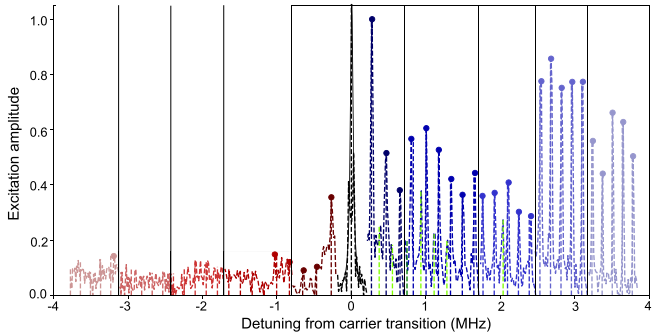

FIG. 10. The frequency sideband spectrum of the axial modes of a laser-cooled chain composed of 24 $^9Be^+$ ions. The dashed lines show the experimental results of the normalized excitation level vs frequency, whereas the red and blue lines denote the scan over redshifted sideband (anti-Stokes), carrier, and blueshifted sideband (Stokes) transitions, respectively. The brightness of the dashed line shows the variable probe times throughout the spectrum to ensure that all modes are excited with high visibility. The dashed vertical blue and red (dark) lines show all 24 calculated first-order red and blue sideband frequencies. The dashed vertical green (light) lines show the mode mixings between the center of mass and a few higher-frequency modes, coinciding with the smaller peaks in the experimental data. The part of the spectrum between the two vertical black lines has been recorded with the same probe time, while probe times differ between the sections. Details on the figure were given by Wu, Shi, and Zhang (2023).

In a harmonic trap, axial and transverse motion are decoupled and the harmonic spectrum can be numerically determined even for relatively large chains. The set of linear differential equations are obtained by expanding the potential [Eq. (27)] to second order in the axial displacements from the axial equilibrium positions, $q_i = x_i - x_i^{(0)}$, and in the transverse displacements from the chain, $\zeta_i = y_i, z_i$. They read

$$\ddot{q}_i = -\nu^2 q_i - K_0 \sum_j \mathcal{I}_{ij} q_j, \tag{32}$$

$$\ddot{\zeta}_i = -\nu_t^2 \zeta_i + \frac{K_0}{2} \sum_j \mathcal{I}_{ij} \zeta_j, \tag{33}$$

where $K_0 = 2Q^2/(mL^3)$ scales the long-range Coulomb interaction and $\mathcal{I}_{ij}$ is a $N \times N$ real symmetric matrix,

$$\mathcal{I}_{ij} = -(1-\delta_{ij}) \frac{1}{|\xi_i - \xi_j|^3} + \delta_{ij} \sum_{l \neq i} \frac{1}{|\xi_i - \xi_l|^3}, \tag{34}$$

with δ_{ij} the Kronecker delta. In Eq. (34) $\xi_i = x_i^{(0)}/L$ is the dimensionless equilibrium position rescaled by the half length L of the chain at equilibrium. The set of differential equations (32) and (33) is solved by diagonalizing the matrix I_{ij}, thereby solving the linear set of equations

$$\sum_j \mathcal{I}_{ij} w_j^{(n)} = \lambda_n w_i^{(n)}, \tag{35}$$

whose eigenvalues λ_n are real and positive. The axial and transverse dispersion relations read, respectively,

$$\omega_n^{\parallel 2} = \nu^2 + K_0\lambda_n, \tag{36}$$

$$\omega_n^{\perp 2} = \nu_t^2 - K_0\lambda_n/2, \tag{37}$$

with $n \in [1, N]$ and $\omega_n^{\perp}$ doubly degenerate in a cigar-shaped trapping potential. While $\omega_n^{\parallel}$ is always real, $\omega_n^{\perp}$ becomes imaginary when $\lambda_n \geq 2\nu_t^2/K_0$. This identifies the critical value of the transverse trap frequency $\nu_t^{(c)}$ at which the chain becomes mechanically unstable.

In the rest of this section, we make general considerations on the structure of the eigenvalues for $\nu_t > \nu_t^{(c)}$, which are based on the treatment of Morigi and Fishman (2004a, 2004b). For convenience we adopt the convention $\lambda_n < \lambda_m$ for $n < m$. With this convention the label n directly gives the number of nodes $\ell = n - 1$ of the corresponding eigenmode $w^{(n)}$. Since the position of the nodes is generally constrained to the position of the ions within the chain, the value of λ_n generally depends on the number of ions N. There are two exceptions: (i) the eigenvalue $\lambda_1 = 0$ corresponding to the bulk eigenmodes where the chain oscillates as a rigid body at the frequencies of the trap and (ii) the eigenvalue $\lambda_2 = 2\nu^2/K_0$ corresponding to the breathing mode, which has a single node at the chain center. These two eigenvalues are related to two symmetries of the Hamiltonian: point (i) is due to the fact that the dynamics is separable into center-of-mass and relative coordinates even in the presence of the harmonic trap, and point (ii) is a consequence of the symmetry by reflection about the trap center. The breathing oscillations $\omega_2^{\parallel} = \sqrt{3}\nu$ and $\omega_2^{\perp} = \sqrt{\nu_t^2 - \nu^2}$, in fact, are also characteristic of a one-component plasma in an ellipsoidal trap (Dubin and Schiffer, 1996).

Some information on the analytical behavior of the other modes can be extracted for large numbers of ions N. For $n \ll N$, and thus for long-wavelength eigenmodes, the displacements $w_i^{(n)}$ can be approximated using continuous functions, $w_i \to w(\xi)$, and away from the edges the secular equation (35) reduces to a differential equation to leading order in an expansion in $1/\log N$ (Morigi and Fishman, 2004a, 2004b),

$$\log N[(1-\xi^2)w''(\xi) - 4\xi w'(\xi)] = \lambda_n w(\xi). \tag{38}$$

The eigenmodes are Jacobi polynomials $w^{(n)} = P_\ell^{(1,1)}$ with $n = \ell + 1$ and $\ell = 0, 1, \ldots$ The eigenvalues read $\lambda_n = \ell(\ell+3)$ and exactly reproduce the eigenvalues λ_1 and λ_2 for $\ell = 0$ and 1, as shown in Fig. 11. Note that the model of a plasma in a cigar-shaped trap potential gives the same expression for the axial spectrum $\omega_n^{\parallel} = \nu\sqrt{n(n+1)/2}$ in the limit of the vanishing aspect ratio; see Dubin (1991). The same plasma model, however, fails to predict the transverse oscillations of the chain, since it becomes singular.

The short-wavelength spectrum is also amenable to some analytical treatment. Morigi and Fishman (2004b) determined the density of states at short wavelengths by extending analytical methods that were originally developed for calculating the dispersion relation of disordered chains (Dyson, 1953). The same treatment allows one to determine the largest

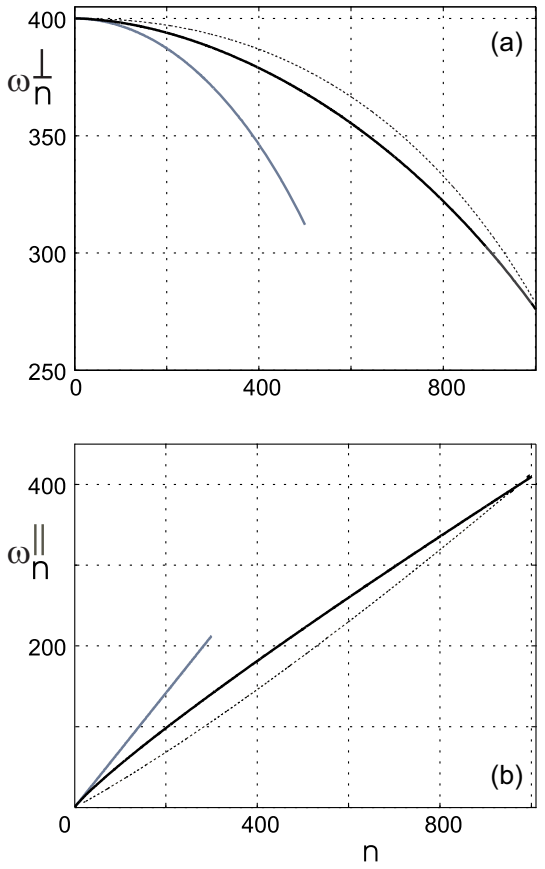

FIG. 11. (a) Transverse and (b) axial spectrum of eigenfrequencies (in units of ν) for a chain of $N = 1000$ ions and with $\nu_t = 400\nu$. The solid line is obtained from the numerical solution of Eq. (35), and the gray line is taken from the spectrum of Eq. (38) (the gray curves have been truncated, as they do not correctly reproduce the short-wavelength eigenmodes). The dotted line gives the spectra evaluated by extending a method first developed for determining the density of states of a disordered chain. Adapted from Morigi and Fishman, 2004b.

eigenvalue λ_N. At leading order in an expansion in $1/\log N$ and using the thermodynamic limit of Eq. (30), one obtains $K_0\lambda_N = (9/8)\nu^2N^2/\log N = 8Q^2/(ma_0^3) = 8\omega_0^2$. This shows that the frequency ω_0 scales the bandwidth of the axial mode spectrum. It also scales the critical value of the transverse trap frequency $\nu_t^{(c)}$, at which the chain becomes unstable. The latter is found setting $\omega_N^{\perp} = 0$, giving $\nu_t^{(c)} = \sqrt{K_0\lambda_N/2} = 2\omega_0$. The corresponding critical aspect ratio reads $\alpha^{(c)} = (\nu/\nu_t^{(c)}) = \sqrt{(16/9)\log N}/N$ (Dubin, 1991; Schiffer, 1993; Morigi and Fishman, 2004b). In Sec. II.A.4 we review the structural transition at $\nu_t = \nu_t^{(c)}$ and its statistical properties.

In the regime of stability of the linear chain (but for $\nu_t \sim 8\omega_0$), axial and transverse eigenfrequencies can be degenerate and the coupling due to anharmonicities becomes relevant. The effects of this coupling have been measured even at the level of vibrational quanta (Roos *et al.*, 2008).

When instead the trap frequency $\nu_t \gg 8\omega_0$, there is a gap between axial and transverse modes. Moreover, the transverse spectrum becomes almost flat, so the transverse dynamics is well approximated by local oscillators weakly coupled via the

Coulomb interactions. This regime is at the basis of the proposals for realizing effective Hubbard models (Porras and Cirac, 2004) and for implementing quantum information processors using ion chains (Serafini, Retzker, and Plenio, 2009).

3. Thermodynamics of the ion chain

The thermodynamic properties of Debye crystals are textbook examples, and a linear chain provides a laboratory to verify hypotheses and predictions down to the quantum regime and even close to the absolute zero, thanks to laser cooling. Quantities such as the specific heat could be measured in a calorimetric experiment where the temperature of the crystal is determined as a function of the energy transferred to the chain. The temperature can be extracted by resonance fluorescence, as in the protocols discussed by Roßnagel *et al.* (2015) and Gajewski *et al.* (2022), or by means of so-called sideband thermometry (Eschner *et al.*, 2003; Vybornyi *et al.*, 2023).

From a theoretical point of view, there is an essential difference between the textbook solid-state crystals, where the interaction is typically nearest neighbor, and the long-range Coulomb repulsion of ion Coulomb chains. Morigi and Fishman (2004a, 2004b) studied the influence of Coulomb repulsion on thermodynamic behavior by determining the specific heat per particle and the coefficient of thermal expansion. They considered the case in which the motion is effectively one dimensional, which is realized for an ion chain in a steep transverse trap potential, assuming temperatures for which the transverse vibrations are frozen out. Using the notation of Sec. II.A.2, this requires that $\nu_t \gg 8\omega_0, k_B T/\hbar$.

The free energy is evaluated while assuming quantized vibrations and a canonical ensemble with temperature T, using the scaling of Eq. (30), which warrants a well-defined thermodynamic limit. The free energy is a function of the number of ions N, of the temperature T, and of the volume. The volume is determined by the length L from end to end, which for fixed N is controlled by the axial trap frequency ν; see Eq. (29). The specific heat is $c_a = (1/N)\partial U_{\rm th}/\partial T|_{\nu,N}$, where $U_{\rm th}$ is the thermal energy of a quantum gas of phonons, $U_{\rm th} = \sum_n \hbar\omega_n^{\parallel}/(e^{\beta\hbar\omega_n^{\parallel}} - 1)$ with $\beta = (k_B T)^{-1}$ the inverse temperature. Figure 12(a) shows that the behavior of the specific heat with the temperature is similar to that of a one-dimensional Debye chain: it saturates at large temperatures, characteristic of Dulong-Petit law, while at low temperatures c_a scales linearly with T. Note that the limits $T \to 0$ and $N \to \infty$ do not commute. By keeping N constant, the proportionality coefficient in the relation $c_a = \gamma T$ is a function of N, namely, $\gamma \sim 1/\sqrt{\log N}$ (Morigi and Fishman, 2004b). This deviation from extensivity is due to the long-range interactions and becomes evident in the quantum regime. Despite the nonintensive behavior of the specific heat (namely, the fact that it depends on N), the usual ensemble equivalence holds because the relative energy fluctuations at low temperatures scale as $(\sqrt{\log N}/N)^{1/2}$, and hence vanish in the thermodynamic limit $N \to \infty$.

The coefficient of thermal expansion takes the form $\alpha_T = (1/L)\partial L/\partial T|_{P,N}$ and is calculated at constant pressure

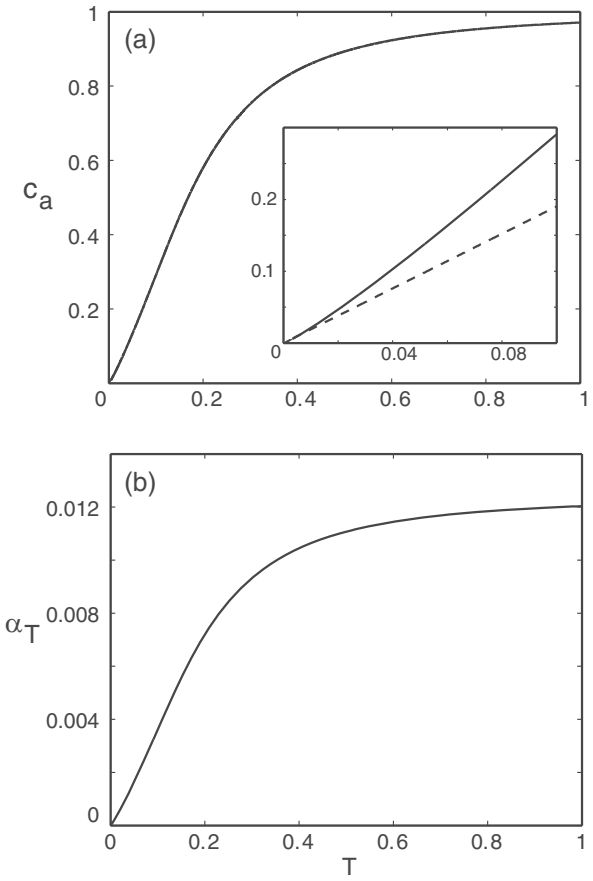

FIG. 12. (a) Specific heat c_a, in units of k_B, and (b) coefficient of thermal expansion α_T, in units of $\hbar\omega_N^{\parallel}$, as functions of the temperature T. The temperature is in units of the Debye temperature $\Theta_D = \hbar\omega_N^{\parallel}/k_B$. The thermodynamic functions are calculated for $N = 1000$ ions in the limit in which the transverse excitations are frozen out. This would correspond to an experiment with $\nu = 2\pi \times 31$ kHz and $\nu_t = 2\pi \times 34$ MHz. For these parameters and beryllium atoms, $\Theta_D \approx 20$ μK. Inset of (a) Low-temperature behavior of the specific heat. The dashed line is the slope extracted from a theoretical analysis that uses the density of states for $\omega_n^{\parallel} = \nu\sqrt{n(n+1)/2}$; see Sec. II.A.2. Adapted from Morigi and Fishman, 2004b.

P and number of ions N. Using thermodynamic relations, one can show that its temperature dependence is determined by c_a,

$$\alpha_T = \frac{3}{2}\frac{N}{L}\kappa_T c_a, \tag{39}$$

where κ_T is the isothermal compressibility, which is independent of T at leading order (Morigi and Fishman, 2004a). Figure 12(b) shows that the functional dependence on the temperature is similar to the specific heat. Owing to the nonintensive behavior of the isothermal compressibility, the coefficient of thermal expansion is also a nonintensive function of N over the entire range of temperatures.

The nonintensive behavior of specific heat and of α_T is a manifestation of the long-range Coulomb interactions in one dimension. It is typically cured by theoretical procedures, so-called Kac scaling (Campa, Dauxois, and Ruffo, 2009), which

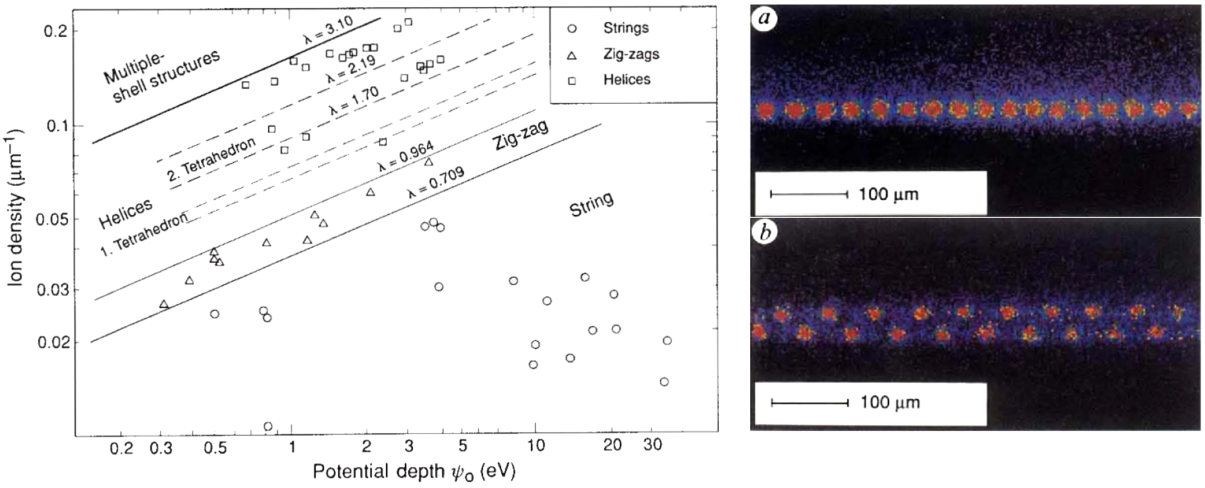

FIG. 13. Left panel: summary of the experimentally observed configuration as a function of the potential depth and the linear ion density. These two parameters can be combined to give the normalized linear particle density λ, which fully determines the ion configuration; see the text. The observed configurations are labeled with different symbols for each structure. The straight lines show critical λ values separating the regions of different theoretically expected structures; see Hasse and Schiffer (1990). Right panel: images of crystalline structures of laser-cooled $^{24}Mg^{+}$ ions in a quadrupole trap. Adapted from Birkl, Kassner, and Walther, 1992.

in this case would consist in artificially assuming that the ion's electric charge depends on N in such a way to reestablish extensivity of the energy (Landa, Cormick, and Morigi, 2020). In experiments the charge is fixed and measurements at low temperatures would detect a relatively strong dependence of c_a on the size of the chain, while they converge to a well-defined, size-independent limit at relatively large temperatures.

4. The linear-zigzag transition

We devote the rest of this section to the structural instability of the linear chain. The demonstration that this is a second-order phase transition of the Ising universality class of magnetic systems has permitted researchers to directly connect the physics of ion Coulomb crystals with statistical mechanics and condensed-matter concepts and models. This has paved the way to a series of theoretical and experimental investigations on critical properties, which we review later in the review. It has further inspired and set the basis for subsequent works on the formation and stability of topological defects; see Secs. III.C–III.F.

Structural order in ion crystals is stabilized by the external trap, which compensates for the repulsive Coulomb interactions. The resulting geometries are determined by the number of ions and the trap aspect ratio. Starting with a linear chain in a cigar-shaped potential, a rich phase diagram of structures was observed by decreasing the trap aspect ratio (Birkl, Kassner, and Walther, 1992; Waki *et al.*, 1992); see the left panel of Fig. 13. The experimental observations are in agreement with the theoretical results of Hasse and Schiffer (1990) and Dubin (1993). The mechanical instability of the linear chain separates it from a planar structure: the ion order in a zigzag array, like that shown in the right panel of Fig. 13. Evidence of the linear-zigzag transition has been reported in numerous studies, starting with the first experimental (Birkl, Kassner, and Walther, 1992; Raizen *et al.*, 1992; Waki *et al.*, 1992) and numerical (Dubin, 1993; Schiffer, 1993) investigations. Further studies sought evidence that this transition is of second order (Schiffer, 1993; Enzer *et al.*, 2000; Piacente *et al.*, 2004), starting with the observation that the zigzag structure breaks the cylindrical symmetry of the linear chain. This conjecture has been supported by numerical results on the derivatives of the energy of finite chains at the linear-zigzag transition (Dubin, 1993; Piacente *et al.*, 2004).

These conjectures are put on solid ground using a statistical mechanics approach that derives the Landau theory of the linear-zigzag instability starting with the classical potential energy of an ion chain (Fishman *et al.*, 2008). This theory shows that the linear-zigzag transition in ion Coulomb chains is of the same universality class of the mean-field phase transition from paramagnet to ferromagnet. Its predictions have been confirmed by experimental studies thus far, as we detail in Sec. III.D. In the following we review the main arguments and steps of the derivation of Fishman *et al.* (2008).

Assume now the thermodynamic limit, which consists of an infinite chain with particles at the uniform distance $a \equiv a(0)$. Away from the critical aspect ratio, the equilibrium positions are $x_n^{(0)} = na$, $y_n^{(0)} = z_n^{(0)} = 0$, and the potential [Eq. (27)] is approximated using its quadratic expansion $V \simeq V^{(0)} + V^{(2)}$. The chain is invariant under discrete displacements; hence, the eigenmodes are standing waves with quasimomentum $k = \pi\ell/Na$. The quadratic term $V^{(2)}$ reads

$$V^{(2)} = \frac{m}{2}\sum_{k>0,s=\pm}\left[\omega_{\parallel}(k)^2\Theta_k^{(s)2} + \beta(k)\left(\Psi_k^{y(s)2} + \Psi_k^{z(s)2}\right)\right], \quad (40)$$

where $\Theta_k^{(s)}$ is the Fourier transform of the axial displacements q_j and $\Psi_k^{y(s)}$ and $\Psi^{z(s)}$ are the Fourier transforms of the transverse displacements y_j and z_j, respectively, while $s = \pm$ denotes the cosine and sine standing waves. The left panel of Fig. 14 displays the normal-mode spectrum. For the linear-zigzag instability, the dispersion relation of the transverse excitation is crucial. Its explicit form (Hasse, 1992; Fishman *et al.*, 2008),

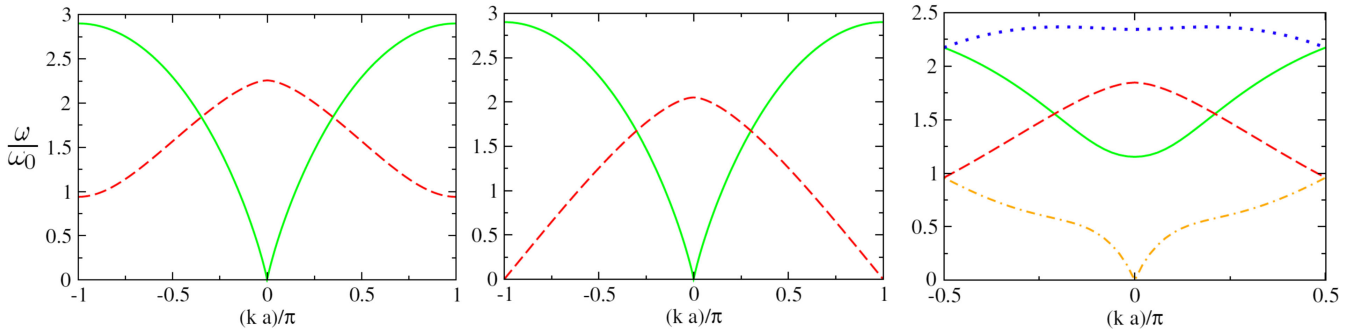

FIG. 14. Normal modes of a uniform chain as a function of the quasimomentum k for (left panel) the linear array $\nu_t > \nu_t^{(c)}$, (middle panel) at the transition $\nu_t = \nu_t^{(c)}$, and (right panel) a zigzag array $\nu_t < \nu_t^{(c)}$. In the left and center panels, the dashed red line denotes the transverse vibrations [Eq. (41)]. In the middle panel, at the critical frequency, the mode at vanishing frequency is the zigzag mode. In the right panel, the Brillouin zone of the zigzag array is half the size of the linear chain owing to the period doubling of the zigzag structure. Adapted from Fishman *et al.*, 2008.

$$\beta(k)^2 = \nu_t^2 - K_0\left(\frac{L}{a}\right)^3 \sum_{j=1}^{N/2} \frac{1}{j^3} \sin^2 \frac{jka}{2}, \tag{41}$$

allows one to make several key observations: (i) The minimal transverse frequency $\omega^{\perp}(k)$ is at the quasimomentum $k_0 = \pi/a$. These are the eigenmodes with the shortest wavelength, $2a$, which is also known as zigzag eigenmodes because neighboring ions oscillate with opposite phases, $y_i = (-1)^i \Phi_{k_0}^{(y)}$ and $z_i = (-1)^i \Phi_{k_0}^{(z)}$. (ii) The linear chain becomes unstable when the eigenfrequency of the zigzag mode vanishes, i.e., $\beta(k_0) = 0$; see the center panel of Fig. 14. This determines the critical transverse trap frequency

$$\nu_t^{(c)} = \omega_0 \sqrt{7\zeta(3)/2}, \tag{42}$$

with $\zeta(j)$ Riemann's ζ function and $\omega_0 = \sqrt{Q^2/(4\pi\epsilon_0 m a^3)}$. In terms of this notation, the normalized particle density of Fig. 13 becomes $\lambda = (3\omega_0^2/\nu_t^2)^{1/3}$, so its critical value for the linear-zigzag transition is $\lambda_c = [3/7\zeta(3)]^{1/3} \approx 0.709$.

For $\nu_t < \nu_t^{(c)}$, when the linear chain is unstable, the quadratic term of Eq. (40) gives imaginary eigenfrequencies. The new ground state is then determined by including higher-order terms in the expansion. Nevertheless, for ν_t that is sufficiently close to $\nu_t^{(c)}$, the transverse displacement is finite but smaller than a, and one expects that only the modes with frequency close to zero will contribute to determining the new structure. These are the transverse eigenmodes with wave number $k = k_0 - \delta k$ and $k = -k_0 + \delta k$ such that $|\delta k a| \ll 1$. By taking the Taylor expansion of the potential V about the equilibrium position of the linear chain but truncating now at fourth order, the lowest (zeroth) order in an expansion in the small parameter $|\delta k a|$ (the gradient expansion) is the Landau potential for the transverse displacement $\varrho = \sqrt{\Phi_0^{z2} + \Phi_0^{y2}}$ in a cigar-shaped trap,

$$V_0(\varrho) = \tfrac{1}{2} m(\nu_t^2 - \nu_t^{(c)2})\varrho^2 + \mathcal{A}\varrho^4, \tag{43}$$

where $\mathcal{A} = (3/2)(31/32)\zeta(5)(Q^2/a^5)$.

For $\nu_t > \nu_t^{(c)}$ the potential V_0 has a single minimum at $\varrho = 0$ and the linear chain is the ground-state structure. By contrast, for $\nu_t < \nu_t^{(c)}$ the potential landscape has the characteristic form of a "Mexican hat" with degenerate zigzag ground states at different angles around the symmetry axis. The magnitude ϱ of the transverse displacement is fixed by minimizing $V_0(\varrho)$,

$$\bar{\varrho} = \sqrt{\frac{m}{4\mathcal{A}}(\nu_t^{(c)2} - \nu_t^2)}, \tag{44}$$

and is in full agreement with the exact solution close to the critical value; see Fig. 15. The plane of the zigzag structure is given by the angle $\varphi = \arctan(\Phi_0^y/\Phi_0^z)$ and can take any value between 0 and 2π. The system hence possesses a gapless "Goldstone mode," which is a consequence of the spontaneously broken symmetry to rotations around the trap axis.

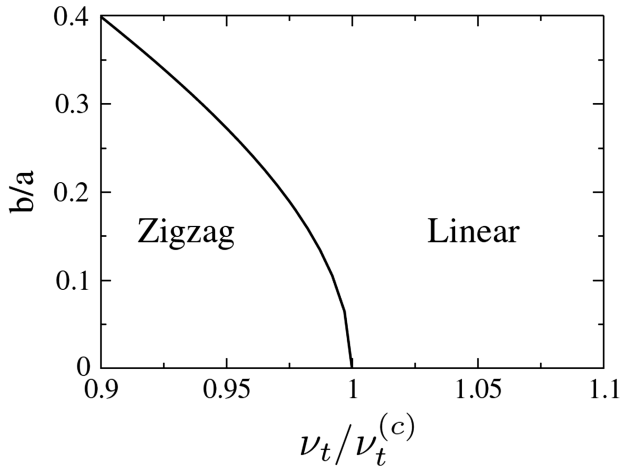

FIG. 15. Transverse equilibrium displacement $b = \varrho$, in units of the interparticle spacing a, as a function of the transverse frequency ν_t, in units of $\nu_t^{(c)}$. On the right of the curve, the ion crystal is a linear chain. In the region on the left of the curve, the ion crystal exhibits a zigzag structure. Adapted from Fishman *et al.*, 2008.

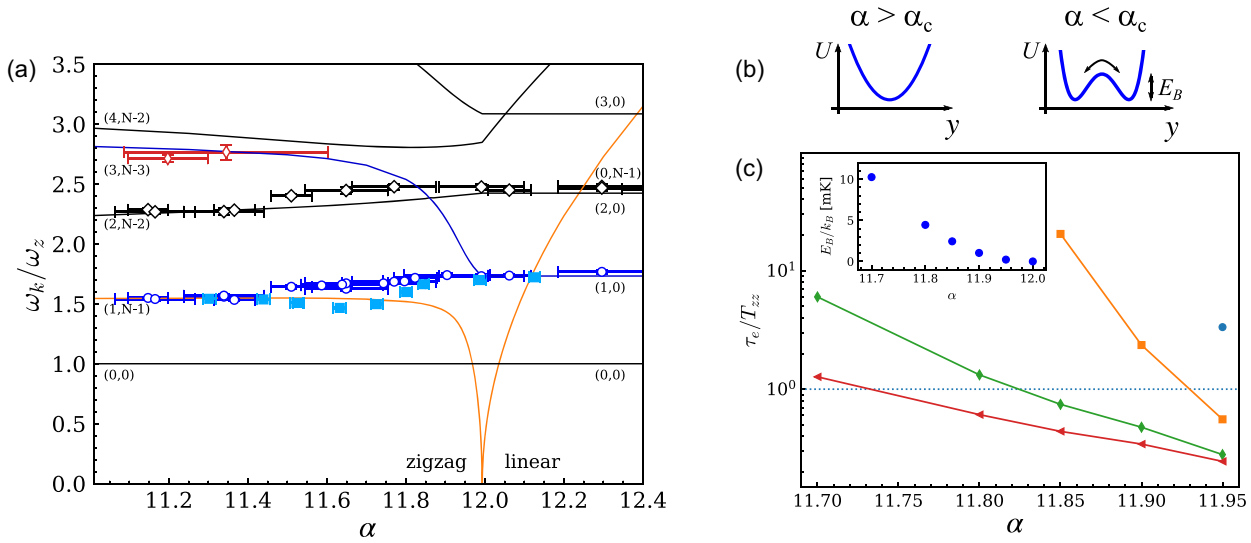

FIG. 16. (a) Low-frequency spectrum as a function of the aspect ratio α. The solid lines are the modes of the harmonic crystal at $T = 0$, and the symbols refer to the experimental measurements along with estimated uncertainties. The ions are laser cooled close to the Doppler limit. A comparison with molecular dynamics simulations gives $T \approx 3.5$ mK. (b) Schematic of the Landau potential in the linear ($\alpha > \alpha_c$) and the zigzag symmetry-broken phase ($\alpha < \alpha_c$). The coordinate y indicates the transverse displacement of the central ion from the chain axis. Thermal excitations can overcome the barrier between the two degenerate zigzag configurations by inducing collective jumps of the crystal configuration. (c) Average dwelling time τ_e, calculated using the Kramers formula, in units of the zigzag mode period $T_{zz} = 1/\omega_{k_0}$. In the simulations the temperatures T are 0.1 mK (blue circles), 0.5 mK (orange squares), 2.0 mK (green diamonds), and 3.5 mK (red triangles). The lines are a guide for the eye. For $T = 0.1$ and 0.5 mK, the missing points indicate no switches were observed during the simulation time. The horizontal dotted line indicates that $\tau_e = T_{zz}$. Inset: potential barrier E_B for different trapping ratios α. Adapted from Kiethe *et al.*, 2021.

Using Eq. (44), one can verify that the transition is continuous by evaluating the difference between the ground-state energy of the linear and that of the zigzag structure. This yields $\Delta E = -(1/2)m\mathcal{C}a^2(\nu_t - \nu_t^{(c)})^2$, with $\mathcal{C} = 112\zeta(3)/[93\zeta(5)]$. The second derivative with respect to ν_t is discontinuous at the critical point, in agreement with the behavior of a second-order phase transition.

This derivation is straighforwardly extended to geometries where the transverse confining potential is anisotropic, such that the confining frequency ν_t appearing in Eq. (27) is replaced by two different values, $\nu_{t,y}$ and $\nu_{t,z}$. In this case the anisotropy pins the zigzag orientation and aligns it in the direction of the weakest transverse confinement. For $\nu_{t,y} < \nu_{t,z}$, Eq. (44) gives the displacement $\varrho = \Psi_{k_0}^{(y)}$, and the angle determining the plane takes the two possible values $\varphi = 0$ and π: the Landau potential V_0 [Eq. (43)] now possesses two degenerate minima at $\phi_j = \pm\bar{\varrho}$, with $\bar{\varrho}$ given by Eq. (44). Thus, the anisotropy favors a zigzag structure confined to a particular plane. This zigzag configuration spontaneously breaks the reflection symmetry about the axis. As a consequence, the continuous XY symmetry of the transition is reduced to a discrete Ising symmetry. The potential close to the transition, including the first nonvanishing order in the small parameter of the gradient expansion $|\delta k|^2 a^2$, takes the form (Shimshoni, Morigi, and Fishman, 2011a)

$$V[\{\phi_j\}] = \sum_{j=1}^{N} V_0(\phi_j) + \frac{1}{2}K\sum_{j=1}^{N}(\phi_j - \phi_{j+1})^2, \quad (45)$$

where V_0 is the local potential [Eq. (43)] and $y_i = (-1)^i\phi_i(t)$ describes the transverse excitations within the interval δk, such that $\phi_i(t)$ is a slowly varying function of position i and time t and the position-averaged expectation value in the zigzag phase is Φ_0^y. The nonlocal part of the interaction is accounted for via the nearest-neighbor coupling term, with $K = m\omega_0^2 \log 2 = (Q^2/a^3)\log 2$ (now chosen to match the leading gradients in the space of the order parameter). Notably, the nearest-neighbor interaction results from the systematic gradient expansion about the soft mode (De Chiara *et al.*, 2008; Fishman *et al.*, 2008; Silvi *et al.*, 2014).

The Landau model is based on several conditions: critical behavior is strictly found for $N \to \infty$ and temperatures $T = 0$. In a linear Paul trap, where the density is inhomogeneous, the zigzag structure forms first at the chain center, where the density is maximal (Schiffer, 1993). For small chains the zigzag structure displaces the ions not only in the transverse but also in the axial direction. This effect becomes negligible close to the transition in chains of dozen of ions (Fishman *et al.*, 2008), where the zigzag eigenmodes are localized at the chain center and are well approximated by phononic waves[1] (Morigi and Fishman, 2004b). Kaufmann *et al.* (2012) experimentally showed that the micromotion modifies the

[1]At the trap center, Eq. (38) reduces to a wave equation in the thermodynamic limit, $I[w(\xi)] \sim \log N(\partial^2/\partial\xi^2)w(\xi)$, and the eigenmodes at the center are phononic waves (Morigi and Fishman, 2006). This expression also reproduces the behavior of the axial dispersion relation of a periodic chain for $k \sim \pi/(Na)$ and $\omega^{\parallel} \sim k\sqrt{|\log k|}$ (Ashcroft and Mermin, 1976).

eigenfrequencies close to the transition. The measurements are in agreement with a theoretical treatment that includes the periodic drive of the Paul trap (Landa *et al.*, 2012a); see Sec. III.A.

At finite, nonvanishing temperatures, the theory predicts that the linear-zigzag transition is a smooth crossover. For finite chains, nevertheless, a relatively sharp transition can be measured when the chain is prepared at temperatures below a critical value T_c that depends on the number of ions N. Kiethe *et al.* (2021) measured the normal-mode spectrum of a trapped-ion chain at the symmetry-breaking linear-to-zigzag transition and at finite temperatures. Spectroscopy was performed by modulating the amplitude of the Doppler-cooling laser to excite and measure the mode oscillations of a chain composed of 30 ^{172}Yb ions. The expected mode softening at the critical point, which is a signature of the second-order transition, was not observed; see Fig. 16(a). The spectroscopic signal at the transition is reproduced by molecular dynamics simulations, suggesting that the disappearance of the mode softening is due to the finite temperature of the chain. The experimental low-frequency spectrum about the transition point is also reproduced by an effective theory based on Landau model, where thermal effects determine the weight of anharmonicities coupling the soft mode with high-frequency modes (Kiethe *et al.*, 2021). Inspection of the numerical trajectories shows that the ions collectively jump between the two ground-state configurations of the symmetry-broken phase, as illustrated in Figs. 16(b) and 16(c). This jump rate is qualitatively reproduced using the Kramers formalism (Delfau, Coste, and Saint Jean, 2013). In this regime, where the ion dynamics consists of thermally activated jumps between the two zigzag configurations, a time-averaged measurement of the mean transverse displacement detects a linear chain where one would instead expect a zigzag structure. The transition to a zigzag configuration is measured at trap aspect ratios below the critical one and resembles a temperature-induced shift of the transition point (Gong, Lin, and Duan, 2010; Delfau, Coste, and Saint Jean, 2013; Li *et al.*, 2019).

Cosco *et al.* (2017) performed a quantum thermodynamic study of the linear-zigzag transition. They argued that the average work distribution diverges at the linear-zigzag critical point. They proposed revealing this prediction by performing small quenches of the ion-trap frequency across the transition and measuring the ion transverse displacements distribution. Interferometric protocols based on spin-motion entanglement across the linear-zigzag instability could access the autocorrelation function of the crystal (De Chiara *et al.*, 2008) and measure the normal-mode spectrum at criticality (Baltrusch, Cormick *et al.*, 2011; Baltrusch, Cormick, and Morigi, 2012). However, the interferometric signals are relatively sensitive to thermal effects, which tend to suppress entanglement (Baltrusch, Cormick, and Morigi, 2013). The universal critical exponents of Landau theory have been indirectly verified by experiments analyzing the scaling of defects by slowly quenching the trap aspect ratio across the linear-zigzag phase transition; see Sec. III.D. Zhang *et al.* (2023) performed sideband spectroscopy at the linear-zigzag transition, in the process revealing quantum effects. This suggests a potential access to a structural transition driven by quantum fluctuations, which is discussed in Sec. II.A.5.

5. The quantum linear-zigzag transition

Structural phase transitions in ion Coulomb crystals are typically modeled by the configurations that minimize the potential energy. Although this approach discards the kinetic energy, it proves to be sufficiently accurate to reproduce the experimental results for Doppler-cooled chains. It works even down to low dimensions thanks to the long-range nature of the Coulomb interactions. For this reason the predictions of Landau theory for the linear-zigzag transition are confirmed by several experimental results within the level of accuracy permitted by the temperature and the measurement apparatus. The possibility of cooling relatively long chains close to the zero-point motion paves the way for verifying the effects of quantum fluctuations at the linear-zigzag transition. Close to the transition, in fact, the competing influences of the Coulomb interaction and the confining potential balance each other out, and fluctuations are expected to become significant. Retzker *et al.* (2008) discussed tunneling across the linear-zigzag transition for an anisotropic trap that confines the motion of the ions on a plane. By means of a field-theoretical model that was postulated on the basis of plausible assumptions, the tunneling rate between the two symmetry-broken zigzag ground states were estimated for chains of a few ions. Zhang *et al.* (2023) experimentally revealed quantum tunnelling between zigzag configurations in a chain composed of three to five ^{171}Yb ions and confined by a linear Paul trap. Figure 17 displays the spectroscopic signal of a Raman transition resolving the anharmonic spectrum of excitations of the zigzag mode, which demonstrates the effect of quantum dynamics.

Shimshoni, Morigi, and Fishman (2011a, 2011b) derived a quantum field-theoretical model for an anisotropic potential, such as that of Zhang *et al.* (2023), that pins the zigzag orientation in the x-y plane. The procedure permits the quantum linear-zigzag transition to be mapped to an Ising model in a transverse field. The derivation incorporates quantum fluctuations in the classical model [Eq. (45)] and leads to a $(1+1)$-dimensional quantum field theory described by the partition function $Z=\int \mathcal{D}\phi e^{-S[\phi]/\hbar}$ with the Euclidean action (Shimshoni, Morigi, and Fishman, 2011a)

$$S[\phi]=\int_0^{\hbar\beta} d\tau \sum_{j=1}^{N}\left[\frac{1}{2}m(\partial_\tau\phi_j)^2+V_0(\phi_j)+\frac{1}{2}K(\phi_j-\phi_{j+1})^2\right], \tag{46}$$

where $\beta=1/k_{\mathrm{B}}T$ is the inverse temperature. Equation (46) is mapped to a quantum Ising model by writing the continuous field $\phi_j=\bar{\varrho}\sigma_j^z+\delta\phi_j$, where σ_j^z can take the values ±1, which corresponds to approximating the double well (and, equivalently, the displacement of the ions from the chain axis) with a spin, and $\delta\phi_j$ are the fluctuations. When the fluctuations $\delta\phi_j$ are integrated out, the model takes on the form of a quantum transverse field Ising model that is described by the Hamiltonian

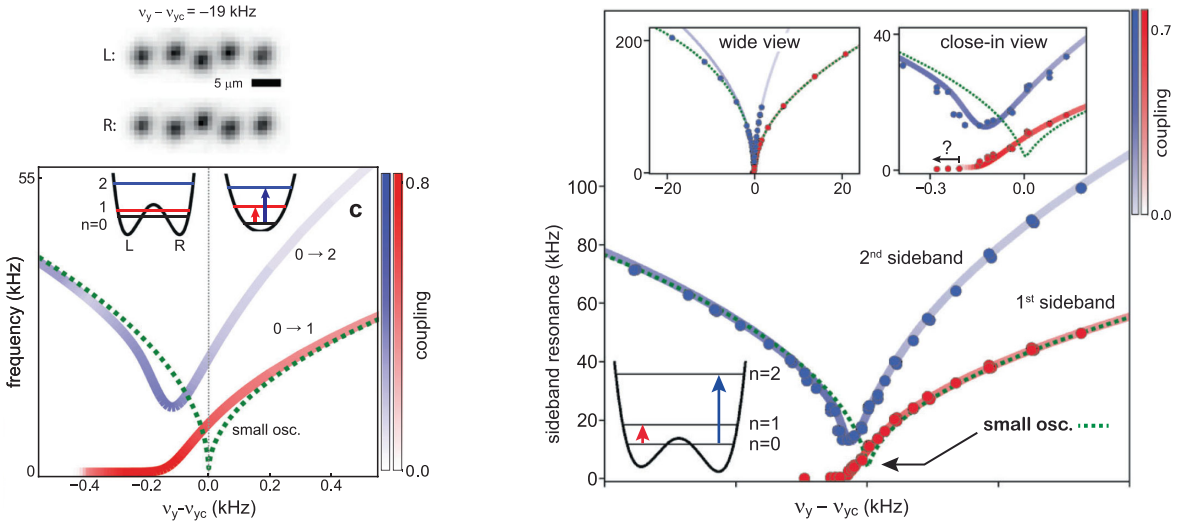

FIG. 17. Top left panel: sample images of the two symmetry-broken equilibrium structures of the five ^{171}Yb ion crystals far from the critical point. Bottom left panel: simulated quantum energy-level spectrum for the first two excited states of the transverse-y zigzag mode of a four-ion crystal that is calculated relative to the ground state. Color shading of the levels indicates the strength of Raman sideband coupling to the ground state for a central ion (see the sidebar scales: the right-handed bar for $0 \to 1$ and the left-handed bar for $0 \to 2$). Also shown is the classical small-oscillation prediction and the form of the zigzag potential on either side of the transition. Right panel: measured frequency of the first and second upper Raman sidebands for the transverse-y zigzag mode as a function of the secular trap frequency ν_y relative to the critical value $\nu_{y,c} = 760$ kHz. The solid lines are quantum energy-level differences of $n = 1$ and 2 number states with respect to the $n = 0$ ground state for a quartic potential. The line shading corresponds to the Raman coupling strength (see the sidebar scale). The dotted green line shows the classical small-oscillation prediction for the full pseudopotential. Insets: full range of data acquisition and an enlarged view near the critical point. From Zhang *et al.*, 2023.

$$H_{\mathrm{I}} = -\sum_{j=1}^{N} (J\hat{\sigma}_j^z \hat{\sigma}_{j+1}^z + h\hat{\sigma}_j^x), \tag{47}$$

where the spin-flip operator $\hat{\sigma}_j^x$ describes the tunneling between the two minima. The magnetic field is $h = \hbar\Delta\omega/2$ and is proportional to the tunnel splitting $\hbar\Delta\omega$ of a quantum particle in the double-well potential. The interaction strength J takes the form

$$J = K\bar{\varrho}^2 = K\frac{m}{4\mathcal{A}}(\nu_t^{(c)2} - \nu_t^2), \tag{48}$$

with $\bar{\varrho}$ given in Eq. (44). Following Eq. (48), the ratio h/J is controlled by the dimensionless parameter

$$\varepsilon = (\nu_t^{(c)} - \nu_t)/\nu_t^{(c)}, \tag{49}$$

which encodes the shift of the trap frequency from its mean-field critical value of Eq. (42).

The Ising Hamiltonian of Eq. (47) is known to have a zero-temperature quantum phase transition at $h_c = J$ (Sachdev, 2011) that corresponds to a finite positive value of the critical detuning, $\varepsilon_c > 0$; this implies a shift of the critical trap frequency below the putative mean-field value. For $h < J$ (corresponding to $\varepsilon > \varepsilon_c$), the ground state has a nonzero expectation value of $\hat{\sigma}_z$, indicating zigzag order, whereas for $h > J$ (corresponding to $0 < \varepsilon < \varepsilon_c$), the expectation value vanishes. Furthermore, on both sides of the transition, the spectrum of excitations is separated by an energy gap Δ from the ground state. However, the gap softens as the transition is approached from either side, as $\Delta = 2|J - h| \propto |\varepsilon - \varepsilon_c|$. This yields the phase diagram shown in Fig. 18. Note that the phase transition is confined to a single critical point on the $T = 0$ axis. However, on the ordered side of the quantum critical point ($\varepsilon > \varepsilon_c$) for T below the gap Δ (the dashed line in Fig. 18), zigzag correlations are maintained up to an exponentially long correlation length $\xi \propto e^{\Delta/T}$. Hence, for chains with a finite number of ions N, at sufficiently low

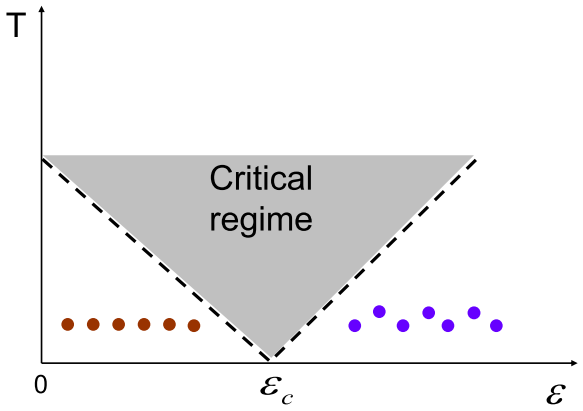

FIG. 18. Phase diagram for a linear-zigzag transition according to a mapping to the quantum Ising chain, where T is the temperature and ε is as defined in Eq. (49). The quantum critical point at $\varepsilon_c > 0$ separates the linear from the zigzag phase at $T = 0$. For $0 < \varepsilon < \varepsilon_c$ quantum fluctuations dominate, and the crystal is in the linear (disordered) phase. The dashed lines indicate the boundaries of the quantum critical region. From Shimshoni, Morigi, and Fishman, 2011a.

	Quantity	Computed (Silvi et al, 2013)	Theory
η	Anomalous dimension	0.258 ± 0.012	0.25
β	Spont. magnetization	0.126 ± 0.011	0.125
ν	Correlation length	1.03 ± 0.05	1
c	Central charge	0.487 ± 0.015	0.5

FIG. 19. Computed critical exponents and central charge of the action in Eq. (46). The theoretical values are those of the Ising model in a transverse field; see Sachdev (2011). From Silvi *et al.*, 2013.

temperatures, the zigzag correlations can exceed the system size and extend throughout the full chain, giving the appearance of long-range order. In contrast, on the disordered side ($\varepsilon < \varepsilon_c$), the correlation length ξ remains finite for all $T \geq 0$. For $T \to 0$, it diverges upon approaching the transition: $\xi \sim |\varepsilon - \varepsilon_c|^{-1}$. Finally, a critical regime emerges for $T > \Delta$, where the correlation length is controlled by the temperature, $\xi \propto 1/T$, and correlations at distances smaller than ξ decay as a power law (Sachdev, 2011).

The mapping of Shimshoni, Morigi, and Fishman (2011a) was numerically verified by means of a density matrix renormalization group (DMRG) analysis (Silvi *et al.*, 2013, 2014), a technique designed for studying quantum many-body systems in one-dimensional lattices, which was used to simulate a lattice version of Eq. (46). Figure 19 reports the critical exponents, the central charge and the corresponding error. The excellent agreement with the values of the Ising model in the transverse field confirms that the quantum linear-zigzag transition belongs to the critical Ising model universality class.

The quantum theory predicts a critical point that is shifted from the mean-field value $\nu_t = \nu_t^{(c)}$ ($\varepsilon = 0$). The shift scales with the ratio between the kinetic and the Coulomb energy,

$$\tilde{\hbar} = \frac{\hbar}{\sqrt{maQ^2 \log 2}}, \tag{50}$$

where the dimensionless variable $\tilde{\hbar}$ is the effective Planck constant. For typical parameters of ion chains, ε takes values ranging between 10^{-5} and 10^{-4}; see Silvi *et al.* (2013). The smallness of the effective Planck constant imposes demanding experimental conditions for observing the quantum critical behavior. The required temperatures are found by estimating the gap of the double-well potential, giving $T[\mathrm{mK}] \ll 1/[4n_A^{2/3}(a/a_0)^{5/3}]$, with n_A the atomic number and $a_0 = 1$ μm a reference interparticle distance, corresponding to sub-Doppler-cooling temperatures (Shimshoni, Morigi, and Fishman, 2011a).

Podolsky *et al.* (2014) computed the shift ε_c as a function of the small dimensionless parameter $\tilde{\hbar}$. This was perfomed by rewriting the partition function $Z = \int \mathcal{D}\phi e^{-S[\phi]/\hbar}$ in the form

$$Z = \int \mathcal{D}\tilde{\phi} e^{-\tilde{S}[\tilde{\phi}]/\tilde{\hbar}}, \tag{51}$$

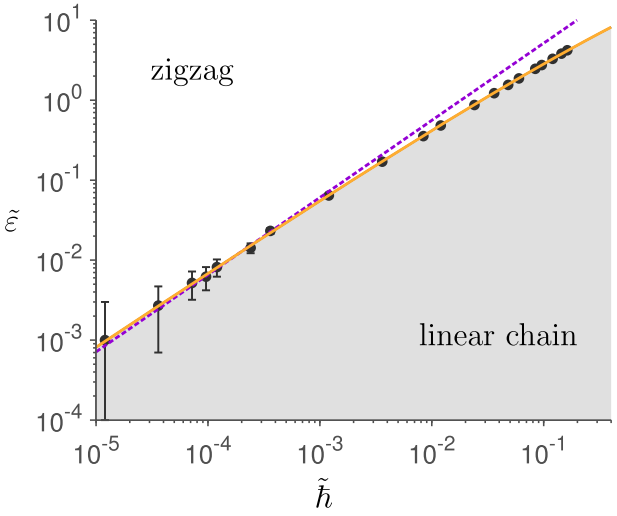

FIG. 20. Phase diagram in the $(\tilde{\hbar}, \tilde{\varepsilon})$ parameter space for $g \simeq 6.027$. The black dots are the critical points $\tilde{\varepsilon}_c(\tilde{\hbar})$ calculated via DMRG along with estimated uncertainties. The solid orange curve is a fit to Eq. (53) with $\log \tilde{\hbar}^* = 2.632 \pm 0.008$. By comparison, the dashed violet curve is a power-law fit to $\tilde{\varepsilon}_c \propto \tilde{\hbar}^{\zeta}$ restricted to data in the narrow interval $[10^{-5}, 3 \times 10^{-4}]$ with fitted exponent $\zeta = 0.97 \pm 0.05$. From Podolsky *et al.*, 2014.

where $\tilde{S}$ is a dimensionless action written in terms of the rescaled field $\tilde{\phi}(x, \tau) = \phi(x, \tau)/a$,

$$\tilde{S}[\tilde{\phi}] = \tfrac{1}{2} \int d\tilde{\tau} d\tilde{x} [(\partial_{\tilde{\tau}} \tilde{\phi})^2 + (\partial_{\tilde{x}} \tilde{\phi})^2 - \tilde{\varepsilon} \tilde{\phi}^2 + g \tilde{\phi}^4], \tag{52}$$

with $\tilde{\varepsilon} = \varepsilon 7\zeta(3)/\log 2$ and $g = 93\zeta(5)/(32 \log 2)$.[2] The parameter $\tilde{\hbar}$ controls the strength of quantum fluctuations in the theory: when $\tilde{\hbar} \to 0$, the partition function is given by a saddle-point minimization of the action. This corresponds to the mean-field equations of motion, with a phase transition at the mean-field value $\tilde{\varepsilon}_c = 0$. Adding small fluctuations for a small but nonzero $\tilde{\hbar}$, one can attempt to evaluate the partition function perturbatively in $\tilde{\hbar}$. However, the leading term in this expansion exhibits a logarithmic divergence in the long-wavelength limit, implying that the shift in $\tilde{\varepsilon}_c$ is not analytic in $\tilde{\hbar}$. To sidestep the infrared divergences plaguing the perturbative expansion, a renormalization group analysis was performed by Podolsky *et al.* (2014). The resulting shift of the critical point is

$$\tilde{\varepsilon}_c \sim \frac{3g\tilde{\hbar}}{\pi} \log \frac{\tilde{\hbar}^*}{\tilde{\hbar}}, \tag{53}$$

[2]Equation (52) was obtained by taking the continuum limit of Eq. (46) after replacing the sum over sites with an integral in space and replacing the finite difference term with spatial gradients. Moreover, the position and the Euclidean time were rescaled as $\tilde{x} = x/a$ and $\tilde{\tau} = \sqrt{Q^2 \log 2/ma^3}\tau$, respectively. All factors $\log 2$ come from the value of K in Eq. (45). They did not appear in the expressions of Podolsky *et al.* (2014).

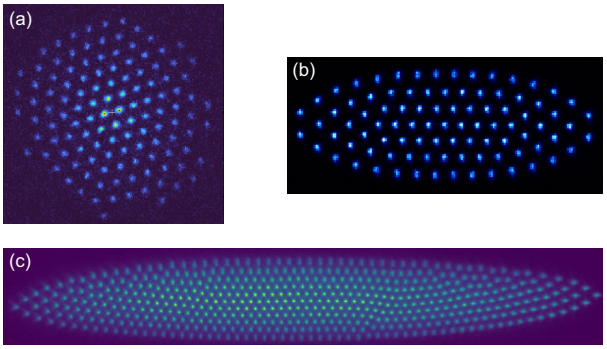

FIG. 21. Examples of 2D trapped-ion crystals formed in the laboratory. In all cases the image is obtained in a direction normal to the plane. (a) Two-dimensional ion crystal with 121 $^{9}Be^{+}$ ions formed in a Penning trap. The average ion-ion spacing is approximately 35 μm. From Wolf *et al.*, 2024. (b) Two-dimensional ion crystal with 91 $^{40}Ca^{+}$ ions formed in an rf trap operated in a lateral configuration; see Sec. II.B.1. The average ion-ion spacing is approximately 6.5 μm. From Kiesenhofer *et al.*, 2023. (c) Two-dimensional ion crystal with 512 $^{171}Yb^{+}$ ions formed in an rf trap operated in a lateral configuration. The average ion-ion spacing is approximately 4 μm. From Guo *et al.*, 2024.

where $\tilde{\hbar}^{*}$ is a nonuniversal number. This result is predicted to be asymptotically exact for small $\tilde{\hbar}$ and is confirmed by numerical simulations using the DMRG program of Silvi *et al.* (2013, 2014). Figure 20 displays the numerical results and the prediction of Eq. (53), showing agreement over the entire range of values of $\tilde{\hbar}$ considered, with a single fitting parameter $\tilde{\hbar}^{*}$.

These results indicate that the quantum critical region is small yet measurable using stable trapping potential. The shift could be revealed by means of interferometric protocols (De Chiara *et al.*, 2008; Baltrusch, Cormick, and Morigi, 2012). The critical exponents at the quantum linear-zigzag transitions could be extracted by measuring the scaling of the excess heat produced by slow quenches across the phase transition (Silvi *et al.*, 2016). This is discussed in Sec. III.D.

B. Planar geometries

Single-plane crystals of ions have been prepared in both Penning and rf ion traps by adjusting the confinement to be much stronger in one direction relative to the two orthogonal directions. Figure 21 shows some representative examples. In contrast to ion chains, cooling of single-plane crystals near the ground state of the transverse motion has been demonstrated only recently (Jordan *et al.*, 2019; Kiesenhofer *et al.*, 2023; Guo *et al.*, 2024; Pham *et al.*, 2024). We note that two-dimensional ion crystals are at the basis of protocols for realizing robust quantum information processing (Taylor and Calarco, 2008; Baltrusch, Negretti *et al.*, 2011). They have been employed in quantum simulation experiments of long-range Ising spin models, producing entanglement of the internal spin degrees of freedom (Bohnet *et al.*, 2016; Gärttner *et al.*, 2017), and in the preparation of geometrically frustrated ground states (Qiao *et al.*, 2022; Guo *et al.*, 2024). Two-dimensional ion crystals have also been used to simulate spin-boson models (Safavi-Naini *et al.*, 2018; Gilmore *et al.*, 2021).

In this section, after reviewing the different trap configurations for preparing 2D ion crystals, we discuss their thermodynamic (ground-state configuration) and dynamic (normal mode) properties, and the structural instability when a single-plane crystal transitions to multiple planes. Many of the results of this section can be applied to single-plane crystals in rf traps in the limit in which the pseudopotential approximation holds and micromotion can be neglected.

1. Trap configurations

The effective confining potential of an ion trap used to prepare trapped-ion crystals can typically be written as

$$V(x,y,z) = \tfrac{1}{2}m\omega_z^2(z^2 + \beta_x x^2 + \beta_y y^2), \tag{54}$$

where (x,y,z) denote coordinates along the principal axes of the confining potential and relative to the center of the trap. Harmonic confinement is assumed, which is typically a good approximation. For a Penning trap (see Sec. I.B.2), (x,y,z) are coordinates in the rotating frame of the crystal, with z denoting the distance along the magnetic field axis. For a linear rf trap, V denotes the confining pseudopotential and z indicates the distance along the nodal line in the center of the trap that is free from rf fields; see Sec. I.B.1. Single-plane crystals have been prepared in a variety of trap configurations that are now summarized.

In Penning traps single-plane ion crystals are formed in the plane perpendicular to the magnetic field of the trap by adjusting $\beta_x, \beta_y \ll 1$. This is achieved by controlling the crystal rotation frequency to produce a weak radial confinement compared to the axial confinement; see Fig. 7. The relative strength of β_x and β_y is set by the strength of the rotating wall electric field. Typically, $\beta_x \sim \beta_y$, giving rise to crystal shapes that are approximately circular. Single-plane crystals of up to 400–500 ions have been produced and controlled in Penning traps (Mitchell, Bollinger, Dubin *et al.*, 1998; Mavadia *et al.*, 2013; Ball *et al.*, 2019). Readout of the spin state of an individual ion in a single experiment (McMahon *et al.*, 2024; Wolf *et al.*, 2024) and how to address individual ions (McMahon *et al.*, 2024) in the rotating frame of the crystal have been demonstrated.

As with the Penning trap, single-plane crystals have been prepared in rf traps by adjusting the confinement in the axial $(\hat{z})$ direction to be strong compared to the confinement in the radial direction (Drewsen *et al.*, 2003; Richerme, 2016; D'Onofrio *et al.*, 2021; Kato *et al.*, 2022). With traps operated in this configuration (a *radial configuration*), single-plane crystals of up to ∼50 ions have been prepared and well characterized. Another approach for forming 2D ion crystals is to weaken the confinement in a direction transverse to the axis of a linear rf trap (Block *et al.*, 2000; Bermudez *et al.*, 2012; Kaufmann *et al.*, 2012; Szymanski *et al.*, 2012; Wang *et al.*, 2020; Qiao *et al.*, 2022; Kiesenhofer *et al.*, 2023). Starting with an ion chain along the $\hat{z}$ direction, weakening the lateral confinement in the $\hat{y}$ direction results in a 2D zigzag structure, as discussed in Sec. II.A.4. By further weakening the lateral confinement and carefully controlling of the relative

confinement strengths in the transverse and axial directions to ensure that $1 < \beta_y \ll \beta_x$, single-plane ion crystals that have an approximate elliptical shape are obtained; see Figs. 21(b) and 21(c). With traps operating in this lateral configuration, single-plane crystals of up to 150 ions have been observed in a surface electrode trap (Szymanski *et al.*, 2012). Stable crystal structures have been realized and studied with up to 105 ions in a three-layer rf trap operated at room temperature (Kiesenhofer *et al.*, 2023) and with up to 512 ions in a monolithic three-layer trap operated at cryogenic temperatures (Guo *et al.*, 2024).

In contrast to chains of ions in the linear rf trap, single-plane crystals in rf traps undergo substantial micromotion. In both the previously discussed radial and lateral configurations, the driven micromotion of the ions at the rf drive frequency can be designed to lie in the plane of the ion crystal (Richerme, 2016; Kiesenhofer *et al.*, 2023). A beneficial feature of the lateral configuration is that the trap can be designed such that the micromotion occurs in a single direction (Kiesenhofer *et al.*, 2023), which enables micromotion-free interactions with laser beams from more than one direction.

2. Ground-state configuration

The ground-state equilibrium configuration of a single-plane, trapped-ion crystal is an approximate triangular lattice (Dubin, 1989, 1993; Schiffer, 1993) like the one shown in Fig. 22. In the interior of the ion crystal, the ions arrange themselves at the vertices of equilateral triangles, which is characteristic of an infinite 2D system. Such triangular lattices have frequently been called *hexagonal planes* in the literature, a name that emphasizes the sixfold symmetry of the lattice.

For a harmonic trap potential such as Eq. (54), the 2D number density of a single-plane crystal is inhomogeneous and decreases from the center to the boundary of the crystal. For simplicity, consider the azimuthally symmetric confinement potential [see Eq. (22) in Sec. I.B.2]

$$V(\rho, z) = \tfrac{1}{2} m\omega_z^2 (z^2 + \beta\rho^2), \tag{55}$$

which was obtained with $\beta_x = \beta_y \equiv \beta$. Single-plane ion crystals are formed in the $\hat{z} = 0$ plane of the trap when $\beta \ll 1$. For a single-plane crystal of N ions, β must be less than a critical $\beta_c(N) \approx 0.665/\sqrt{N}$ (Dubin, 1993). We can estimate the radial dependence in the 2D number density of a single-plane crystal by considering three-dimensional crystals formed in the potential of Eq. (55). This potential produces a crystal in a spheroidal volume of axial extent $2Z_p$ and diameter $2R_p$ with constant, three-dimensional density n_0 given by

$$n_0 = \frac{\epsilon_0 m}{Q^2}\omega_z^2(1 + 2\beta). \tag{56}$$

See Eqs. (19) and (23). For this spheroidally shaped crystal, the 2D number density per unit area $\sigma(\rho)$ is

$$\sigma(\rho) = \sigma\sqrt{1 - \rho^2/R_p^2}, \tag{57}$$

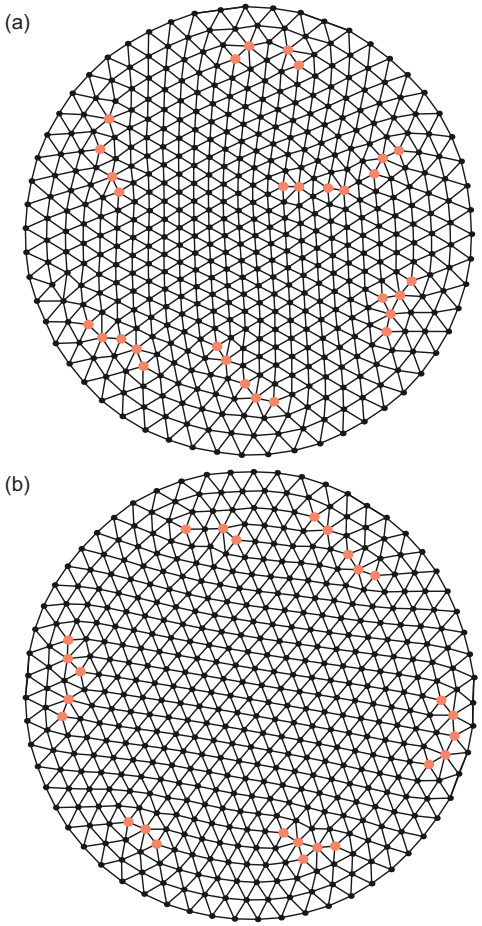

FIG. 22. Charge distribution in the ground state of a two-dimensional ion crystal. The dots correspond to the local minimum energy configuration evaluated numerically for $N = 500$ identical charges in (a) a purely quadratic trap potential and (b) a quadratic trap potential plus a lowest-order anharmonic moment ($C_4 \neq 0$) designed to generate a more uniform lattice in the interior of the crystal. The enlarged red dots indicate dislocations in the crystal lattice. From Dubin, 2013.

where $\sigma = n_0 2Z_p$ is the 2D number density at the center. Equation (57) provides a good estimate of the 2D number density of a single-plane crystal obtained in the limit of small Z_p/R_p. This expression for the inhomogeneity in the 2D number density of a single-plane crystal is analogous to Eq. (28) for the inhomogeneity in the linear density of chains of ions.

In the thermodynamic limits $\beta \to 0$ and $R_p \to \infty$, the crystal is a triangular lattice with the constant planar density σ. The single plane has a lattice constant $a_{\rm lat} = (2/\sqrt{3}\sigma)^{1/2}$ (Dubin, 1989, 1993) and is stabilized by the transverse potential $V(\rho, z) = m\omega_z^2 z^2/2$ for $\sigma a_0{}^2 \lesssim 1.11$, where $a_0 \equiv [(Q^2/\epsilon_0)/m\omega_z^2]^{1/3}$ is a characteristic length derived from the ratio between the Coulomb interaction and the transverse confinement (Dubin, 1993). Note that $a_0^{-3} = n_0$ in Eq. (56) for $\beta = 0$.

For finite planes the inhomogeneous charge density of single-plane ion crystals is necessarily associated with dislocations. They are illustrated by red dots in Fig. 22(a) (Dubin, 2013). Near the boundary of the planar crystal, shells are

formed that conform to the overall symmetry of the confining potential (Dubin and O'Neil, 1988). The shell structure is typical for systems with long-range interactions (Bubeck *et al.*, 1999). For azimutally symmetric potentials, the shells are circular and the locations of ions in neighboring shells is staggered; see Fig. 22. This shell structure has a different symmetry than the underlying triangular lattice and contributes to the formation of dislocations.

The number of dislocations in the interior of the crystal can be reduced by modifying the confining potential through the addition of anharmonic terms, thereby approaching a regular triangular lattice. The configuration of Fig. 22(a), for instance, can be made more regular by adding a fourth-order term to the harmonic confining potential. The resulting structure is presented in Fig. 22(b) for an optimized potential and in a configuration relevant for the Penning trap. The fourth-order term is frequently called a C_4 term. Structures even closer to uniform triangular lattices can be achieved by adding corrections to the confining potential with the same underlying symmetry as the target structure. In Penning traps the symmetry of the boundary is determined by the symmetry of the rotating wall potential. Theoretical studies have indicated that a nearly perfect triangular lattice can be obtained by fine-tuning the strength of an $m = 3$ rotating wall potential (Dubin, 2013), where m refers to the azimuthal symmetry of the applied rotating wall potential ($\propto \cos[m(\phi + \omega_r t)]$); see Eq. (25). Experimental work demonstrated that this strategy leads to the formation of more regular ion crystals in Penning traps (McMahon *et al.*, 2024). Overall, these strategies are at the early stages of experimental investigation.

3. Normal modes

In the following we discuss the normal modes of single-plane ion crystals. We assume that the ions are confined to a single plane via a harmonic, conservative potential. The discussion applies to single-plane crystals in Penning traps and linear rf traps; in the latter, micromotion is neglected and the pseudopotential approximation is assumed to be valid.

We start with the normal modes of an infinite, single-plane ion crystal. This is an idealization that provides intuition for understanding the normal modes of finite-size, two-dimensional structures. In the infinite triangular lattice, the equilibrium positions are $\boldsymbol{\rho} = [(n_1 + n_2/2)\hat{x} + (\sqrt{3}/2)n_2\hat{y}]a_{\rm lat}$, with n_1 and n_2 integers. The normal modes are waves with wave vector $\mathbf{k}$ in the x-y plane and displacements proportional to $\exp(i\mathbf{k}\cdot\boldsymbol{\rho})$. For every $\mathbf{k}$ there are three different polarizations: two are in the x-y plane, while the third is in the $\hat{z}$ direction, perpendicular to the plane. For example, consider the two in-plane modes when $k_y = 0$. They have polarizations in the $\hat{x}$ and $\hat{y}$ directions corresponding to the compressional and transverse modes. Their dispersion relation, along with the dispersion relation for oscillations normal to the plane, is displayed in Fig. 23 for $\sigma a_0^2 = 1.07$ and at the instability of the single plane ($\sigma a_0^2 = 1.11$). Note that the bandwidth of the in-plane modes overlaps with the bandwidth of the mode for oscillations normal to the plane.

The dispersion relation of the in-plane modes exhibits the characteristic features of acoustic modes in solids: the frequency increases as the wavelength decreases. The longitudinal (compressional) mode displays a sublinear dispersion at long wavelengths (the $\hat{x}$ mode in Fig. 23), $\omega(k) \sim \sqrt{k}$, arising from the long-range nature of the Coulomb repulsion (Stern, 1967). The dispersion relation of the out-of-plane oscillations in the $\hat{z}$ direction is similar to optical modes in solids: the mode frequency decreases as the wavelength increases. The largest frequency is the transverse confining frequency ω_z, where the crystal oscillates as a bulk. The shortest wavelengths, comparable to the inter-ion spacing, are the smallest frequencies. As shown in Fig. 23, at the single-plane stability limit ($\sigma a_0{}^2 = 1.1$), the mode frequency becomes zero at $k_x a_{\rm lat} = 4\pi/3$, producing the second-order phase transition discussed in Sec. II.B.4.

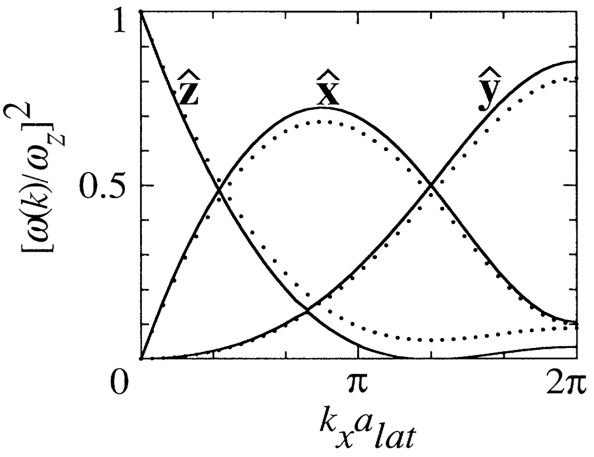

FIG. 23. Normal-mode frequencies of a single-plane triangular lattice as a function of k_x in units of the inverse of the lattice constant $a_{\rm lat} = (2/\sqrt{3}\sigma)^{1/2}$. The frequencies $\omega(\mathbf{k})$ are squared and are in units of the frequency ω_z of the transverse harmonic trap, confining the ions on the x-y plane. The modes shown are the in-plane (along $\hat{x}$ and $\hat{y}$) and the transverse (along $\hat{z}$) modes for $k_y = 0$. For the dotted lines, $\sigma a_0^2 = 1.07$, while for the solid lines, $\sigma a_0^2 = 1.11$, which corresponds approximately to the density σ where the single plane becomes mechanically unstable. The branch of the transverse modes approaches 0 for $k_x = 4\pi/3$. The phase transition of this mechanical instability is discussed in Sec. II.B.4. From Dubin, 1993.

The normal modes of trapped, single-plane ion crystals take on the character of the infinite single-plane crystal modes, including a similar dispersion relation. The general theoretical approach consists in diagonalizing the stiffness matrix, which is obtained by performing the Taylor expansion of the Coulomb potential, with some salient differences between the rf and the Penning trap due to the respective micromotion and the strong magnetic field (Wang, Keith, and Freericks, 2013; Shankar *et al.*, 2020). In rf traps some of the ions in the crystal undergo significant micromotion. Including the effects of micromotion in describing normal modes is challenging and has been incorporated in only a few studies (Kaufmann *et al.*, 2012; Kiesenhofer *et al.*, 2023). Kaufmann *et al.* (2012) found that including micromotion through a full time-dependent Coulomb theory was necessary to obtain good agreement between the measured and predicted eigenfrequencies for the in-plane mode spectrum of a three-ion crystal. Kiesenhofer *et al.* (2023) obtained some discrepancies with

the predictions of pseudopotential theory for some of the measured transverse mode frequencies of a single-plane crystal in an rf trap composed of eight ions. Theoretical calculations including micromotion did not resolve the discrepancies.

In a Penning trap, the natural frame in which to analyze the normal modes is the frame that corotates with the ion crystal. Because the nonthermal ion motion is a rigid body rotation about the trap symmetry axis, it does not impact the calculation of the normal modes, beyond adding a centrifugal potential. However, the strong magnetic field requires one to modify the theoretical procedure for determining the ion-crystal normal modes.

In general, a single-plane crystal of N ions supports $2N$ in-plane modes and N transverse modes. The latter are frequently called drumhead modes because they resemble the modes of a drum with open boundary conditions (Sawyer *et al.*, 2012; Wang, Keith, and Freericks, 2013; Shankar *et al.*, 2020). In a Penning trap, the drumhead modes for a single-plane crystal involve ion motion parallel to the magnetic field. Therefore, the magnetic field does not impact the drumhead mode frequencies or eigenvectors in the harmonic approximation, and the drumhead mode structure is the same for single-plane crystals in Penning traps and rf traps, provided that the pseudopotential approximation applies to the latter.

Figure 24 illustrates the oscillation amplitudes of the four highest-frequency drumhead modes for a single-plane ion crystal. Moving from larger to lower frequency in the figure, the highest-frequency mode is the center-of-mass (or bulk) mode where all ions in the crystal oscillate as a bulk at frequency ω_z. The next drumhead modes are tilt modes. Like the out-of-plane oscillations (the $\hat{z}$ polarization in Fig. 23) in an infinite crystal, as the normal-mode frequency decreases, so does the effective wavelength. In the short-wavelength limit, the wavelength is of the order of the lattice spacing in the interior of the crystal, and only ions in the crystal interior participate in the mode. In this spatial region, the crystal approaches a regular triangular lattice and the short-wavelength drumhead modes essentially coincide with the transverse modes of the infinite crystal. See Sawyer *et al.* (2012) and Kiesenhofer *et al.* (2023) for examples of experimental spectroscopy of drumhead modes in single-plane crystals in rf and Penning traps.

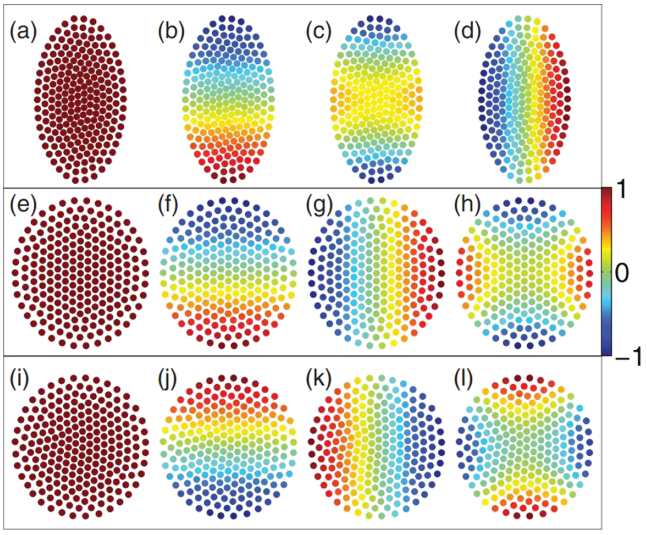

FIG. 24. The four highest-frequency drumhead mode eigenvectors calculated for a single-plane ion crystal consisting of $N = 217$ ions. The three rows correspond to three different in-plane confinement strengths. The color scale illustrates the eigenvector amplitude with the maximal value set to 1. From Wang, Keith, and Freericks, 2013.

For single-plane crystals in an rf trap, the magnetic field is nominally zero and the in-plane modes exhibit acousticlike dispersion, as with the in-plane modes of an infinite crystal (the $\hat{x}$ and $\hat{y}$ polarizations in Fig. 23). The green branch in Fig. 25 shows the results of a calculation of the in-plane mode spectrum for a single-plane crystal consisting of 120 ions in zero magnetic field (Shankar *et al.*, 2020). The calculation is performed for an rf trap in the pseudopotential approximation with an axial frequency $\omega_z/(2\pi) = 1.59$ MHz and confinement frequencies $\omega_x/(2\pi) = 0.276$ MHz and $\omega_y/(2\pi) = 0.259$ MHz in the orthogonal directions. For $N = 120$ ions, there are 240 in-plane modes, which are ordered in Fig. 25 according to increasing frequency. The lowest-frequency modes are associated with the weak asymmetry that provides azimuthal confinement, without which there would be a zero-frequency mode corresponding to rigid body rotation about

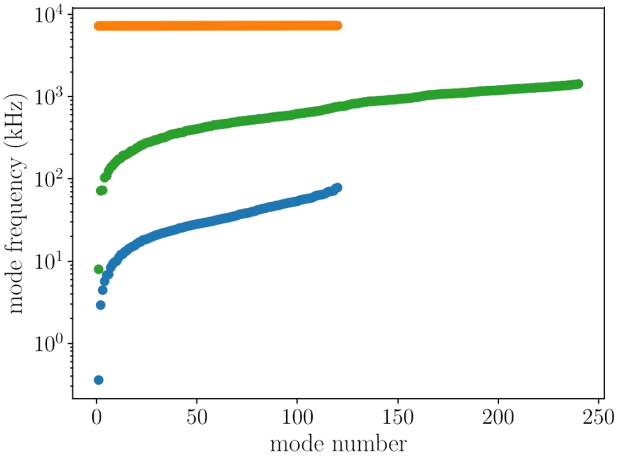

FIG. 25. Calculation of the in-plane mode frequencies for a single-plane crystal with $N = 120$ ions in the presence of no magnetic field (green central branch) and of a strong magnetic field that splits the single central branch into low-frequency (blue line) and high-frequency (orange line) branches. The central (zero-field) branch is the in-plane mode spectrum in the pseudopotential approximation for a single-plane ion crystal in an rf trap with $\omega_z/(2\pi) = 1.59$ MHz and effective confinements $\sqrt{\beta_x}\omega_z/(2\pi) = 276$ kHz and $\sqrt{\beta_y}\omega_z/(2\pi) = 259$ kHz in the orthogonal directions. The blue and orange branches are, respectively, the low-frequency $\mathbf{E} \times \mathbf{B}$ mode and high-frequency cyclotron mode spectra for the same single-plane crystal confined in a Penning trap by an identical effective potential in the rotating frame of the crystal. For the Penning trap, a cyclotron frequency $\Omega_c/(2\pi) = 7.60$ MHz, a rotation frequency $\omega_r/(2\pi) = 180$ kHz, and a weak quadrupole rotating wall potential characterized by $\omega_W = 68$ kHz are assumed; see Eq. (26). The mode frequencies are referenced to the rotating frame of the ion crystal. From Shankar *et al.*, 2020.

the $\hat{z}$ axis. The higher-frequency modes correspond to effective shorter-wavelength oscillations where ion motion becomes anticorrelated over a distance of a few inter-ion spacings.

Adding a strong magnetic field normal to the single-plane crystal (parallel to the z axis) gives rise to velocity-dependent forces. This is the case for the Penning trap. There the mode analysis becomes more involved for in-plane modes, requiring the solution of a generalized eigenvalue problem (Wang, Keith, and Freericks, 2013; Dubin, 2020; Shankar *et al.*, 2020). Figure 25 illustrates that an important consequence of the strong magnetic field is to split the single band of $2N$ in-plane modes for $B = 0$ (the green central branch) into a band of N high-frequency cyclotron modes and a band of N low-frequency $\mathbf{E} \times \mathbf{B}$ modes with a frequency on the order of the single ion magnetron frequency ω_m; see Sec. I.B.2.

In a frame that corotates with the ion crystal, individual ions in the cyclotron modes undergo an approximately clockwise circular motion about their equilibrium positions. In contrast, the $\mathbf{E} \times \mathbf{B}$ modes on average exhibit counterclockwise motion (Shankar *et al.*, 2020). Movies that show the eigenvectors of the planar normal modes of a single-plane crystal in a Penning trap were included in the Supplemental Material of Wang, Keith, and Freericks (2013). In the rotating frame, both the cyclotron modes and the $\mathbf{E} \times \mathbf{B}$ modes are positive-energy modes. They exhibit the conventional property that an increase in mode amplitude corresponds to an increase in mode energy. However, the $\mathbf{E} \times \mathbf{B}$ and cyclotron modes are more complicated than the drumhead modes, which, in the linear approximation, behave like N independent simple harmonic oscillators. In contrast to a simple harmonic oscillator, the time-averaged kinetic and potential energies are not equal for the cyclotron or the $\mathbf{E} \times \mathbf{B}$ modes. The cyclotron modes are dominated by kinetic energy, whereas the $\mathbf{E} \times \mathbf{B}$ modes are dominated by potential energy. In the normal-mode analysis of Fig. 25, which employs conditions relevant for recent experimental work (Shankar *et al.*, 2020) with $^9Be^+$ and parameters $(\Omega_c, \omega_z, \omega_r)/(2\pi) = (7.60, 1.59, 0.180)$ MHz, the ratio of potential to kinetic energy for a typical $\mathbf{E} \times \mathbf{B}$ mode is of order 200, while the ratio of potential to kinetic energy for a typical cyclotron mode is 0.005.

The large magnetic field of a Penning trap therefore produces a separation of thermal fluctuations into potential energy fluctuations that are captured mainly by the $\mathbf{E} \times \mathbf{B}$ branch and kinetic energy fluctuations that are captured predominantly by the cyclotron branch. This separation has consequences for Doppler laser cooling. In fact, Doppler laser cooling exploits the dependence of the scattering rate on the velocity via the Doppler shift, and therefore efficiently cools the cyclotron motion. In contrast, the $\mathbf{E} \times \mathbf{B}$ modes are dominated by the potential energy associated with positional fluctuations of the ions from their equilibrium positions and are therefore inefficiently laser cooled. In addition, recent simulations have shown that the equilibration rate between the cyclotron branch and the $\mathbf{E} \times \mathbf{B}$ branch is exponentially weak in the ratio of the frequency of the cyclotron branch to the $\mathbf{E} \times \mathbf{B}$ branch ($\sim\Omega_c/\omega_m$) (Tang *et al.*, 2021).

Evidence for elevated temperatures of the $\mathbf{E} \times \mathbf{B}$ mode has been obtained from simulations (Johnson *et al.*, 2024) and from the measurement of the broadening of the spectrum of the drumhead modes, which is sensitive to fluctuations in the ion positions (Sawyer *et al.*, 2012; Sawyer, Britton, and Bollinger, 2014; Shankar *et al.*, 2020). This is motivation for developing techniques for improved measurements of the temperature of the in-plane modes, in particular, for the $\mathbf{E} \times \mathbf{B}$ modes, and generalizing techniques like "axialization" (Phillips *et al.*, 2008), which use time-dependent electric field gradients to couple and equilibrate the cyclotron and magnetron motions of a single or a few ions stored in Penning traps. Doppler-cooling simulations of single-plane ion crystals in a Penning trap have indicated that efficient cooling of the $\mathbf{E} \times \mathbf{B}$ modes is possible when the bandwidths of the $\mathbf{E} \times \mathbf{B}$ and drumhead modes overlap through appropriate tuning of the ion-crystal parameters (Johnson *et al.*, 2024).

4. Structural instability of the planar geometry

Single-plane crystals are strictly two-dimensional geometries that are stable provided that the transverse confinement is sufficiently strong. By decreasing the transverse trap strength below a critical value, the plane becomes unstable and the crystal undergoes a transition to a three-dimensional structure (Dubin, 1993). This instability is driven by the drumhead modes at the lowest frequency and manifests itself in the formation of a three-plane structure, as illustrated in Fig. 26. We call this structure the *buckled phase*, and we call the transition into this phase the *buckling transition*.

The theoretical prediction of the buckling transition of Dubin (1993) is based on minimization of the potential energy. The condition for stability of the single-plane structure can be written as $\sigma a_0^2 \lesssim 1.1$, where a_0 is the characteristic length emerging from the competition between the Coulomb repulsion and the transverse harmonic confinement. Equivalently, stability requires the trap frequency ω_z to exceed the value ω_z^{MF}, with

$$\omega_z^{\mathrm{MF}} \approx \left(\frac{13.36Q^2/(4\pi\epsilon_0)}{Ma_0^3}\right)^{1/2}. \tag{58}$$

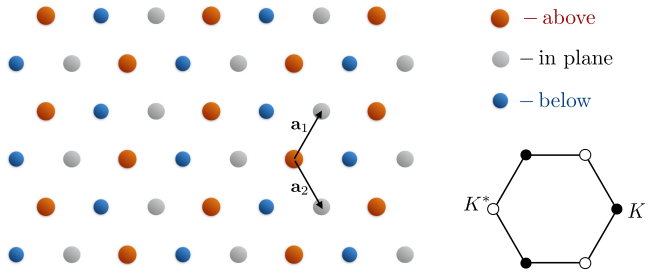

FIG. 26. Single-plane, triangular crystal undergoing a so-called buckling transition to three planes, each with a triangular structure. Left panel: height pattern in the ordered phase. The triangular lattice is split into three sublattices, one in the $z = 0$ plane (medium gray circles), one above it (large red circles), and one below it (small blue circles). There are $3! = 6$ inequivalent configurations corresponding to the possible height assignments to the sublattices. Right panel: first Brillouin zone of the single-plane crystal together with the wave vectors of the height pattern $\mathbf{K}$ and $\mathbf{K}^* = -\mathbf{K}$. From Podolsky *et al.*, 2016.

This analysis predicts a direct phase transition from the planar to the buckled phase, which is of second order.

Owing to their large mass, ions typically have negligible kinetic energy compared to their potential energy. However, at the buckling transition, where the Coulomb and confining potential energies balance each other, kinetic energy becomes disproportionately significant. This leads to thermal and quantum fluctuations that alter the nature of the buckling instability. The role of ion kinetic energy in the buckling transition was examined in the field theory analysis of Podolsky *et al.* (2016). This theory predicts that the transition from one to three planes occurs via a two-stage process where the planar (disordered) and buckled (ordered) phases are separated by an intermediate, partially ordered phase. This behavior is captured by mapping the field theory onto a six-state clock model, a well-studied framework in statistical physics (José *et al.*, 1977; Oshikawa, 2000; Lou, Sandvik, and Balents, 2007). We now review the basic steps leading to the mapping and its predictions.

The first step of the field theory analysis is to identify the order parameter of the buckled phase. The pattern shown in Fig. 26, for example, is encoded by the expression

$$z_i = \mathrm{Re}[\psi e^{i\mathbf{K}\cdot\boldsymbol{\rho}_i}], \tag{59}$$

where z_i is the transverse displacement of ion i from the plane, $\boldsymbol{\rho}_i$ is its in-plane lattice vector, and $\mathbf{K} = (4\pi/3a_{\mathrm{lat}}, 0)$ is the wave vector at the corner of the Brillouin zone. In Eq. (59) $\psi = |\psi|e^{i\theta}$ is a complex-valued field that serves as an order parameter. The amplitude $|\psi|$ determines the height of the buckling modulation, and the phase θ dictates the in-plane position of the maximal height modulation. The requirement that one of the three sublattices remains level at $z = 0$ (see Fig. 26) implies that there is an energetic preference for θ to take one of the discrete values $\theta = \pi(2n+1)/6$, where $n \in \{1, \ldots, 6\}$.

This suggests a mapping to the six-state clock model (José *et al.*, 1977; Oshikawa, 2000; Lou, Sandvik, and Balents, 2007). The mapping is performed for transverse frequencies ω_z near the mean-field critical value ω_z^{MF} [Eq. (58)]. In this regime the displacements z_i and, consequently, $|\psi|$ remain much smaller than the in-plane interparticle distance, which allows corrections to the planar Coulomb interaction to be incorporated via a multipole expansion. By assuming that the complex-valued order parameter $\psi(\boldsymbol{\rho}, t)$ varies slowly in space and time, one can employ a gradient expansion by treating the discrete planar distribution as a continuum. This leads to the Ginzburg-Landau (GL) functional expressed in terms of $\psi(\boldsymbol{\rho}, t)$, whose form is constrained by the symmetries of the triangular lattice. The explicit formulation of the GL model was given by Podolsky *et al.* (2016). Here we present its form when the transverse trap frequency ω_z falls below the mean-field threshold ω_z^{MF}. In this regime the order parameter ψ acquires a finite amplitude, $|\psi| = |\psi_0|$, that is effectively described by the mean-field model. Meanwhile, the phase dynamics of $\theta(\boldsymbol{\rho}, t)$ is governed by the Lagrangian density,

$$\mathcal{L}_{\mathrm{GL}} = \frac{\rho_s^0}{2}\left(\frac{1}{c^2}|\partial_t\theta|^2 - |\nabla\theta|^2\right) - h_6\cos(6\theta), \tag{60}$$

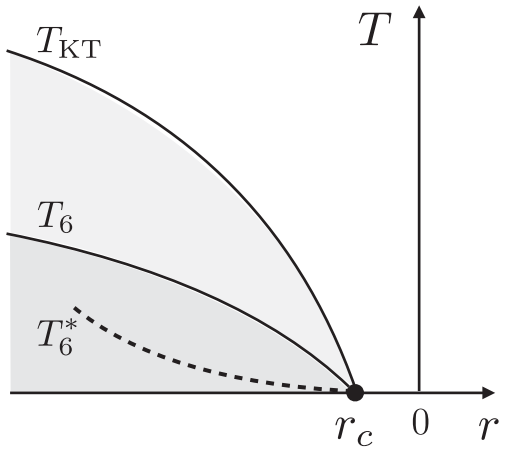

FIG. 27. Phase diagram of the structural instability of a planar ion crystal in the parameter space determined by the temperature T and $r = \omega_z - \omega_z^{\mathrm{MF}}$. For $r > 0$ the ions form a stable, single-plane crystal. At $r < 0$, in the white region, the transverse structure is disordered because of either thermal (for $T > 0$) or quantum ($T = 0$) fluctuations. The external line at T_{KT} separates the disordered phase from a critical phase, where the ions are distributed along three layers and exhibit quasi-long-range order in the transverse direction. The second line at T_6 indicates the onset of the long-range ordered buckled phase, where the ions arrange in three static planes, as illustrated in Fig. 26. The value $r_c < 0$ indicates the critical point at $T = 0$. The dashed line at T_6^* is a crossover separating quantum and classical behaviors within the ordered phase. From Podolsky *et al.*, 2016.

where the parameters ρ_s^0, c, and h_6 depend on ω_z and the characteristics of the single-plane crystal. The Lagrangian density in Eq. (60) determines both the thermal and quantum phases of the six-state clock model.

Figure 27 illustrates the phase diagram as a function of two control parameters: the temperature T and the transverse trap frequency, here expressed as the difference $r = \omega_z - \omega_z^{\mathrm{MF}}$ from the mean-field value ω_z^{MF}. At finite temperatures the model predicts a two-stage thermal transition. At high temperatures, for $T > T_{\mathrm{KT}}$ the system remains in a fully disordered phase where ions undergo thermal fluctuations around the single-plane structure. In this phase correlation functions of the atoms' heights decay exponentially with distance and time. At low temperatures below a critical temperature denoted by T_6, the system enters a fully ordered phase where the ions' equilibrium positions form a static, three-plane buckled structure. Both transitions are of the Kosterlitz-Thouless (KT) type, with critical temperatures determined by the conditions

$$T_{\mathrm{KT}} = \frac{\pi\rho_s(T_{\mathrm{KT}})}{2}, \qquad T_6 = \frac{2\pi\rho_s(T_{\mathrm{KT}})}{9}, \tag{61}$$

where ρ_s denotes the renormalized stiffness. In the intermediate regime $T_6 < T < T_{\mathrm{KT}}$, a critical phase emerges where the height correlations decay as a power law (on top of oscillations at the wave vector $\mathbf{K}$ of the buckling structure),

$$\langle z(\boldsymbol{\rho})z(0)\rangle \sim |\boldsymbol{\rho}|^{-\eta}\cos(\mathbf{K}\cdot\boldsymbol{\rho}), \qquad \eta = \frac{T}{2\pi\rho_s}. \tag{62}$$

Noting that $0 < \eta < 1/4$, we see that this phase exhibits quasi-long-range order of the buckled structure.

As the temperature T decreases, quantum fluctuations become increasingly dominant, ultimately driving a phase transition at a single quantum critical point $(T = 0, r = r_c)$ (Oshikawa, 2000; Lou, Sandvik, and Balents, 2007). For temperatures above $T_6(r)$, the clock term $\cos(6\theta)$ in Eq. (60) is effectively suppressed by fluctuations. Consequently, the model describing the transition corresponds to the quantum XY model in two space dimensions, implying that the stiffness ρ_s scales as r approaches r_c according to

$$\rho_s(r,T) = \Delta\Phi(T/\Delta), \qquad \Delta \sim |r - r_c|^{\nu}, \tag{63}$$

where $\nu \approx 0.671$ and $\Phi(x)$ is a universal scaling function of a single variable x that remains nearly constant for $x \leq 1$. As a result, the values of T_{KT} and T_6 (and thus the extent of the critical intermediate phase) shrink as r approaches r_c, ultimately vanishing together at the quantum critical point $r = r_c$ at $T = 0$; see Fig. 27.

For a finite but sufficiently small T, a crossover occurs within the ordered phase from classical to quantum behavior at a temperature $T_6^* < T_6$. This signifies the emergence of an additional characteristic length scale, $\xi_6 \sim 1/T_6^*$, beyond which the long-range clock order becomes apparent (Oshikawa, 2000; Lou, Sandvik, and Balents, 2007). The clock term influences the system's dynamics by introducing a gap due to breaking of the continuous phase-displacement symmetry of θ. This gap, of order T_6^*, is strongly suppressed as the system approaches the quantum critical point.

The experimental signatures of the predicted phases are the measurement of the layer separation and the structure form factor. The layer separation h associated with the formation of the three planes serves as a measurable probe of the order parameter. In particular, tracking its behavior as a function of T and r can distinguish the three phases. In addition, it is suggestive of the classical-quantum crossover at T_6^*. For a given $r < r_c$, the value T_6^* can be identified with the temperature scale at which $h(T)$ saturates to a constant value. The structure form factor provides information on the enlargement of the unit cell, signaled by additional Bragg peaks, and on the critical KT phase. The latter becomes visible in the height and line shape of the peaks as a function of the temperature, which are expected to exhibit a power-law dependence (Podolsky *et al.*, 2016). Small layer separations can be detected by means of interferometric measurements based on spin-motion entanglement (Baltrusch, Cormick *et al.*, 2011; Baltrusch, Cormick, and Morigi, 2012; Gilmore *et al.*, 2021). The structure form factor is accessed by Bragg scattering measurements (Itano *et al.*, 1998; Dantan *et al.*, 2010).

In currently available 2D ion crystals, experiments have not yet unambiguously revealed the occurrence of the buckled phase, but its verification, while challenging, is possibly within reach. We now provide some estimates of the required experimental conditions. Sufficiently far from the quantum critical point r_c, the critical temperatures T_{KT} and T_6 [which are of the same order of magnitude; see Eq. (61)] are found to be 2 orders of magnitude smaller than the Coulomb energy, yielding ∼10 mK for typical interparticle distances on the order of 15 μm. Tracking of their shrinking as $r \to r_c$ and accessing the lower-temperature scale T_6^* would require temperatures to be cooled down on the order of hundreds of microkelvin. This regime is accessible using available sub-Doppler-cooling techniques (Eschner *et al.*, 2003; Lechner *et al.*, 2016). A more serious limitation arises due to the finite size of the crystal. Present experiments can realize planes with $N \sim 1000$ ions corresponding to linear sizes of $L \sim 30$ ions (although an ordered triangular lattice is typically formed on a smaller scale). In this regime finite-size effects will strongly affect the observations. However, as Podolsky *et al.* (2016) argued, a systematic finite-size-scaling analysis can be utilized to perform a meaningful comparison with the theory.

C. Three-dimensional crystals

Three-dimensional trapped-ion crystals have been prepared in Penning and rf ion traps since the early days of laser cooling (Diedrich *et al.*, 1987; Wineland *et al.*, 1987; Gilbert, Bollinger, and Wineland, 1988). While 1D and 2D ion crystals have been limited to ∼500 ions, 3D crystals can reach sizes greater than 10^5 ions (Tan *et al.*, 1995). The large sizes accessible in 3D crystals make them promising platforms for developing new control and characterization techniques. At present, however, such techniques are less mature for 3D crystals than for 1D and 2D crystals. To date, only Doppler cooling has been applied with 3D crystals. We review here the types of 3D crystal configurations that have been prepared in the laboratory, discuss the importance of finite-size effects, and summarize the characteristic properties of the vibrational motion.

1. Ground-state configuration

Before discussing the detailed structure of three-dimensional ion Coulomb crystals, it is useful to consider the cold-fluid plasma model of a single-species ion crystal in which the ions are approximated by a continuous charge distribution in space. This is also called the zero-temperature, mean-field plasma (Dubin and O'Neil, 1999). For simplicity, consider an effective harmonic confinement potential in all three dimensions, which is routinely achieved in Penning and quadrupole rf traps. At low temperatures this gives rise to ion crystals with constant density and sharp boundaries. In the cold-fluid model, the continuous charge distribution is uniform in space, with approximately the same boundary as the ion crystal. The energy required to assemble the continuous charge distribution does not scale extensively with (that is, is not proportional to) the number of trapped charges.

The cold-fluid model is useful for determining the overall crystal shape and the number of trapped ions through the volume enclosed by the crystal shape, but the specific lattice structure is dictated by the discreteness of the charges and, more precisely, by the short-distance contributions to the energy. The latter, the so-called correlation energy, scales extensively with the lattice size. Three-dimensional strongly

coupled OCPs are peculiar systems in that three different lattice configurations have nearly the same correlation energy per ion in the infinite (bulk) lattice and at zero temperatures. These configurations are bcc, face centered cubic (fcc), and hexagonal close packed (hcp). The bcc lattice is the zero-temperature ground state (Brush, Sahlin, and Teller, 1966; Ichimaru, 1982), but the bulk energy per ion in the fcc and hcp configurations is less than 10^{-4} higher than that in the bcc configuration (Dubin, 1989; Baiko, Potekhin, and Yakovlev, 2001).

The near degeneracy of the bcc, fcc, and hcp lattices means that the actual ground-state configuration of finite, 3D trapped-ion crystals can be strongly impacted by boundary effects. In general, large system sizes are required for the bcc lattice to be the thermodynamic ground state. We now review the structures that have been studied and realized in the laboratory for different confinement geometries.

Spherical geometry. Consider the most symmetric case of isotropic confinement, where the confining force can be written in terms of a single force constant κ,

$$\boldsymbol{F}_{\mathrm{trap}}(\boldsymbol{r}) = -\kappa \boldsymbol{r}, \tag{64}$$

with $\boldsymbol{r}$ the spherical radius vector. Owing to the spherical symmetry of the confining potential, the global structure of finite Coulomb crystals is expected to be spherical as well. Crystals containing up to a few thousand ions minimize their potential energy as the temperature goes to zero by organizing themselves in concentric spherical shells with a specific maximum "magic" number of ions in each shell (Dubin and O'Neil, 1988; Hasse and Avilov, 1991; Schiffer, 2003; Calvo, Yurtsever, and Wales, 2012); see Fig. 28. Within each shell the ions form a two-dimensional triangular lattice (like single-plane crystals; see Sec. II.B.2), but with a number of defects to account for the curvature of the surface (see Fig. 28). The ground-state (zero-temperature) configurations are traditionally found using Monte Carlo methods or molecular dynamics simulations combined with careful annealing procedures. It is challenging, however, to determine the absolute ground-state configurations already for a modest number of ions (∼100) since, as is well known from cluster physics, the number of slightly excited metastable configurations increases exponentially with the particle number. Combined with the small deviations from a perfect harmonic confining potential in real experiments, predictions for the exact structures obtained experimentally become extremely challenging.

The uncertainty in the predicted magic numbers of ions within each shell is so small, however, that when observing a given spherical shell structure for crystals consisting of up to ∼1000 ions in the laboratory, one can typically obtain an estimate of the number of ions with an uncertainty smaller than the square root of the number of ions. Hence, measurements of the crystal structure provide a reliable way to obtain information on the number of ions in a real crystal.

Ellipsoidal and spheroidal geometries. A similar shell structure is obtained for the more general ellipsoidal ion-crystal shapes (or spheroidal if the confinement in two orthogonal directions is equal[3]). The Coulomb potential energy of the crystal is minimized by forming a shell on the boundary of the crystal that conforms with the overall crystal shape determined by the confining potential. This shell structure propagates into the interior of the ion crystal through the formation of commensurately shaped shells of a smaller size. Experimentally, shell structures are routinely observed in trapped 3D ion crystals (Gilbert, Bollinger, and Wineland, 1988; Drewsen *et al.*, 1998; Hornekær and Drewsen, 2002; Schmid *et al.*, 2022). See Fig. 29 for experimental images.

(a)

N	Structure
2	2
3	3
4	4
5	5
6	6
7	7
8	8
9	9
10	10
11	11
12	12
13	12+1
61	48+12+1
147	93+41+12+1
309	163+90+43+12+1
565	256+160+93+43+12+1
900	356+247+154+92+38+12+1

(b)

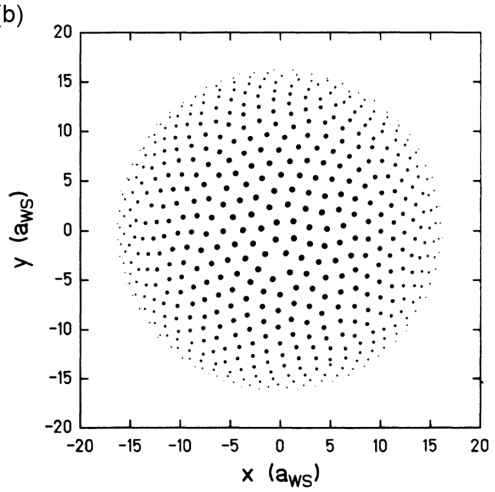

FIG. 28. Molecular dynamics simulations of spherical symmetric confined ion Coulomb crystals. (a) Shell structure as a function of the number of ions N. When a plus sign appears in the Structure column, this indicates that a new shell has started forming. In this case N is the corresponding *magic number*. In all simulations the final Coulomb coupling parameter Γ is larger than 10^5. (b) Illustration of the position of the ions in the outer shell of a 5000-ion system. Note the general hexagonal structure with a few point defects, such as the one below the center. The length scale is the Wigner-Seitz radius a_{WS}. From Hasse and Avilov, 1991.

[3]A spheroid is the shape obtained by rotating an ellipse about one of its principal axes.

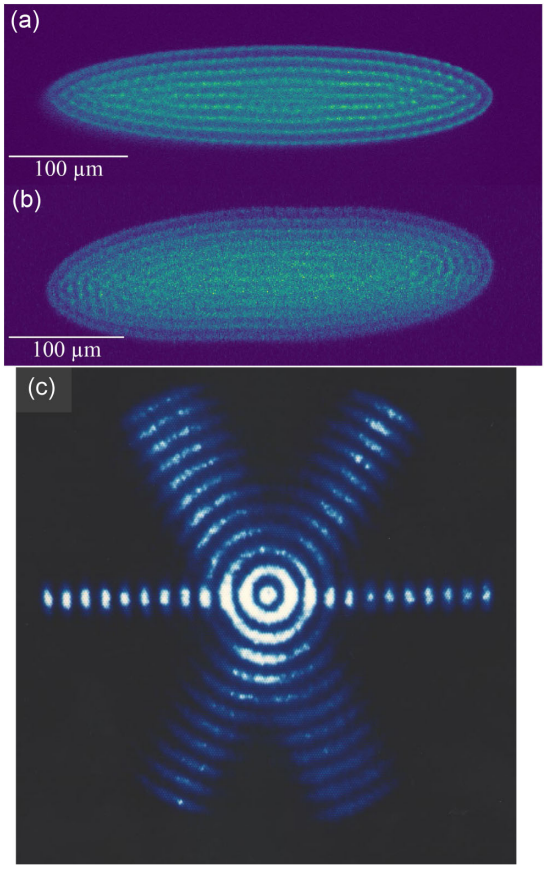

FIG. 29. Images of the ion fluorescence from trapped-ion crystals exhibiting shell structure. (a) Horizontal and (b) vertical views of an ion crystal consisting of about 2000 Be^+ ions stored in a linear rf trap. From Schmid *et al.*, 2022. (c) Image of the ion fluorescence from three laser beams directed through the center of an $N \approx 15\,000$ Be^+ ion crystal that exhibits shell structure. The ions are stored in a Penning trap and the image, averaged over many rotations of the ion crystal, is obtained along the magnetic field or rotation axis of the ion crystal. The crystal diameter is 0.6 mm. From Gilbert, Bollinger, and Wineland, 1988.

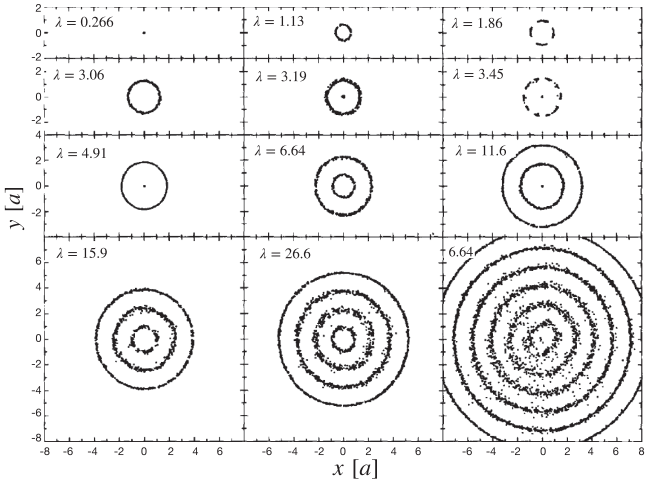

FIG. 30. Molecular dynamics simulation of cross sections of cylindrically confined Coulomb crystals for various normalized linear charge densities λ. For the lowest charge density, $\lambda = 0.266$, the charged particles form a one-dimensional string (a single dot in the cross-section view), whereas as the charge density increases, an increasing number of concentric shells, sometimes with a central string, form. Adapted from Hasse and Schiffer, 1990, who provided further details on the simulations.

An interesting question is as follows: At what size will it become energetically favorable for an ion crystal to have a bcc lattice as its ground-state configuration? Molecular dynamics simulations with spherical OCPs indicate that the spherical bcc crystal has lower energy than the shell structure for $N > 10^4$. The simulations were performed independently by Totsuji *et al.* (2002) and Hasse (2003), with ion numbers ranging from a few thousand to greater than 10^5 ions. Note that if the molecular dynamics simulation started with randomly distributed ions and was slowly annealed, a formation of spherical shells was always observed that advanced from the boundary of the crystal to the center. On the contrary, starting with a spherical cutout of a bcc lattice and then annealing resulted in a bcc crystal in the interior surrounded by a few shells at the boundary.

Experimentally, stable bcc crystals have been observed in the interior of large ion crystals formed in Penning traps through Bragg scattering of the laser-induced resonance fluorescence, as well as through direct imaging of the ion resonance fluorescence (Bollinger *et al.*, 2000). Long-range 3D periodic order was observed in approximately spherical crystals with as few as $N \approx 5 \times 10^4$ ions (Tan *et al.*, 1995). The crystal diameter was $\sim 70 a_{\mathrm{WS}}$, where a_{WS} is the Wigner-Seitz radius defined in Eq. (2). With $N > 2 \times 10^5$ ions (crystal diameter $> 130 a_{\mathrm{WS}}$), bcc crystals were the only type of 3D periodic crystal that was reported by Itano *et al.* (1998). This investigation could place only a crude lower limit on the observed bcc crystal size of $20 a_{\mathrm{WS}}$, which is a small fraction of the entire ion-crystal size. In linear rf traps, stable fcc and bcc crystalline structures have also been observed through fluorescence imaging in Coulomb crystals with more than 10^4 ions (Mortensen *et al.*, 2006).

Cylindrical geometry. A different trapping situation for three-dimensional crystals is realized when the ions are confined by an isotropic harmonic potential in two dimensions while being free to move along the third dimension. Here the parameter governing the crystal structure is the linear density of charged particles along the unconfined axis. For low linear densities, the minimum energy states are concentric cylindrical shell structures with varying surface structures within the shells. As the linear density increases, the core forms lattice structures that are translationally invariant along the axis; see Fig. 30.

In the laboratory this idealized situation cannot be fully implemented. It can effectively be realized by choosing a ring-shaped two-dimensional rf quadrupole trap, as pioneered by Birkl, Kassner, and Walther (1992) and Waki *et al.* (1992); see Fig. 31. As long as the ring's circumference is much larger than the typical ion-ion distance and the radial extent of the crystal, only small deviations from the ideal infinite situation are expected.

More surprisingly, when two different ion species are simultaneously confined in a linear rf quadrupole trap, cylindrical crystal structures that mimic those of infinitely

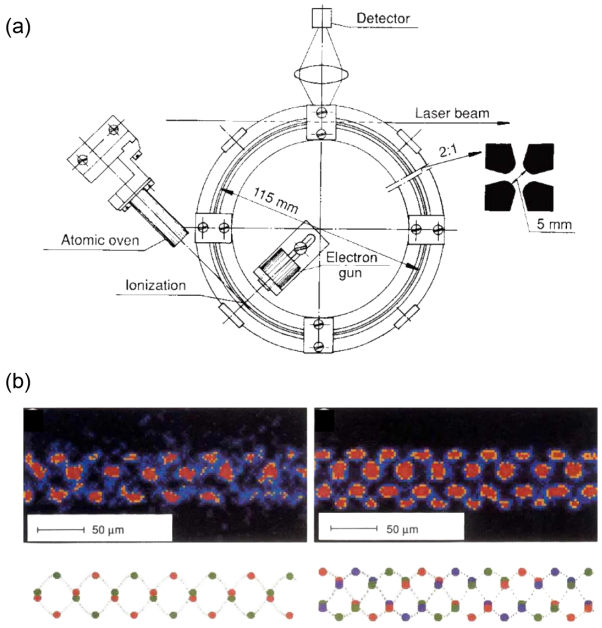

FIG. 31. Sketch of the rf ring-trap experiment used to study (a) ion Coulomb crystals under effective cylindrical confinement, together with (b) some examples of fluorescence images of ion crystalline structures (here helical structures) obtained with different linear densities. The helical structures are sketched beneath the images. See also Fig. 13. From Birkl, Kassner, and Walther, 1992.

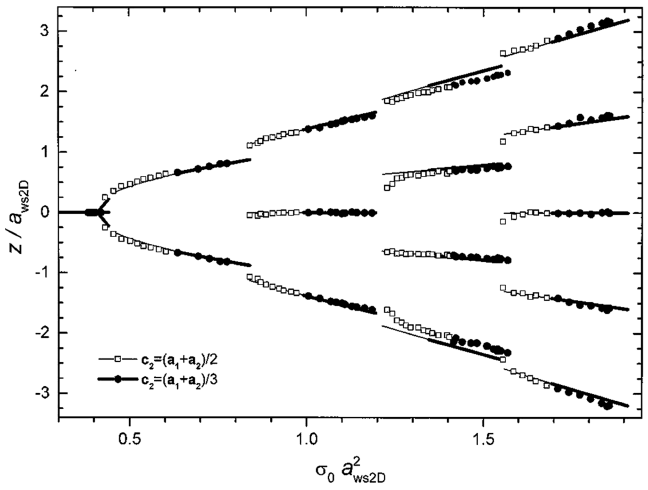

FIG. 32. Axial positions of the planes in the central region ($\rho \approx 0$) of small aspect ratio ion crystals as a function of the central areal number density. The lines show predictions from theory, and the symbols show experimental measurements. An open square (filled circle) indicates the experimental observation of a square or rhombic plane (hexagonal plane). Similarly, a thin line (thick line) indicates that theory predicts a square or rhombic plane (hexagonal plane). Lengths have been normalized by $a_{\mathrm{WS\,2D}} = (3e^2/4\pi\epsilon_0 m\omega_z^2)^{1/3}$. From Mitchell *et al.*, 1998, who defined the interlattice displacement vector $\mathbf{c}_2$.

long systems can be realized (Hornekær *et al.*, 2001). This should also be observable in Penning traps (Larson *et al.*, 1986; Imajo *et al.*, 1997). See the mention of two-species Coulomb crystals that concludes this subsection.

Slab geometry. The slab geometry consists in a uniform density OCP that is harmonically confined in one direction, $q\phi_T(\rho, z) = m\omega_z^2 z^2/2$, but infinite in the orthogonal directions. This geometry allows for a careful theoretical treatment that illustrates the importance of surface effects with 3D trapped-ion crystals (Dubin, 1989). The treatment assumes that the lattice planes that form in the $T = 0$ limit have the same symmetry. It is found that, although the bcc lattice has a lower bulk energy per ion than the fcc one, the fcc lattice has a smaller surface energy contribution than the bcc lattice, making it the lower energy lattice for thicknesses with smaller numbers of planes. Dubin showed that when the slab thickness is larger than approximately 60 planes, bcc becomes the structure that minimizes the energy, while for smaller thicknesses fcc prevails.

Experimentally, this geometry can be approximated in ion traps by adjusting the trap radial confinement to be much weaker than the axial confinement. In a Penning trap, this condition can be achieved with low rotation frequencies ω_r that are slightly higher than the magnetron frequency ω_m of the trap; see Eq. (24) and Fig. 7. For a given rotation frequency, this is the regime that gives rise to single-plane crystals for a sufficiently small number of ions; see Sec. II.B. With larger numbers of trapped ions, multiplane crystals form with an overall pancake (or lenticular) shape. The lattice planes have some curvature, but near the radial center ($\rho \approx 0$) of the trap, the planes are flat and can be compared with the structures of infinite planar systems analyzed by Dubin (1993).

Figure 32 summarizes the ion-crystal structures observed in the laboratory as a function of the 2D areal number density ($\sigma_0 a^2_{\mathrm{WS\,2D}}$) obtained by integrating over the axial extent of the crystal (Mitchell, Bollinger, Dubin *et al.*, 1998). The crystal structure was determined from direct images of the ion fluorescence from the central ($\rho \approx 0$) region of Doppler laser-cooled ion crystals with aspect ratios $\alpha \equiv Z_p/R_p < 0.1$ and ion number $N \lesssim 10^4$ ions. Figure 32 also compares the measured separation of the planes with the theory of Dubin (1993). Starting with a low 2D number density, the experiment reported single-plane crystals with a triangular lattice; see Sec. II.B.2. With increasing $\sigma_0 a^2_{\mathrm{WS\,2D}}$, theory predicts a buckling transition to three closely spaced planes that is stable over a small interval of $\sigma_0 a^2_{\mathrm{WS\,2D}}$; see Sec. II.B.4. This small region of three planes is followed by two more widely separated planes. Initially, each plane has a square and then rhombic symmetry. As the planes move farther apart, they transition into planes with hexagonal symmetry. As $\sigma_0 a^2_{\mathrm{WS\,2D}}$ increases, three planes with square symmetry eventually form and the pattern repeats. As shown in Fig. 32, the overall agreement between experimental observations with the $T = 0$ infinite extent theory of Dubin (1993) is good, with some minor discrepancies (Mitchell, Bollinger, Dubin *et al.*, 1998). One disagreement is that the transition from a single plane to a small region of three closely spaced planes was not observed. This transition is particularly interesting and serves as motivation for a more careful study at lower temperatures with new experimental tools; see Sec. II.B.4.

Note that the crystal planes with rhombic symmetry observed by Mitchell, Bollinger, Dubin *et al.* (1998) have

peculiar thermodynamic properties such as a negative Poisson's ratio. A negative Poisson's ratio means that stretching the crystal in a particular direction, in this case along the $\hat{z}$ or axial direction of the trap, causes an expansion in a lateral direction. This behavior contradicts common experience for ordinary materials that act as incompressible, such as rubber bands. Negative Poisson's ratios were measured by Baughman *et al.* (2000).

We close this section on slab geometries by pointing out that multilayer 3D crystals of trapped ions consisting of flat planes can be formed through the addition of anharmonic terms to the trapping potential. This was numerically demonstrated for crystals in Penning traps, where the anharmonic terms are additions to the usual harmonic trapping potential [see Eq. (20)] and are readily implementable in the laboratory (Hawaldar *et al.*, 2024). The formation and control of ion crystals in traps with significant anharmonic components of the trapping potential is the subject of an ongoing experimental investigation.

Two-species Coulomb crystals. As previously indicated, two-species Coulomb crystals constitute an interesting and special type of Coulomb crystal. It is instructive to draw a comparison with normal solids formed through electronic (chemical) bindings between the atomic constituencies. In this case, when more atomic species are involved, various alloys form. In contrast, in Coulomb crystals the confined ions interact mainly through the repulsive Coulomb forces at a distance that inhibits chemical bonding. Consequently, the structural organization of two simultaneously trapped-ion species is the one that minimizes the potential energy of all ions. Since, in both linear Paul (rf) traps and Penning traps, the effective confining potential in the plane perpendicular to the static confining direction depends on both the charge and the mass of a specific ion species, a two-species Coulomb crystal will generally lead to a separation of the two species with respect to this plane. This type of separation consists in the strongest bound species forming a cylinderlike central structure within an embedding spheroidal, globally shaped crystal; it was reported by Hornekær *et al.* (2001) and Mortensen *et al.* (2007). Examples are shown in Figs. 33 and 34. When the charge-to-mass ratio of the two species is the same, the species mix. This has been observed in experiments where the two trapped species were $^{26}Mg^+$ and $^{24}MgD^+$ ions (Mølhave and Drewsen, 2000). It was also reported in molecular dynamics simulations where one species has both double the mass and double the charge of the other (Matthey, Hansen, and Drewsen, 2003). In the latter case, the ground state of an infinite system is expected to be a simple cubic lattice with a unit cell consisting of one species at a corner and the other displaced halfway to the $\langle 111 \rangle$ diagonal, which is similar to chemically bound CsCl crystals in a solid state.

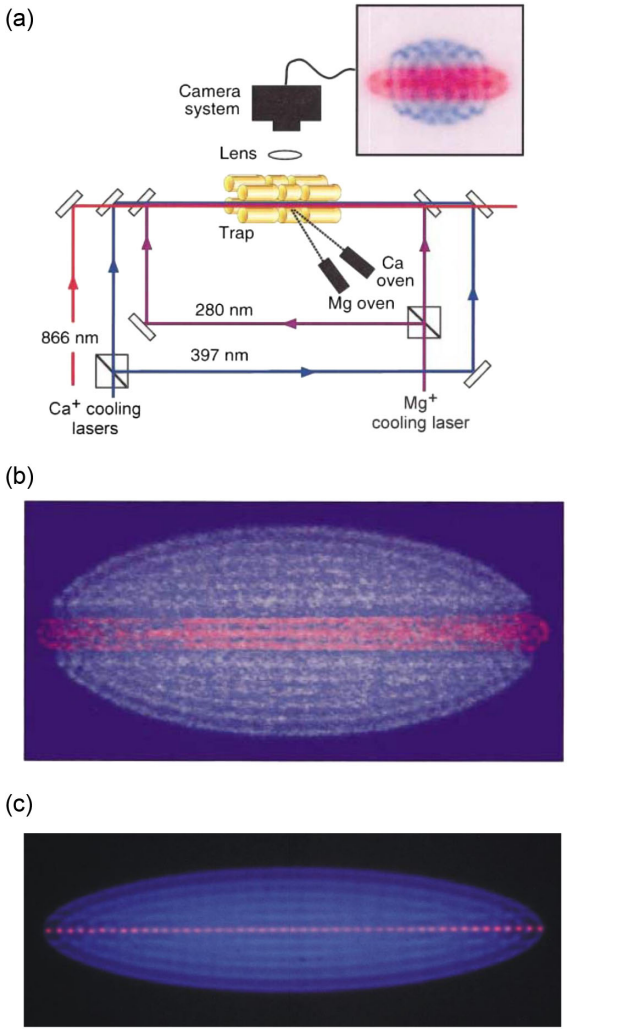

FIG. 33. (a) Sketch of a linear rf trap experiment to study two-species ion Coulomb crystals consisting of Mg^+ and Ca^+ ions. (b) Fluorescence images for 300 Mg^+ ions (red central region) and 3000 Ca^+ ions. (c) Fluorescence images for 47 Mg^+ ions and 1300 Ca^+ ions. Both crystals have a spheroidal global shape with a cylindrical symmetry axis coinciding with the central axis of the Mg^+ component. From Hornekær *et al.*, 2001.

2. Metastable and perturbation-induced structures

The theoretical analysis of the experimental results discussed thus far has assumed that the trapping potential is conservative and purely harmonic. However, this is only an approximation of the experimental situations. Specifically, in rf traps the time dependence of the trapping potential can produce measurable deviations from this idealized situation and thus impact the formation of ion-crystal structures and even the resulting structures.

For instance, in linear rf traps operated with $a_{dc} = 0$, the pseudopotential is symmetric under rotation about the z axis in the geometry of Fig. 4. However, this continuous symmetry is only an approximation of the exact discrete symmetry imposed by the four electrode configuration of the trap. The effect of this discrete symmetry is already evident in clusters composed of two ions, which are forced by a strong confining force to lie in the x-y plane. Molecular dynamics simulations [as well as expansions of the pseudopotential beyond the leading order (Drewsen and Brøner, 2000)] show that at equilibrium the two ions always align along one of the $(1,1)$ or $(1,-1)$directions in the plane, where the orientation of the micromotion is perpendicular to the line connecting the two ions. Similarly, for weak confinement along the z axis, small zigzag structures always align in the same directions.

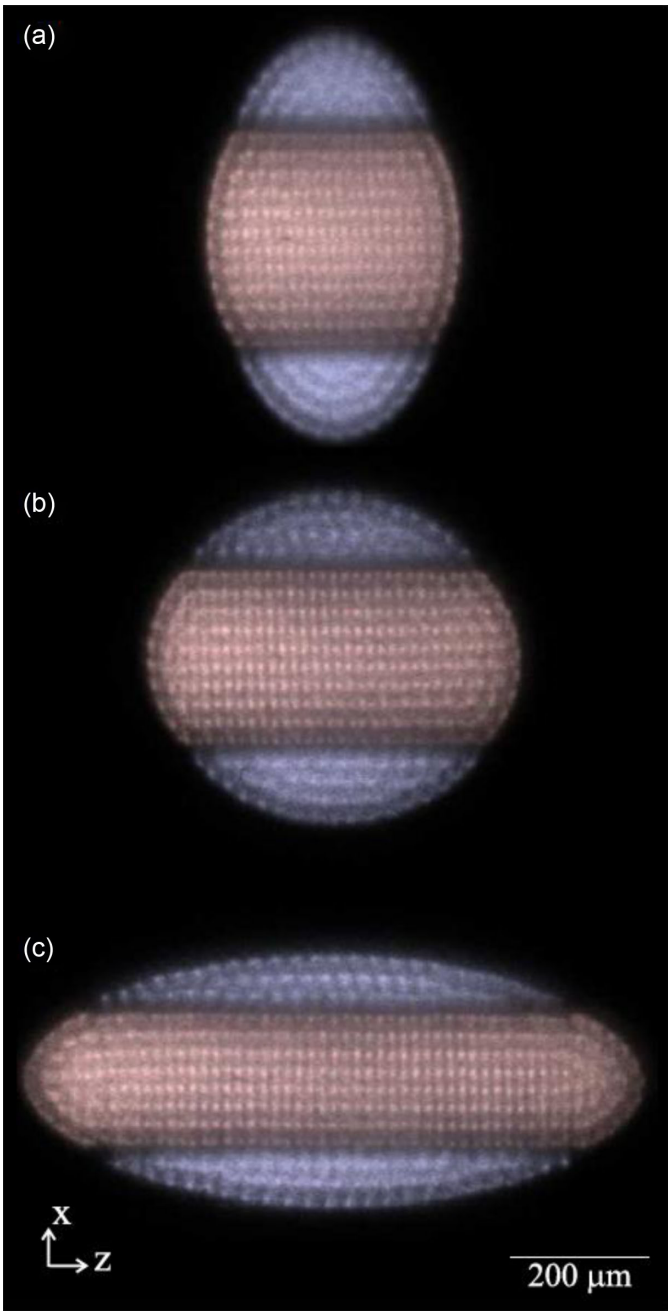

FIG. 34. Fluorescence images of two-species ion Coulomb crystals containing ∼1500 $^{40}Ca^{+}$ ions in the central region (red) and ∼2000 $^{44}Ca^{+}$ ions in the surrounding regions (blue) for the same ion densities but different trapping potential aspect ratios. From Mortensen *et al.*, 2007.

In three-dimensional ion crystals, the micromotion occurs along several directions, and the resulting order is therefore more challenging to predict. However, some general properties can be extracted from experimental evidence. Three-dimensional crystals that are laser cooled by beams propagating along the axis of the linear trap are never observed to rotate around the same axis. This occurs for single as well as multispecies crystals and indicates that the trap potential tends to pin the crystals. Moreover, translationally periodic crystal structures of single-species crystals have a propensity to occur with, for example, bcc or fcc configurations at specific orientations with respect to the trap electrodes (Mortensen *et al.*, 2006, 2007). More pronounced effects have been observed in two-species crystals consisting of two isotopes of Ca^{+} ($^{40}Ca^{+}$ and $^{44}Ca^{+}$), as shown in Fig. 34 (Mortensen *et al.*, 2007). Here the inner $^{40}Ca^{+}$ component, in addition to having a global cylindrical shape, had a persistent internal structure (presumably orthorhombic) with fixed relation to the trap electrodes and with lifetimes longer than 10 s. Similar results were found via simulations that included the full rf trap potential (Mortensen *et al.*, 2007).

The application of optically induced dipole forces (Grimm, Weidemüller, and Ovchinnikov, 2000) can generate spatially localized perturbations to the ions' trapping potential. A standing-wave light field can force the ions to localize on gratings of potential minima separated by half the laser wavelength, $\lambda/2$ (Cormick and Morigi, 2012; Enderlein *et al.*, 2012; Linnet *et al.*, 2012; Lauprêtre *et al.*, 2019; Wipfli *et al.*, 2023). In general, competition with Coulomb repulsion gives rise to frustration; see Sec. III.E. However, for crystalline structures with bcc, fcc, or hcp symmetry, one can tune these gratings so that the periodicity is commensurate with the distance between the lattice planes. Molecular dynamics simulations showed that in this way one can control the crystal structures and orientations and can adiabatically change the crystal structure from bcc to fcc structures, and vice versa (Horak, Dantan, and Drewsen, 2012). In a cylindrically symmetric pseudopotential, the radiation pressure of a single traveling laser beam that does not propagate across the trap center exerts a torque and can set the crystal into rotation. Drewsen *et al.* (2003) observed this by illuminating a crystal in an rf trap with a beam propagating within the x-y plane, but offset with respect to the center point. The measured rotational frequencies varied from zero all the way up to 98% of the radial trap frequency dependent on the specific position and detuning of the laser beam (Drewsen *et al.*, 2003); see Fig. 35 as well as Sec. III.E for details on an analogous experiment performed in Penning traps.

In rf traps a more dramatic kind of perturbation can be induced when the density of a crystal is increased to the point where the plasma frequency of the crystal ω_p becomes close to half that of the rf drive frequency Ω_{rf}, namely, when $\omega_p \sim \Omega_{\mathrm{rf}}/2$. In such situations the parametric resonances lead to heating of the crystal (Blümel *et al.*, 1989), and in many instances even to melting. However, if the crystal is set into rotation, its density and hence its plasma frequency will be lowered, and the crystal will eventually get out of parametric resonance with the rf frequency. Using appropriate laser-cooling and laser torque conditions, one can stabilize structures where the ions form rotating disks (Kjærgaard and Drewsen, 2003); see Fig. 36. A full understanding of these types of dynamics is still not available. Nevertheless, these configurations seem to satisfy a detailed balance condition between the laser-cooling and rf heating processes.

As mentioned in Sec. II.C.1, the number of ordered metastable configurations within a given energy interval typically increases exponentially with the number of ions in a Coulomb crystal. Hence, in experiments where the ions are cooled to finite temperatures, one expects to observe

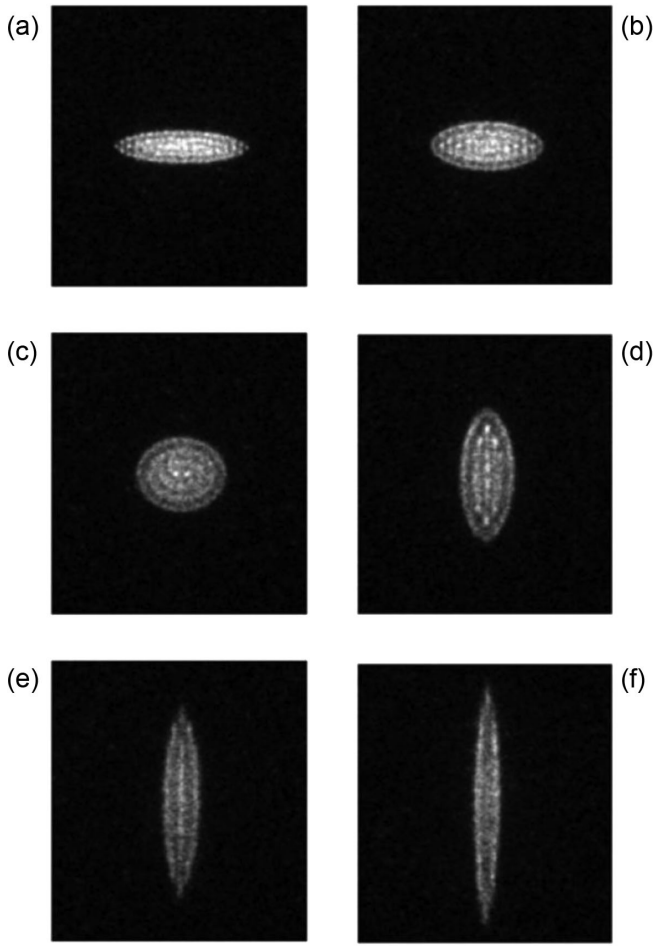

FIG. 35. Images of an ion crystal consisting of ~200 $^{24}Mg^{+}$ ions illuminated by two traveling laser beams. One laser beam propagates along the z axis and laser cools the crystal. The other beam propagates within the x-y plane such that it exerts a torque on the crystal and forces it to rotate. (a) Image corresponding to a stationary crystal. (b)–(f) Images showing rotating crystals with increasing rotational frequencies $\Omega_{\rm rot}$. (b) $\Omega_{\rm rot} = 0.4\omega_{r,\rm trap}$. (c) $\Omega_{\rm rot} = 0.7\omega_{r,\rm trap}$. (d) $\Omega_{\rm rot} = 0.9\omega_{r,\rm trap}$. (e) $\Omega_{\rm rot} = 0.96\omega_{r,\rm trap}$. (f) $\Omega_{\rm rot} = 0.98\omega_{r,\rm trap}$. (b)–(f) $\omega_{r,\rm trap} = \omega_y = \omega_x$ is the radial trap frequency. In all experiments $\omega_{r,\rm trap} = 2\pi \times 180$ kHz and $\omega_z = 2\pi \times 86$ kHz. From Drewsen *et al.*, 2003.

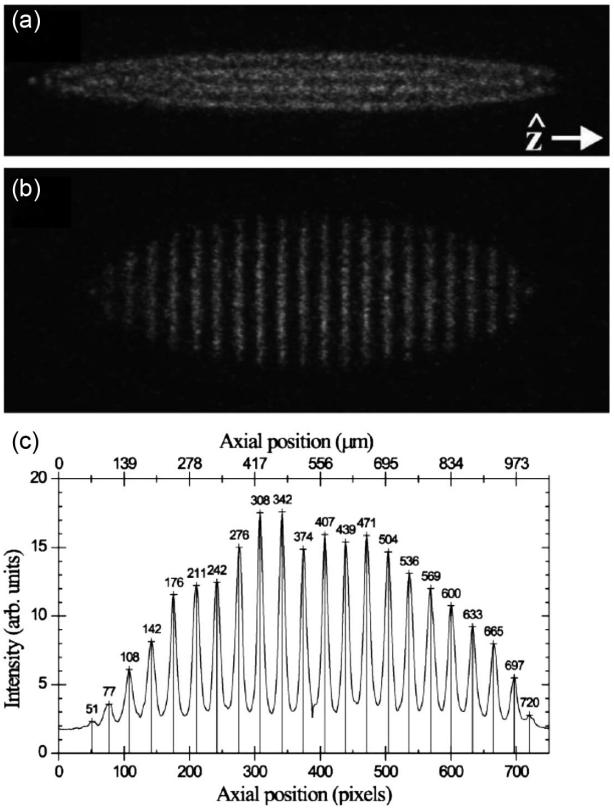

FIG. 36. Laser-cooled ion ensemble containing approximately 370 $^{24}Mg^{+}$ ions in Coulomb crystal configurations (a) just below and (b) above the $2\omega_p = \omega_{\rm rf}$ dynamical instability. (c) Integrated axial intensity distribution of the string-of-disks configuration (b) showing that the disks are near-equidistantly spaced. From Kjærgaard and Drewsen, 2003.

thermally excited metastable configurations. Figure 37 shows four images of the same cold ion ensemble of approximately 2700 ions stored in a linear rf trap. The images were recorded seconds apart, showing various 3D periodic lattice structures. They are all excited metastable configurations; for example, they correspond to energies higher than the ground-state energy. We note that Coulomb crystals as small as ~1000 ions have been observed to possess a central, metastable bcc-ordered core (Mortensen *et al.*, 2006). In Penning traps an example of a metastable structure is the fcc lattice observed in ion crystals having more than 50 000 ions (Tan *et al.*, 1995; Itano *et al.*, 1998); see Sec. II.C.1.

3. Normal modes of three-dimensional crystals

Normal-mode phonon spectra of bulk, crystalline, strongly coupled OCPs have been calculated with varying degrees of accuracy over the past six decades both in the absence (Clark, 1958; Chabrier, Ashcroft, and DeWitt, 1992; Baiko, Potekhin, and Yakovlev, 2001) and in the presence of a strong magnetic field (Usov, Grebenschikov, and Ulinich, 1980; Nagai and Fukuyama, 1982; Baiko, 2009). Interest in this area has frequently been in predicting the thermodynamic properties of dense astrophysical OCPs. As discussed, trapped-ion crystals formed and studied in the laboratory typically are not of sufficient size to form a body-centered-cubic lattice in a large fraction of the interior of the crystal. In addition, the normal modes that are most straightforwardly excited in the laboratory typically have wavelengths that are long compared to the inter-ion spacing. The dispersion relation of long-wavelength modes is insensitive to the details of the lattice structure but can be influenced by the boundary or shape of the ion crystal.

A trap geometry that is frequently employed in experimental work provides quadratic (frequently called harmonic) confinement in the axial and radial directions. See Eqs. (13) and (22). As discussed in Secs. I.B.1 and I.B.2, at low laser-cooling temperatures, a quadratic confining potential results in uniform density crystals with a spheroidal shape. Note that a simple exact analytic solution exists for the normal modes of a uniformly charged spheroid, both in the absence of and in the presence of a magnetic field. The treatment assumes that the normal-mode wavelength is long compared to the inter-ion

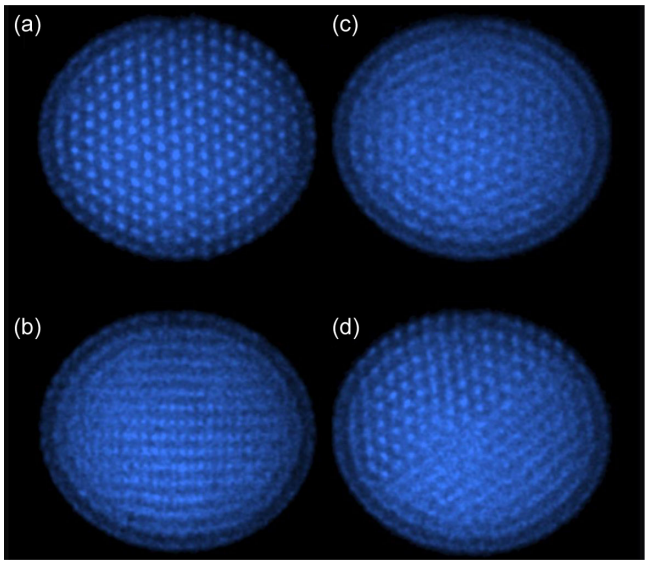

FIG. 37. Fluorescence images of metastable spheroidal Coulomb crystals containing ~2700 $^{40}Ca^{+}$ ions. (a) Dominating bcc structure viewed from the $\langle 111 \rangle$ direction. (b) Crystal structure containing a central fcc structure viewed from the $\langle 211 \rangle$ direction. (c) Crystal structures with indications of nucleations of defects at the center. (d) Crystal indicating the coexistence of bcc and fcc structures. All images were obtained with a 0.1 s integration time. From Drewsen *et al.*.

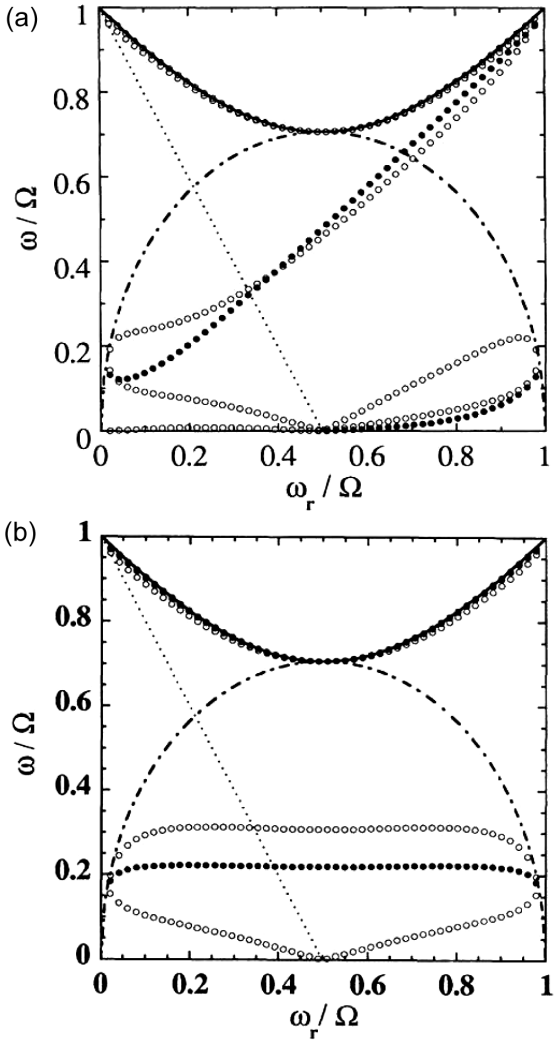

FIG. 38. Normal-mode frequencies ω in the rotating frame of the ion-crystal vs rotation frequency ω_r for $\omega_z/\Omega = 0.151$ and different values of (l, m), where $\Omega \equiv \Omega_c$ is the cyclotron frequency. Frequencies $\omega < 0$ are allowed and obtained by reflecting through the point $(\omega_r, \omega) = (\Omega/2, 0)$. For $m \neq 0$ the sign of ω determines the direction of the azimuthal motion of the mode potential. Also shown for comparison are the vortex frequency $\Omega_v(\omega_r) = \Omega - 2\omega_r$ (dotted lines), the plasma frequency $\omega_p(\omega_r)$ [see Eq. (4)] (dot-dashed curve), and the upper hybrid frequency $\Omega_u(\omega_r) = (\omega_p^2 + \Omega_v^2)^{1/2}$ (solid curve). (a) $(l, m) = (2, 1)$, filled circles; $(l, m) = (5, 1)$, open circles. (b) $(l, m) = (2, 0)$, filled circles; $(l, m) = (4, 0)$, open circles. From Bollinger *et al.*, 1993.

spacing, so the mode is well described by cold-fluid equations. See Dubin (1991) and Bollinger *et al.* (1993) for detailed descriptions of cold-fluid equations.

The modes can be cataloged by two integers l and m, where $0 \leq m < l$, following the conventions of Dubin (1993). Here l and m characterize the functional dependence of the mode potential ψ in terms of the associated Legendre functions. For example, the solution for the mode potential outside the spheroidal crystal is given by

$$\psi \propto Q_l^m(\xi_1/d) P_l^m(\xi_2) e^{i(m\phi - \omega t)}. \tag{65}$$

In Eq. (65) Q_l^m and P_l^m are associated Legendre functions, the coordinate ξ_1 is a generalized distance coordinate (similar to a spherical radius), ξ_2 is a generalized latitude (similar to the polar angle θ), ϕ is the usual azimuthal angle, ω is the mode frequency, and $d^2 \equiv Z_p^2 - R_p^2$, where $2Z_p$ is the axial extent and $2R_p$ is the diameter of the spheroid. The specification of the mode potential in the interior of the ion crystal is more complicated.

We discuss some example calculations of the $m = 1$ and $m = 0$ modes in Figs. 38(a) and 38(b), respectively. Both panels show the calculated mode frequency ω normalized to the ion cyclotron frequency Ω ($\Omega \equiv \Omega_c$ in Secs. I.B.2 and II.B) as a function of the ion-crystal rotation ω_r in a Penning trap with axial frequency $\omega_z/\Omega = 0.151$. The mode frequencies are plotted in the rotating frame of the ion crystal. For $\omega_r \sim 0$ (or $\omega_r \sim \Omega$) the ion crystal has a lenticular shape (see Fig. 7) and the mode frequencies separate into three different bands. These bands are the 3D analogues of the $\mathbf{E} \times \mathbf{B}$, drumhead, and cyclotron modes discussed in Sec. II.B.3. A difference with respect to single-plane modes is that the $\mathbf{E} \times \mathbf{B}$ modes (and, to a much lesser extent, the cyclotron modes) now acquire a component of motion that is parallel to the magnetic field (Dubin, 2020; Hawaldar *et al.*, 2024).

As ω_r/Ω increases from zero, the separation of the modes into three bands becomes less distinct. At $\omega_r/\Omega = 0.5$ the effective magnetic field in the rotating frame of the ion crystal goes to zero. At this special point, the equations of motion of the normal modes are equivalent to the ones of a spheroidal ion crystal with the same aspect ratio in an rf trap in the psuedopotential approximation, and the modes can be

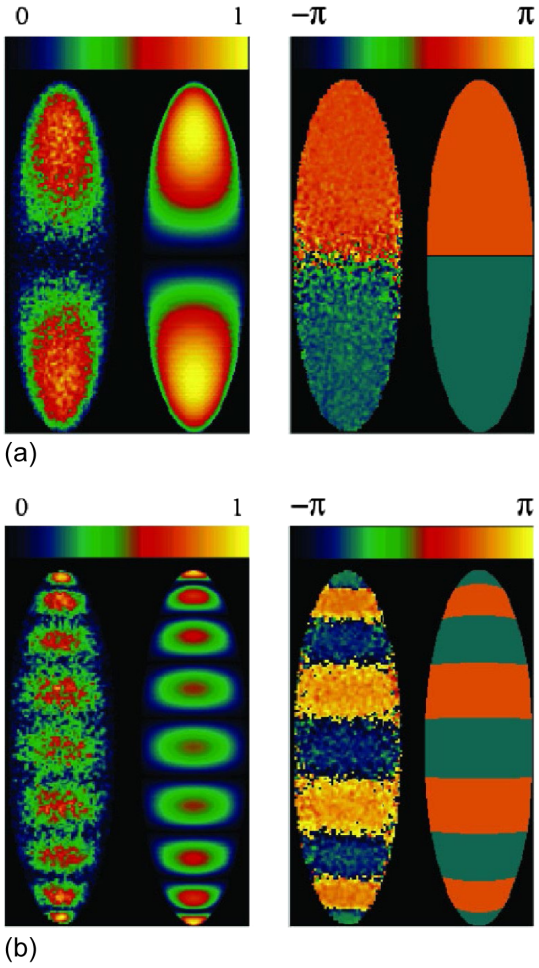

FIG. 39. Side-view image of the velocity profile of an $(l, m = 0)$ mode excited in a spheroidal, laser-cooled cloud of $^9Be^+$ ions in a Penning trap. $\omega_r/(2\pi) = 1.00$ MHz, $\omega_z/(2\pi) = 1.13$ MHz, and $\Omega/(2\pi) = 7.608$ MHz, where $\Omega \equiv \Omega_c$ is the cyclotron frequency. The magnetic field and axial laser beam point up. The ion cloud spheroidal dimensions are $2Z_p = 0.76$ mm and $2R_p = 0.24$ mm, with the density $n_0 = 2.70 \times 10^9$ cm^{-3}. At each point of the image, the measured ion resonance fluorescence is fitted to an amplitude and phase. (a) Left panel: comparison of the measured amplitude of a $(2, 0)$ mode excited at $\omega_{2,0}/(2\pi) = 1.656$ MHz with the predictions of linear theory. Right panel: comparison of the measured phase with theory. (b) Left panel: comparison of the measured amplitude of a $(9, 0)$ mode excited at $\omega_{9,0}/(2\pi) = 2.952$ MHz with the predictions of linear theory. Right panel: comparison of the measured phase with theory. From Mitchell, Bollinger, Huang, and Itano, 1998.

classified with the integers (l, m) of Eq. (65) (Dantan *et al.*, 2010). For discussions about the limits of validity of this equivalence and a mathematical analysis of modes that includes the time-dependent dynamics of rf Paul trap potentials; see Landa *et al.* (2012a, 2012b).

Experimentally, the normal modes of 3D trapped-ion crystals have been excited by applying time-dependent potentials to the trap electrodes (Mitchell, Bollinger, Huang, and Itano, 1998; Dantan *et al.*, 2010) or by means of radiation pressure (Kriesel *et al.*, 2002). Typically, the ion motion produced by exciting the mode induces Doppler shifts that can be used to detect the mode. In the work of Dantan *et al.* (2010), several $(l, m = 0)$ modes of spheroidal ion crystals stored in a linear rf trap were excited by a resonantly oscillating electrical field and the resulting Doppler shifts detected through modification of the collective coupling of the ion crystal to an optical cavity. Excellent agreement (better than 1%) was observed with the mode frequency predictions of the cold spheroidal theory of Dubin (1991). In Penning traps detection of the Doppler shifts produced by an excited mode through changes in the ion fluorescence (the so-called Doppler velocimetry) was used to measure the frequencies of modes (l, m), with l as large as 9 and m as large as 2 (Heinzen *et al.*, 1991; Mitchell, Bollinger, Dubin *et al.*, 1998).

Images of the excited mode eigenfunction of a trapped ion crystal can be obtained through the laser-induced ion fluorescence. Figure 39 shows experimentally measured images of $(2, 0)$ and $(9, 0)$ modes excited in cold spheroidal clouds of $^9Be^+$ ions in a Penning trap. In the experiment a laser beam is directed parallel to the magnetic field axis (the vertical direction in Fig. 39) with a frequency tuned below resonance with a cycling transition of $^9Be^+$. Ions moving with a velocity in the direction opposite to the laser wave vector $\mathbf{k}$ fluoresce more strongly than ions moving in the same direction as $\mathbf{k}$. By recording side-view images of the ion crystal with a photon-counting imaging camera that measures the spatial and temporal coordinates of each detected photon, it is possible to construct side-view images of the excited mode velocity profile that are phase synchronous with the external radio frequency drive used to excite the mode. A comparison of the experimental images with the theoretical predictions in Fig. 39 shows that the experiment and theory are in good agreement.

III. OUT-OF-EQUILIBRIUM DYNAMICS OF ION COULOMB CRYSTALS

Understanding how strongly correlated many-body systems reach equilibrium is a central objective of statistical physics and is essential for applications to quantum technologies. By offering a controllable environment, ion Coulomb crystals are a prominent platform for simulating models that allow verification of equilibration and thermalization hypotheses. The intrinsic physical properties make the system peculiar in itself. In fact, the unscreened Coulomb interactions make ion Coulomb crystals a unique laboratory for studying the out-of-equilibrium dynamics of long-range interacting systems that can clarify hypotheses and conjectures formulated for cosmological and plasma systems (Campa, Dauxois, and Ruffo, 2009; Defenu *et al.*, 2023). In this section we review experimental and theoretical work on out-of-equilibrium dynamics in ion Coulomb crystals. We focus, in particular, on transport and relaxation of ion Coulomb crystals after a perturbation from equilibrium, such as a slow or sudden change (quench) of the trapping parameters or of the temperature. One relevant aspect is the formation, metastability, and decay of defects and dislocations, which in ion crystals can be imaged in both real and Fourier spaces. As the concept of out-of-equilibrium dynamics is central to this section, we start by defining what can be understood as equilibrium in a trapping

environment and when the laser-cooled crystal can be said to be in a thermal state.

A. Equilibrium and temperature

In the Penning trap (see Sec. I.B), the trapping forces break time reversal symmetry and confinement is achieved by setting the ions in rotation. Collisions between the ions drive the system into a state where the ion ensemble rotates rigidly (without shear) about the symmetry axis of the trap, which is parallel to the direction of the magnetic field. Rigid body rotation has been observed in the laboratory (Brewer *et al.*, 1988; Driscoll, Malmberg, and Fine, 1988). In the frame corotating with the ions, the system can evolve into a thermal equilibrium state characterized by a global temperature (Dubin and O'Neil, 1999).

The Paul trap instead achieves confinement by means of fast-oscillating forces. Often the confinement can be characterized by a conservative potential in the pseudopotential approximation, enabling a conventional statistical mechanics description that can potentially be described by a global temperature. However, strictly speaking, the dynamics is a many-body Coulomb problem in the presence of time-dependent, periodic forces. A theoretical study accounting for the full temporal dependence of the trap unveiled the existence of ordered structures that are periodic in time and that are not otherwise captured by the pseudopotential description (Landa *et al.*, 2012a, 2012b).

The concept of temperature for characterizing laser-cooled ensembles is often convenient, albeit not strictly appropriate. Temperature is often employed as a unit of measure for the energy width of the single-particle distribution in the pseudopotential approximation (or, for Penning traps, in the rotating frame of the crystal), assuming that the crystal's degrees of freedom have equilibrated. However, the crystal is not in thermal contact with a heat bath, and the stationary state is reached through laser cooling, namely, by means of the mechanical forces associated with scattering of laser photons. This leads to two key issues. One issue, which lies at the core of laser cooling, is that the single-particle distribution is not, strictly speaking, a Maxwell-Boltzmann distribution. The second issue is intrinsic to the Coulomb crystal: even under ideal conditions, the individual vibrational modes are cooled to different temperatures, depending on the ratio between the effective linewidth and the vibrational frequency of the mode (Eschner *et al.*, 2003). The possibility of nonthermal motional distributions resulting from laser sideband cooling has been discussed in the context of optical atomic clocks, where a detailed evaluation of the motional distribution is important for characterizing time-dilation shifts (Chen *et al.*, 2017).

On longer timescales, anharmonicities can redistribute the energy between the modes leading to a thermal state (Morigi and Walther, 2001; Morigi and Fishman, 2004b). At first glance, because rf and Penning traps can routinely confine ensembles of charges of the same sign ranging from many hours to days, the achievement of global thermal equilibrium states appears to be feasible. However, depending on the details of the trap parameters, the time to equilibrate to a global thermal state can exceed even these timescales. Consider a long linear chain of ions. The confinement in the transverse direction, which is characterized by frequency ν_t [see Eq. (27)], is much stronger than the confinement in the longitudinal direction, which is characterized by frequency ν. This results in normal-mode frequencies for motion transverse to the trap axis that are much higher than the normal-mode frequencies of motion parallel to the trap axis. In this case it has been shown theoretically that the rate of equilibration between the transverse and parallel motional degrees of freedom can be exponentially small in the ratio ν_t/ν, leading to equilibration time periods that exceed many months for cold ion chains with $N > 10$ (Chen and Dubin, 1993). Physically, this result can be understood through energy conservation arguments. For large ratios ν_t/ν, the coupling between the transverse (optical) and longitudinal (acoustic) bands is a weak perturbation. In terms of vibrational quanta, an interband transition requires that several low-frequency acoustic phonons are annihilated to create a single high-frequency optical phonon. Such multiphonon processes arise as high-order terms in the Coulomb interaction and have small effective rates.

Long equilibration rates are also anticipated with single-plane crystals having a large ion number N, which require a trap asymmetry parameter $\beta \ll 1$; see Eq. (55). Finally, in Penning traps the strong magnetic field splits the normal modes that describe in-plane motion into high-frequency cyclotron modes and low-frequency $\mathbf{E} \times \mathbf{B}$ modes; see Fig. 25. Numerical studies show that the equilibration of the cyclotron and $\mathbf{E} \times \mathbf{B}$ branches is exponentially weak in the ratio of the frequencies of the two branches (Tang *et al.*, 2021).

In summary, although ion Coulomb crystals can be confined for a long time, this might not be sufficient to observe equilibration between different bands, especially when they are separated by relatively large energy gaps. Equilibration processes can be experimentally accelerated using various strategies, such as fine-tuning of the trap parameters. As a simple example, for a two-ion crystal aligned along the axis of a linear rf trap, the axial stretch mode frequency can be tuned to be approximately equal to twice the frequency of the radial rocking mode. In this case the intrinsic nonlinear Coulomb force between the ions leads to a strong nonlinear coupling between these two modes, as illustrated in Fig. 40 (Ding *et al.*, 2017). Furthermore, in a linear crystal of three ions it has been possible to tune and exploit the resonant coupling of three normal modes (Maslennikov *et al.*, 2019). In Penning traps numerical studies show that the coupling between in-plane $\mathbf{E} \times \mathbf{B}$ modes and out-of-plane drumhead modes for single-plane crystals can be strongly enhanced by tuning trap parameters so that their respective bandwidths overlap (Johnson *et al.*, 2024).

An alternative strategy accelerates the process of equilibration by inducing effective mode-mode couplings with time-dependent electric fields (Gorman *et al.*, 2014; Hou *et al.*, 2024). This has been successfully applied to the equilibration between two modes of small ion crystals. Its extension to large ion crystals with widely separated bandwidths of many modes is an area of current investigation.

We conclude by discussing temperature measurement in rf traps. Temperature is determined by extracting the kinetic energy associated with the rf-driven coherent micromotion,

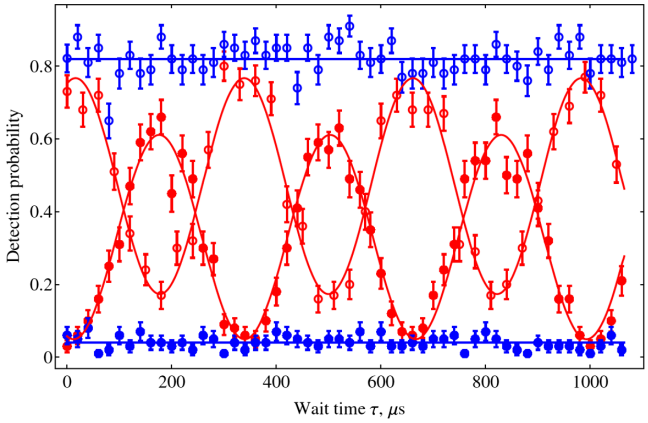

FIG. 40. Parametric coupling between an axial (a) and a radial (r) normal mode of a two-ion system. The mode frequencies are tuned such that $\omega_a = 2\omega_r$. The data points indicate the time evolution of the excitation of the axial mode (solid dots) and the radial mode (open circles) when the system is initially prepared with either one or two quanta of excitation in the radial mode. In the latter case (data points fitted by a sinusoidal solid red curve), a coherent exchange of energy is observed between the two modes. When the radial mode is initially prepared with only one quantum of excitation (data points fitted by solid horizontal blue lines), no coherent exchange is observed, and the modes are effectively decoupled. The error bars show 1 standard deviation of statistical uncertainty. From Ding *et al.*, 2017.

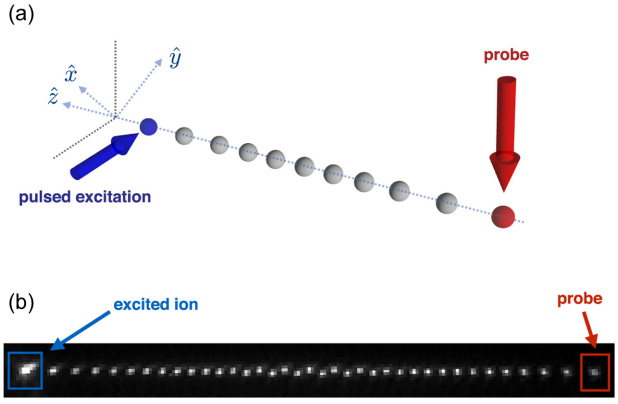

FIG. 41. Schematic of the energy transport experiment of Ramm, Pruttivarasin, and Häffner (2014). (a) An ion at the chain edge is excited by a pulsed beam (diagonal blue arrow). Following free evolution the energy is read out along the chain with a probe beam (vertical red arrow). (b) CCD image of the ion chain with 37 ions. The ions are $^{40}Ca^{+}$ and are initially Doppler cooled. The pseudopotential frequencies of the Paul trap are $(\omega_x, \omega_y, \omega_z)/(2\pi) = (2.25, 2.0, 0.153)$ MHz. The vibrations are locally excited along the x direction, which corresponds to the steepest confining potential. From Ramm, Pruttivarasin, and Häffner, 2014.

which is typically several orders of magnitude larger than the thermal motion. This can be done by recording in molecular dynamics simulations the change in the individual ion velocities at the same phase of the rf fields over time (Schiffer *et al.*, 2000). In this way one can also gain knowledge of the heating of the Coulomb crystals due to the rf drive (Blümel *et al.*, 1989; Schiffer *et al.*, 2000; Tarnas, Nam, and Blümel, 2013; Nam, Jones, and Blümel, 2014; Poindron, Pedregosa-Gutierrez, and Champenois, 2023). In experiments with 3D Coulomb crystals, where the kinetic energies of the individual ions (or, equivalently, the various normal-mode excitations) are difficult to measure, comparisons between the experimentally measured fluorescence images and those generated from molecular dynamics simulations are often a practical way to estimate the temperature (Ostendorf *et al.*, 2006; Okada *et al.*, 2010; Kiethe *et al.*, 2021).

B. Transport in trapped-ion chains

The possibility of performing normal-mode spectroscopy of an ion chain and addressing and monitoring a single ion within the chain make these systems a powerful laboratory for studying thermodynamics of and heat transport in many-body systems at the quantum level. This has led to investigations of coherent transport of excitations along ion chains varying from a few to dozens of ions, with temperatures ranging from the Doppler-cooling limit to near zero-point energies.

Coherent transport of vibrational excitations in ion chains in linear Paul traps was studied by Haze *et al.* (2012) and Ramm, Pruttivarasin, and Häffner (2014). We discuss in more detail the experiment of Ramm, Pruttivarasin, and Häffner (2014), as it is representative of the state of the art reached on the observation of these dynamics. They measured the transport of a transverse vibrational excitation along chains of $^{40}Ca^{+}$ in a linear Paul trap with a number of ions ranging from five to 37, as illustrated in Fig. 41. After initializing the chain motion to Doppler-cooling temperatures, an edge ion was excited by a laser pulse with a finite duration. The intensity of the pulse was modulated at the trap radial frequency, thereby locally exciting a transverse vibration. The dynamics of energy propagation was monitored by resolving individual ions along the chain using focused, near-resonant laser pulses to convert motional excitation to electronic excitation, which is routinely measured. The measured data are consistent with a model of coupled oscillators (or, equivalently, with a harmonic crystal). In a quantized form, the model for the vibrational dynamics along the transverse x direction reads

$$H = \sum_i \hbar\omega_{x,i} a_i^\dagger a_i + \sum_{i\neq j} \hbar t_{ij} (a_i^\dagger a_j + a_j^\dagger a_i), \qquad (66)$$

where i labels the ions along the chain ($i = 1, \ldots, N$) and a_i is the boson annihilation operator of a quantum of transverse vibration at site i. In this representation an excitation hops between sites with a nonlocal hopping amplitude t_{ij}. The frequency of the local oscillators is the transverse trap frequency ω_x, here along the x direction. It includes a position-dependent frequency shift owing to the Coulomb interactions: $\omega_{x,i} = \omega_x - \sum_{i\neq j} t_{ij}$. In the experiment the hopping element between the leftmost ion and its neighbor is in the interval range $t_{ij} \in 2\pi \times (2.21, 6.7)$ kHz, where the smallest (largest) value is for a chain of five ions (25 ions). The measurements show that the time required for the excitation to propagate across the entire chain is comparable to the inverse of the coupling rate between nearest neighbors. This behavior was interpreted as a manifestation of the long-range hopping,

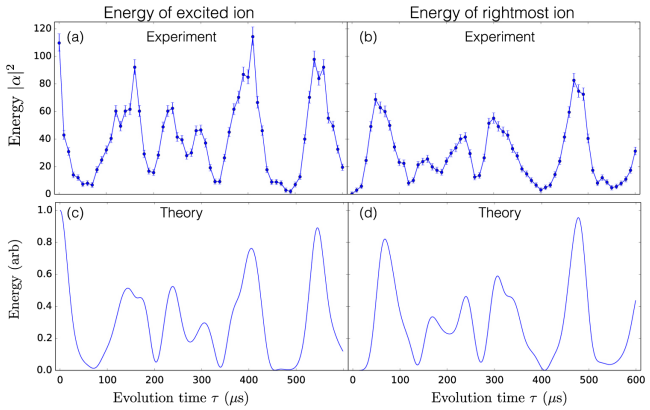

FIG. 42. Energy transport in a chain of five ions. (a) Leftmost ion given a kick and its energy measured after a subsequent evolution time τ. Energy revivals approaching the initial energy are observed. (b) Energy of the rightmost ion. Initially unexcited, the energy from the kick is rapidly transferred across the chain. (c),(d) Energies of ions obtained from molecular dynamics simulations. From Ramm, Pruttivarasin, and Häffner, 2014.

which permits the excitation to directly reach a distant ion. In this configuration long-range hopping favors direct transfer between the edge ions since they possess the same local frequency. These features also explain why adjacent ions could have far different energy excitations.

Revivals of the excitation energy are depicted in Fig. 42. They were reported even for long chains. The revivals persisted for times on the order of 40 ms with measured timescales that seem to be weakly dependent on the number of ions. Their decay was attributed to the change of the radial trap frequency over this time. These revivals can be understood as being due to the rephasing of multiple phonon normal modes and signal the coherent dynamics of the propagating excitation, showing that the chain had not thermalized. In these settings Abdelrahman *et al.* (2017) measured the spreading and refocusing of a vibrational excitation on a chain composed of 42 ions, by means of a Ramsey-type measurement such as that used by De Chiara *et al.* (2008). Abdelrahman *et al.* accessed the autocorrelation functions of the phonons, as well as the quantum discord. The experiments described thus far were performed with cold yet thermal chains. Deep in the quantum regime, transport of a single quantum of vibration was first realized by Tamura, Mukaiyama, and Toyoda (2020) on a chain composed of four $^{40}Ca^{+}$. The experiment reported a coherence time exceeding 10 ms. The experimental measurements were in excellent agreement with the predictions of Eq. (66).

Heat transport in ion chains has been the subject of several theoretical studies. Lin and Duan (2011) determined the energy distribution along the chain when two ions in the chain realized point contacts to heat baths at different temperatures. This configuration can be implemented by continuously laser cooling the two individual ions to different stationary temperatures. A rich behavior was predicted as a function of the cooling rate and of the position of the laser-cooled ions within the chain. Heat transport through an ion chain that undergoes the linear-to-zigzag transition was experimentally measured by Ramm, Pruttivarasin, and Häffner (2014). A theoretical study reported that the onset of zigzag order gives rise to a qualitative change in transport, from ballistic to diffusive (Ruiz *et al.*, 2014). The origin of the diffusive behavior was attributed to the nonlinearity induced by coupling between the longitudinal and transverse phonons to the zigzag modes. Moreover, the heat conductivity was found to be maximal near the critical point, where the transverse phonon spectrum becomes gapless. Transport in a chain embedding two mass impurity defects was theoretically analyzed by Fogarty *et al.* (2013) and Taketani *et al.* (2014). They argued that for certain mass ratios, the motion of the mass defects can become entangled via the resonant exchange of vibrational excitations with the rest of the chain. Heat transport in the presence of a topological defect was investigated by Timm *et al.* (2023) and is reviewed in Sec. III.C. The properties of transport using the radial modes of a linear chain are at the basis of proposals for quantum information with trapped-ion chains (Serafini, Retzker, and Plenio, 2009).

In microtraps, where the ion structure is designed using the external potential, transport experiments have realized the coherent exchange of phononic excitations (Brown *et al.*, 2011; Harlander *et al.*, 2011; Hakelberg *et al.*, 2019). This experimental progress demonstrates the capability of controlling and tailoring phonon hopping between the ions and sets the basis for simulating many-body dynamics of strongly correlated bosons (Porras and Cirac, 2004), as well as for revealing quantum features of transport (Bermudez, Bruderer, and Plenio, 2013). Further work has been devoted to transport controlled by the coupling with the internal degrees of freedom of the ions. We mention here the realization of vibrationally assisted transfer of energy (Gorman *et al.*, 2018) and the simulation of an effective Jaynes-Cummings type of dynamics (Schneider, Porras, and Schaetz, 2012) in order to achieve effects such as phonon-blockade and designed phonon-phonon interactions (Debnath *et al.*, 2018; Ohira *et al.*, 2021).

C. Topological defects and metastability

As mentioned in Sec. II.C.2, manifestations of pretherm-alization in ion Coulomb crystals such as defects and dislocations can be imaged on a CCD camera. They are typically created by means of temporal transformations of the trap potential, or by rapidly quenching the temperature while laser cooling the ion cloud to a crystal. In low-dimensional crystals, and especially in the zigzag chain, it is possible to experimentally monitor the formation and the dynamics of individual defects. This has led to a series of insightful studies, some of which are reviewed in the rest of this section.

Figure 43 reports some examples of defects (kinks) measured in a zigzag chain: Fig. 43(a) displays a so-called localized kink, while Fig. 43(b) shows an example of an extended kink, within which the ions form two parallel ion chains. Other kinds of kinks are composed of dislocations in all three dimensions (Mielenz *et al.*, 2013; Nigmatullin *et al.*, 2016). Mielenz *et al.* (2013) observed the formation of kinks by laser cooling a cloud of $^{24}Mg^{+}$ ions in a linear Paul trap into a zigzag configuration. By imaging the ion positions, they measured kinks at the center of the zigzag chain with an

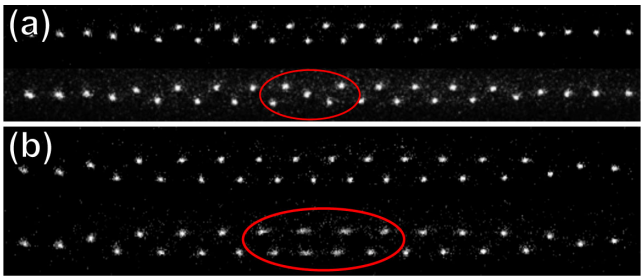

FIG. 43. Experimentally observed kinks in an ion chain of about 30 ions. The kinks (red ellipses) are created during a radial quench of a crystal and imaged with exposure times of 40 ms. (a) Uniform zigzag and localized kink for trap aspect ratio $\nu/\nu_t \approx 8$. (b) Zigzag and extended kink for $\nu/\nu_t \approx 5.5$. Adapted from Partner *et al.*, 2013.

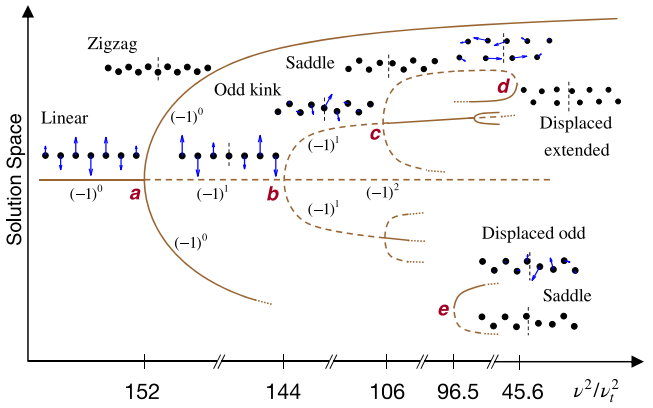

FIG. 44. Schematic of bifurcations and stability of one-kink configurations in a planar crystal of 31 ions. The possible ion configurations are depicted as a function of the ratio of confinement in the axial and one of the transverse directions, where confinement in the second transverse direction is assumed to be strong. The solid lines indicate stable configurations (local minima of the potential); the dashed lines are unstable solutions. The arrows illustrate the spatial oscillations of the normal mode that crosses zero energy at the bifurcation and generates the bifurcating solutions. From Landa *et al.*, 2013.

occurrence rate that depended on the number of ions. The kinks decayed by propagating from the center to the edges of the zigzag chain on a timescale on the order of 10 s, exceeding the oscillation period of the axial trap by 5 orders of magnitude.

Defects such as those shown in Fig. 43 were also observed in experiments where the trap aspect ratio was slowly varied across the linear-zigzag transition while the chain was continuously laser cooled (Ejtemaee and Haljan, 2013; Partner *et al.*, 2013; Pyka *et al.*, 2013; Ulm *et al.*, 2013). They were reproduced by molecular dynamics simulations in the pseudopotential approximation, showing that micromotion is not essential in determining their onset and metastability; see Sec. II.C.2 for a comparison. Their metastable nature identifies them as topological defects. Note that distant localized kinks interact, as verified by a comparison of experimental data and molecular dynamics simulations (Landa *et al.*, 2013).

A classification of kinks was carried out by Landa *et al.* (2013), who used tools of topological degree theory. The stability of a given defect is determined by an analysis of the eigenvalues of the corresponding Hessian matrix; a bifurcation occurs every time an eigenvalue of the Hessian changes sign. Figure 44 illustrates the resulting metastable and unstable equilibrium configurations of one planar kink as a function of the trap aspect ratio for a fixed number of ions (Landa *et al.*, 2013).

The dynamics of a kink is characterized by localized modes, which include a translational mode as well as internal modes. A theoretical analysis of the internal modes of both localized and extended kinks predicted well-resolved spectroscopic features and long coherence times, even at Doppler-cooling temperatures (Landa *et al.*, 2010). The translational energy of the topological defects was studied by calculating the Peierls-Nabarro potential, namely, the potential energy of the soliton as a function of the kink center position (Landa *et al.*, 2013; Partner *et al.*, 2013). Numerical simulations of energy transport in ion chains with a topological defect reported energy localization at the kink (Timm *et al.*, 2020).

The spectroscopic features of the localized defects were measured by Brox *et al.* (2017) by parametric heating. Experimental observations show features that suggest directed transport as a function of the topological charge (Brox *et al.*, 2017). The stability of the extended kink as a function of the trap ratio and its dynamics was extensively analyzed by Kiethe *et al.* (2018); see Sec. III.E.

The prospect of controlling the formation and dynamics of topological defects in ion chains has inspired several theoretical proposals. Landa *et al.* (2014) argued that discrete solitons in a chain confined to a ring geometry can generate entanglement between ions. In a linear Paul trap, when the edge ions are heat point contacts at two different temperatures, the presence of a kink can substantially modify the heat flow, giving rise to a pronounced temperature gradient at its location (Timm *et al.*, 2021). Together, these insights suggest that the interactions between kinks and normal modes of the chain can modify and even tailor the transport properties; see also Sec. III.E.

Mass impurities embedded in the chain give rise to an additional class of topological defects (Landa *et al.*, 2013). It has been argued that the combination of mass impurities and static electric fields can allow for deterministic manipulation and creation of kinks (Landa *et al.*, 2013). Theoretical studies further predict that interactions between mass impurities and the surrounding chain can generate entanglement between the localized modes associated with these defects (Fogarty *et al.*, 2013). Chains containing mass or charge impurities are routinely realized in ion-trap laboratories (Feldker *et al.*, 2014; Keller *et al.*, 2024; Hausser *et al.*, 2025). Structural phase transitions in the presence of mass impurities were characterized by Rüffert *et al.* (2024). Dual species ion crystals can be deterministically prepared (Zawierucha *et al.*, 2024). By positioning impurities at selected locations within the chain, the dispersion spectrum can be designed (Sosnova, Carter, and Monroe, 2021), with applications in quantum logic (Morigi and Walther, 2001; Home, 2013) and metrology (Schmidt *et al.*, 2005; Home, 2013).

We conclude by mentioning structural defects realized by combining spin-dependent forces and individual ion excitations in ion Coulomb crystals (De Chiara *et al.*, 2008; Baltrusch, Cormick *et al.*, 2011; Li and Lesanovsky, 2012; Feldker *et al.*, 2014; Mallweger *et al.*, 2025). Such dynamics can give rise to entanglement between vibrational and internal degrees of freedom (De Chiara *et al.*, 2008; Baltrusch, Cormick *et al.*, 2011; Gilmore *et al.*, 2021) and are employed for quantum technological applications (Gilmore *et al.*, 2021; Martins *et al.*, 2026).

D. Slow quenches and the Kibble-Zurek mechanism

Experimental imaging of kinks in ion Coulomb chains enables a statistical analysis of their formation as a function of the experimental parameters (Ejtemaee and Haljan, 2013; Mielenz *et al.*, 2013; Partner *et al.*, 2013; Pyka *et al.*, 2013; Ulm *et al.*, 2013). On this basis De Chiara *et al.* (2010) and del Campo *et al.* (2010) argued that one can test the so-called Kibble-Zurek (KZ) hypothesis by performing slow ramps across the linear-zigzag structural transition.

The KZ hypothesis was formulated in an attempt to describe inhomogeneities at the cosmological scale as defects formed during the slow expansion of the Universe (Kibble, 1980) and then proposed as a paradigm for adiabatic expansion across a continuous, symmetry-breaking phase transition (Zurek, 1985). It predicts the scaling of the excess heat produced by a slow ramp of a control field across a second-order phase transition, thereby connecting the equilibrium critical exponents with features of the out-of-equilibrium dynamics.

In the experiments the statistics of defect formation was measured after slowly ramping the trap aspect ratio across the symmetry-breaking linear-zigzag transition (Ejtemaee and Haljan, 2013; Pyka *et al.*, 2013; Ulm *et al.*, 2013). The behavior of the excess heat as a function of the ramp velocity appeared to follow power-law behavior (Ejtemaee and Haljan, 2013; Pyka *et al.*, 2013; Ulm *et al.*, 2013), which is compatible with the KZ hypothesis. In this section we review the theoretical model and the experimental results.

De Chiara *et al.* (2010) modeled the dynamics of defect formation starting with the Landau model of Sec. II.A.4 for the transverse displacement field ψ and included the dissipative dynamics of laser cooling by means of a damping and a Langevin force; see Puebla *et al.* (2017) for a discussion of a related semiclassical model. For a chain aligned along the x axis, assuming that the motion along z is frozen out, the displacement field is along the y direction and its dynamics is governed by

$$\frac{\partial^2}{\partial t^2}\psi - v(x)^2\frac{\partial^2}{\partial x^2}\psi + \delta(x,t)\psi + 2\mathcal{A}(x)\psi^3 = -\eta\partial_t\psi + \varepsilon(t). \tag{67}$$

On the right-hand side of Eq. (67), η is the damping rate and $\varepsilon(t)$ is the Langevin force [recall that $\langle\varepsilon(t)\rangle = 0$ and $\langle\varepsilon(t)\varepsilon(t')\rangle = (2\eta k_B T/m)\delta(t-t')$, where T is the stationary temperature of Doppler cooling (Stenholm, 1986; Morigi and Eschner, 2001)]. The equation of motion on the left-hand side of Eq. (67) was obtained by taking the continuous limit of Eq. (45), with V_0 given by Eq. (43). The first two terms of Eq. (67) describe a wavelike propagation with velocity $v(x)$ that is position dependent when the chain's charge distribution is inhomogeneous; see Eq. (38). The parameter $\delta(x,t) \approx \nu_t(t)^2 - \nu_t^{(c)}(x)^2$ gives the amplitude of the local force in the harmonic approximation, where $\nu_t^{(c)}(x)$ is a position-dependent critical trap frequency at which the chain becomes locally unstable.[4] The term $2\mathcal{A}\psi^3$ is the force in the next order; see Eq. (43).

Let the transverse trap frequency be ramped from above to below the critical point with rate $1/\tau_Q$ such that $\delta(t) = -\delta_0 t/\tau_Q$, with δ_0 a constant while the time is varied in the interval $t \in [-t_0, t_0]$. At $t = -t_0$ the linear chain is the stable equilibrium configuration of Eq. (67), while at $t = t_0$ the stationary configuration is the zigzag. According to the KZ hypothesis, the linear and zigzag ground states can be connected by an adiabatic transformation when τ_Q is much larger than the relaxation timescale τ_R of the time-independent problem. In this case, the chain will be able to instantaneously adapt to the temporal variation of $\delta(t)$, implying that τ_R depends on the instantaneous value of $\delta(t)$, $\tau_R = \tau_R[\delta(t)]$. However, close to the critical point, τ_R diverges and the adiabatic condition $\tau_Q \gg \tau_R$ becomes invalid. The KZ mechanism identifies the so-called freeze-out time $\hat{t}$, at which $\hat{\delta} = \delta(\hat{t})$ such that $\tau_Q = \tau_R(\hat{\delta})$. At the freeze-out timescale, the KZ theory postulates that the dynamics becomes frozen out until after the ramp has crossed the critical region. Effectively, it is as if δ were suddenly quenched from $\hat{\delta}$ to $-\hat{\delta}$. According to this conjecture, domains formed in the linear phase at $\hat{\delta}$ then become topological defects in the symmetry-broken phase. This simple hypothesis permits one to determine the scaling of the density of defects d with the ramp time since d is inversely proportional to the size $\xi(\hat{\delta})$ of the domains.

In the homogeneous case, the coefficients of Eq. (67) are independent of x and the critical value is independent of the position along the chain. Close to the critical point, $\tau_R \sim \delta^{-\nu z}$, where $\nu = 1/2$ is the mean-field exponent of the correlation length ξ and z is the dynamical critical exponent. The scaling of defects is determined by the size of the domain walls at the freeze-out time, with $d \sim 1/\xi(\hat{\delta})$ and $\xi(\hat{\delta}) \sim |\hat{\delta}|^{-\nu}$, giving $d \sim \tau_Q^{-\alpha}$ with $\alpha = \nu/(1+z\nu)$. Depending on whether the dynamics is overdamped ($\eta \gg \sqrt{\hat{\delta}}$, corresponding to $z = 2$) or underdamped ($\eta \ll \sqrt{\hat{\delta}}$, corresponding to $z = 1$), then $\alpha = 1/4$ or $\alpha = 1/3$, respectively (De Chiara *et al.*, 2010).

In a linear Paul trap, the ion density along x is nonuniform. For long chains there is a propagating front, from the center to the edges, with which $\nu_t(x)$ crosses the local critical value. This front tends to give rise to independent spatial regions where the transition occurs, and thus to defect nucleation. The speed of the propagating front should be compared with the

[4]For a chain in a linear Paul trap, at the center the functional $\nu_t^{(c)}(x)$ attains its maximum and takes the value $\nu_t^{(c)}(0) = \nu_t^{(c)}$ (see Sec. II.A.4) while it decreases with the distance $|x|$ from the chain's center.

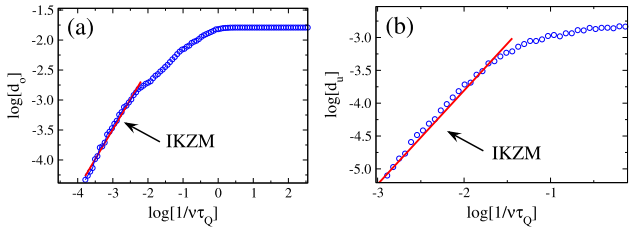

FIG. 45. Density of defects d for an ion chain in a linear trap as a function of the inverse of the sweeping rate (a) in the overdamped regime and (b) in the underdamped regime. The circles are obtained from a molecular dynamics simulation with 50 ions in a linear Paul trap; the defects are counted in only the central 30 ions. The solid red line is the fitting function $d \sim \tau_Q^{-\alpha}$ giving (a) $\alpha = 0.995$ and (b) $\alpha = 1.427$. Both results are consistent with the predictions of the inhomogeneous KZ mechanism. The curves saturate mostly because of finite-size effects. From del Campo *et al.*, 2010.

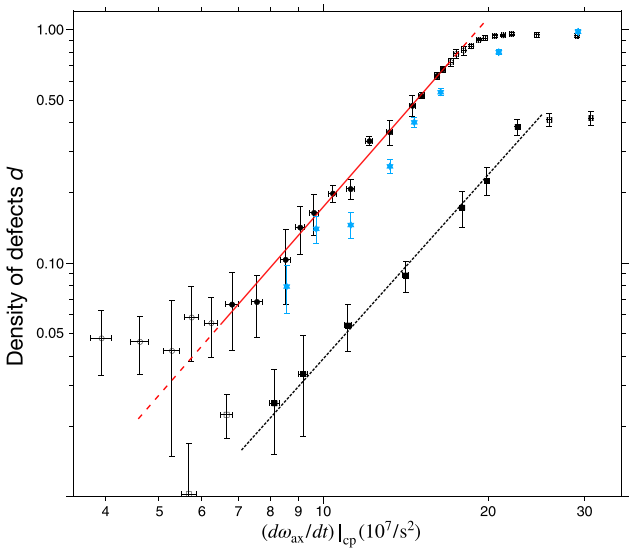

FIG. 46. Defect formation rates in a chain of 16 $^{40}Ca^{+}$ ions gathered by changing the axial trap frequency across the linear-zigzag transition. Shown is a double-logarithmic plot of the measured density of defects d vs the rate of change of ω_{ax} at the critical point, where ω_{ax} is the trap confinement frequency along the direction of the ion chain. All circles correspond to 60 000 measurements at a radial trap anisotropy of 1.03. The fitted function of the form $d \propto 1/\tau_Q^{\alpha}$ (solid red line) gives an exponent $\alpha = 2.68 \pm 0.06$. The constant offset visible at lower ramping rates stems from background gas collisions. The saturation is due to the maximum number of defects being limited by the system size. For comparison, the rate of defects measured with a higher radial trap anisotropy of 1.05 is plotted (squares), showing a loss of defects but a similar fitted exponent of $\alpha = 2.62 \pm 0.15$ (dotted line). Solid data points are used for the fits. The blue stars depict the result of molecular dynamics simulations. Adapted from Ulm *et al.*, 2013.

velocity $v(x)$, at which a perturbation propagates from the center to the edges of the chain, thereby causally connecting the chain. Both quantities depend on the local density, but with different functional behaviors. This leads to different scaling exponents, namely, $\alpha = 1$ for the overdamped regime and $\alpha = 4/3$ for the underdamped dynamics (De Chiara *et al.*, 2010; del Campo *et al.*, 2010). These scalings have been confirmed by molecular dynamics simulations, as shown in Fig. 45.

Experimentally, the slow quench was performed in three different platforms, with different ion numbers and species. The trap aspect ratio was varied across the linear-zigzag transition by sweeping the transverse frequency (Pyka *et al.*, 2013), the axial frequency (Ulm *et al.*, 2013), or both simultaneously (Ejtemaee and Haljan, 2013). In all experiments the ions were initially cooled to the Doppler limit and the cooling laser was on during the entire duration of the quench. The density of defects was measured after the quench using a CCD camera per sweep and averaging over several sweeps, yielding consistent results. Figure 46 shows the resulting statistics of kinks (Ulm *et al.*, 2013). The solid and dashed lines show the function $d \sim \tau_Q^{-8/3}$, which fits the interval in which the sweep rate exceeds the rate of background collisions but is still sufficiently small that defect generation does not saturate. This scaling is compatible with the measurements reported by Ejtemaee and Haljan (2013) and was also reported in the defect statistics measured by Pyka *et al.* (2013) on a larger parameter interval. Molecular dynamics simulations accounting for the experimental setup reproduced the results of De Chiara *et al.* (2010) and del Campo *et al.* (2010) for ramps other than the experimental ones and reported the exponent $\alpha = 8/3$ for the experimental regime (Ejtemaee and Haljan, 2013; Pyka *et al.*, 2013). This power-law scaling has been attributed to a type of KZ mechanism even though a theoretical model justifying this scaling has not been yet identified; see del Campo, Kibble, and Zurek (2013).

The agreement between experiments and molecular dynamics simulations shows that the observed scalings emerge from classical dynamics. Indeed, the experiments are performed with laser-cooled ions at Doppler temperatures at which quantum effects are not expected to be visible; see Sec. II.A and Shimshoni, Morigi, and Fishman (2011a). Quantum effects could be measured for slower quenches and purely coherent dynamics. In this case it should be possible to observe the scaling of defects determined by the critical exponents of the Ising model (Silvi *et al.*, 2013), namely, the quantum KZ mechanism. Silvi *et al.* (2016) used a DMRG simulation to determine the defect statistics generated by slow quenches across the quantum critical model of Sec. II.A.5. A crossover from classical to quantum KZ scaling was reported as a function of the quench rate, with the requirements identified on the ramp speed in order to unveil quantum effects on defect formation.

E. Stick-slip motion and nanofriction

The possibility of imaging the ions within a Coulomb crystal and controlling the forces at play makes these systems ideal platforms for investigating static friction (Vanossi *et al.*, 2013). Static friction refers to the finite work needed to put in motion an object in contact with a surface. It is associated with dynamical phenomena such as stick-slip motion, which consists of intermittent sliding and stuck phases and can characterize the motion of a mesoscopic object dragged over a

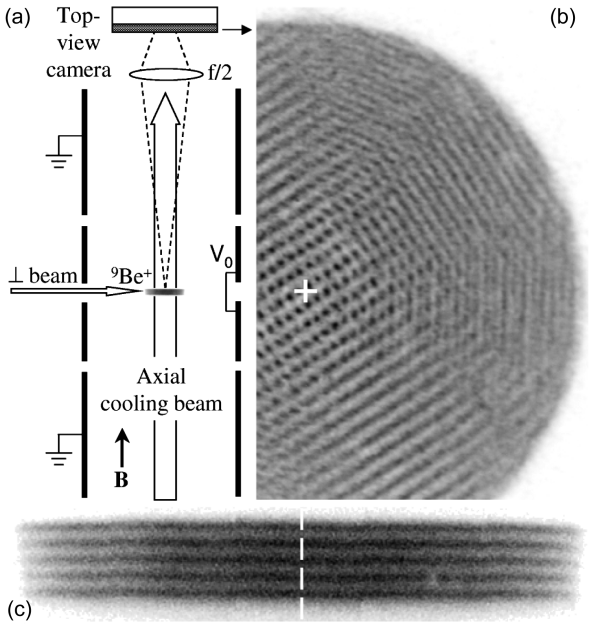

FIG. 47. Setup used to study stick-slip motion on a Coulomb crystal. (a) Schematic of the cylindrical Penning trap and the top-view imaging system. (b) Strobed top-view image of a five-axial plane $^9Be^+$ ion crystal with a bcc structure. (c) Side-view image (unstrobed) of the same ion crystal. A rotating electric field creates a torque on the crystal. From Mitchell *et al.*, 2001.

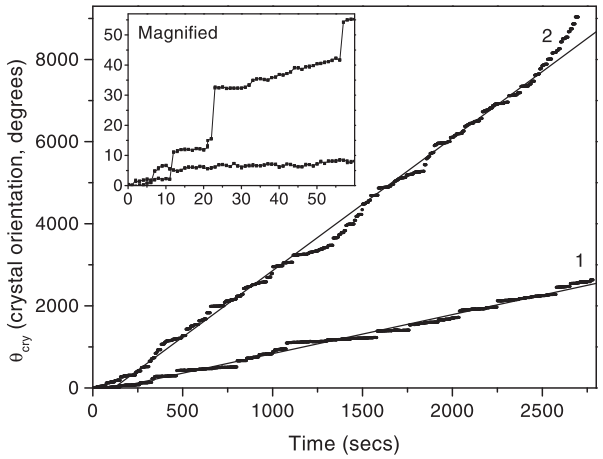

FIG. 48. Crystal orientation in the frame of a rotating perturbation for measurements with two different perpendicular beam torques. The torque is greater in measurement 2. The lines are from a linear regression fit. Inset: magnified plot of the first 60 s of data. From Mitchell *et al.*, 2001.

surface. Stick-slip motion has been observed in laser-cooled ion crystals rotating in Penning traps in the setup shown in Fig. 47. Stress was created by two opposing torques generated by a rotating electric field that controls the ion-crystal rotation through forces applied to the crystal boundary and radiation pressure forces from a focused laser beam, thus implementing Doppler cooling (Mitchell *et al.*, 2001). Stick-slip dynamics was manifested in sudden angular jumps ("slips") of the crystal orientation alternating with intervals when the crystal orientation was phase locked ("stuck") relative to the rotating wall perturbation, as seen in Fig. 48. Note that the slip amplitudes were shown to exhibit a power-law distribution reminiscent of self-organized critical phenomena (Mitchell *et al.*, 2001).

Ion chains offer a controlled environment for studying static friction. Pinning at the subwavelength scale can be observed using resonance fluorescence and has been measured in small ion clusters confined by optical lattices (Enderlein *et al.*, 2012; Linnet *et al.*, 2012; Bylinskii *et al.*, 2016; Lauprêtre *et al.*, 2019; Gangloff, Bylinskii, and Vuletić, 2020). Figure 49 shows the resonance fluorescence of trapped ions as a function of lattice depth for various geometries, allowing the identification of the ions' positions within the lattice. The dragging of an object over a surface can be implemented by setting the chain in motion relative to the optical lattice, as illustrated in Fig. 50. The stick-slip motion results in bistability in the potential energy and manifests itself as hysteresis in the ion position. Bylinskii, Gangloff, and Vuletić (2015) and Gangloff *et al.* (2015) the maximal friction force was extracted from measurements of the hysteresis of the ion position.

A further advantage of studying nanofriction with ion chains is that these platforms are amenable to microscopic modeling and mapping to paradigmatic models (Garcia-Mata, Zhirov, and Shepelyansky, 2007; Benassi, Vanossi, and Tosatti, 2011; Pruttivarasin *et al.*, 2011; Cormick and Morigi, 2013; Vanossi *et al.*, 2013). In the presence of an optical lattice, when the ion chain can be described as an elastic crystal, the dynamics is captured by a paradigmatic model of static friction, the so-called Frenkel-Kontorova (FK) model (Braun and Kivshar, 2004; Pruttivarasin *et al.*, 2011; Cormick and Morigi, 2013),

$$V_{\mathrm{FK}} = \frac{1}{2}\sum_{i,j}\mathcal{K}_{ij}(q_i - q_j)^2 + \frac{U}{2}\sum_j [1-\cos(2\pi x_j/a)], \quad (68)$$

where the second term is the optical lattice with depth U and period a and $q_j = x_j - x_j^{(0)}$ is the axial displacement of ions with respect to the equilibrium position $x_j^{(0)}$ at $U = 0$. The harmonic crystal approximation is valid when the average distance between ions d_0 satisfies $d_0 \gg a$ and the Coulomb force varies smoothly over a. This is typically fulfilled in ion chains where $d_0 \gtrsim 5$ μm and is thus at least 1 order of magnitude larger than the optical lattice periodicity a.

For uniform chains and nearest-neighbor couplings, when $x_j^{(0)} = jd_0$ and $\mathcal{K}_{ij} = K_0\delta_{j,i+1}$, the ground-state and dynamical properties of the FK model are fully determined by two dimensionless parameters, the ratio U/K_0 between the substrate potential and the elastic force and the ratio d_0/a between the two characteristic length scales. At fixed, incommensurable values of the ratio d_0/a, the critical value $[U/K_0]_c$ signals the Aubry transition, separating the sliding phase, where forces giving rise to sticking cancel, from the pinned phase, where the motion alternates stick and slip phases and the minimal force needed to initiate sliding is finite (Braun and Kivshar, 2004). In the pinned phase, continuous translational invariance is broken and pinning is signaled by a nonzero frequency of the lowest phonon mode. At a fixed lattice depth, a given commensurate (periodic) phase at a commensurable ratio d_0/a remains stable for small variations $d/a = d_0/a \pm \delta$, where the mismatch δ

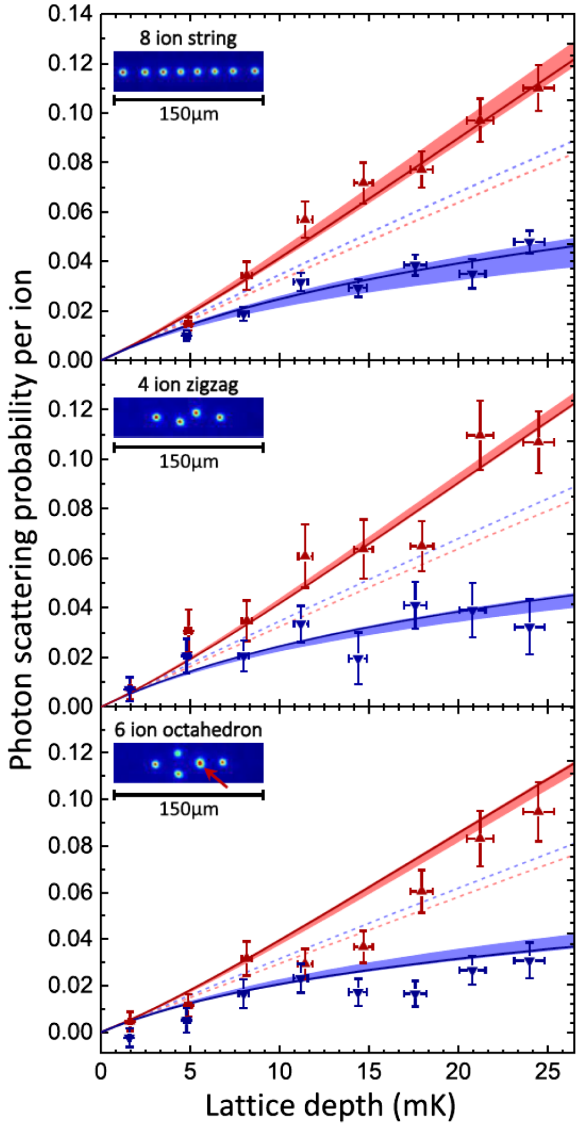

FIG. 49. Probability of scattering a photon from a one-dimensional optical lattice as a function of the optical lattice depth for small one-dimensional (top panel), two-dimensional (center panel), and three-dimensional (bottom panel) Coulomb crystals. The red (upward-pointing) and blue (downward-pointing) triangles are experimental data points for red- and blue-detuned lattices, respectively. As expected for pinned ions, the scattering probability is higher for pinning at intensity maxima (red detuning) than at intensity minima (blue detuning). For comparison, the dashed red (lower) and blue (upper) lines show the theoretical scattering probabilities expected for delocalized ions. From Lauprêtre *et al.*, 2019, who included a discussion of the error bars and uncertainties.

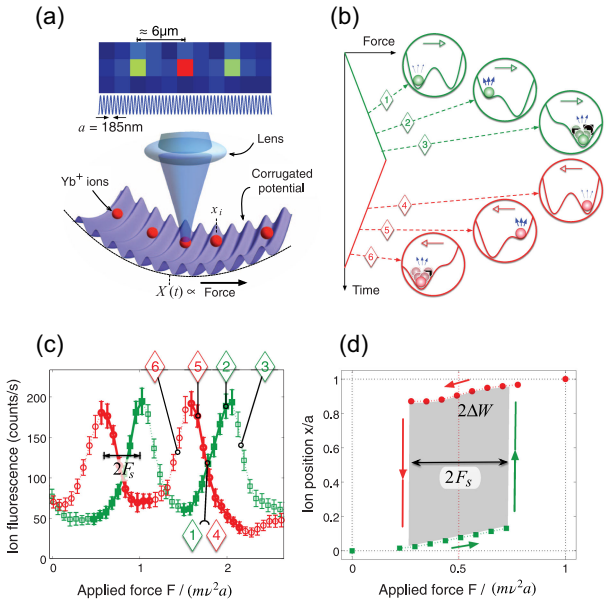

FIG. 50. Ion-crystal emulator of stick-slip friction. (a) Coulomb crystal of $^{174}Yb^{+}$ ions subjected to an optical lattice potential. The ions are imaged with a single-ion-resolving microscope. The typical ion spacing is 6 μm, and the lattice period is $a = 185$ nm. In the bottom illustration of the corrugated potential, the lattice period and the corrugation are strongly exaggerated. (b) Stick-slip results from bistability, illustrated here for a single ion. A shear force is linearly ramped, causing the ion to jump between minima. The stages of the stick-slip process are labeled with numbered diamonds and illustrate the dynamics of the ion during the ramp. The ion's position is extracted from its fluorescence, which is proportional to the lattice potential energy. (c) Fluorescence vs applied force during the forward transport (green squares) and reverse transport (red circles), showing hysteresis that is used to measure the maximum static friction force F_s. The bold data points indicate the ion's position before a slip, and only those data are used to reconstruct the force-displacement curve. (d) Force-displacement hysteresis loop enclosing an area equal to twice the dissipated energy per slip ΔW. The unit $m\nu^2 a$ of the applied force corresponds to 2.8×10^{-19} N; $\nu = 2\pi \times 364$ kHz. Adapted from Bylinskii, Gangloff, and Vuletić, 2015.

quantifies the deviation from the commensurable ratio. The system undergoes a discontinuous transition to an incommensurate (sliding) phase at a critical value $\delta_c > 0$ where the formation of solitons is energetically favorable and the phase becomes a sliding one.

Implementing these dynamics with ions requires one to take into account the long-range Coulomb interactions. Moreover, the external potential of a linear Paul trap breaks the translational invariance, and the lattice-free interparticle distance $d_{j,j+1} = x_{j+1}^{(0)} - x_j^{(0)}$ is inhomogeneous but symmetric under reflections about the trap center. For small ion chains having two to five ions, the long-range interactions do not significantly modify the dynamics with respect to the short-range model. The commensurate phase is realized by adjusting the Paul trap harmonic potential, tuning the misfit to $p_0 = 0$, where the misfit is defined as (Gangloff, Bylinskii, and Vuletić, 2020)

$$p_0 = \frac{2}{N-1}\sum_{j=1}^{N-1}(d_{j,j+1}/a) \bmod 1. \tag{69}$$

In these settings changing p_0 is equivalent to tuning the mismatch δ. Figure 51 displays measurements on small chains for different misfits p_0 across the commensurate-incommensurate transition (Gangloff, Bylinskii, and Vuletić, 2020). The gray regions in Fig. 51 correspond to the commensurate phase,

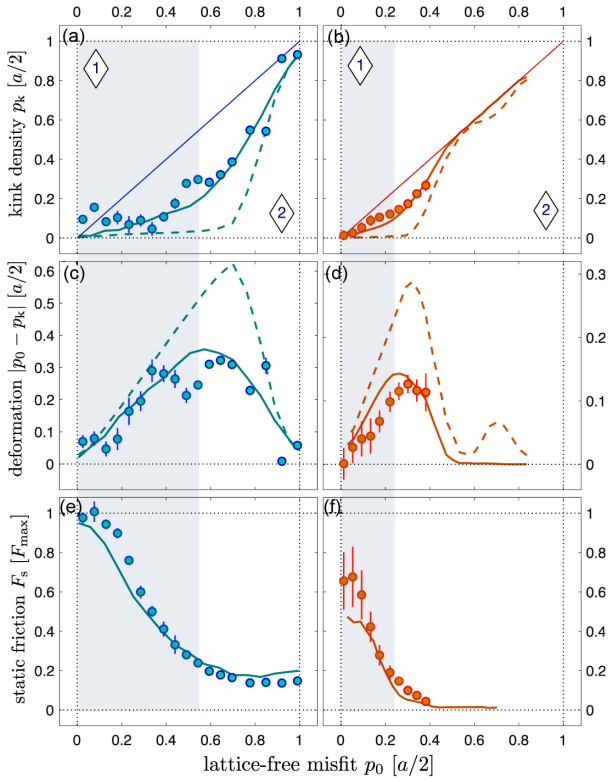

FIG. 51. Commensurate-incommensurate phase transition in an extension of the setup of Bylinskii *et al.* (2016) for two ions (left panels) and five ions (right panels). Shown are the measured kink density p_k (top panels), deformation $|p_0 - p_k|$ (middle panels), and static friction force F_s (bottom panels) vs the misfit p_0. The lines in (a) and (b) are the kink density $p_k = p_0$ for $U = 0$. The solid curves in (a)–(f) are numerical simulations for parameters matching those of the data shown using (a),(c),(e) $k_B T/U = 0.2$ and (b),(d),(f) $k_B T/U = 0.5$. The dashed curves are $T = 0$ simulations. F_{max} is the maximal friction in the single-slip regime. From Gangloff, Bylinskii, and Vuletić, 2020.

where the formation of kinks is suppressed at zero temperature, while in the white regions the friction force is minimal. The discrepancy of the experimental data from the zero-temperature simulation is attributed to thermal effects. This hypothesis is supported by a comparison with molecular dynamics calculations that assume a finite temperature. Note that in the Paul trap, the friction force does not vanish in the sliding phase but becomes independent of the misfit p_0 or of the lattice depth U. In this environment the sliding-pinning Aubry transition breaks the reflection symmetry about the trap center (Braiman *et al.*, 1990; Benassi, Vanossi, and Tosatti, 2011; Fogarty *et al.*, 2015).

The Aubry transition was observed in the setup of Fig. 50 through measurement of the static friction force as a function of optical lattice depth (Bylinskii *et al.*, 2016). It was also reported in a setup that simulated the FK model in a chain of about 30 ions in the absence of a periodic lattice (Kiethe *et al.*, 2017). In the realization of Kiethe *et al.* (2017), in fact, the elastic crystal and the substrate are the upper and lower chains of an extended kink, which is metastable in the zigzag phase for a finite range of aspect ratios; see Fig. 52(a). In this setup a cooling laser induces differential forces between the upper and lower chains and can thus set one into motion with respect to the other (Kiethe *et al.*, 2017, 2018). The parallel chains forming the extended kink can slide on top of one another. By decreasing the transverse trap frequency, the extended kink becomes unstable and the stable structure is a zigzag corresponding to locking one chain with respect to the other and realizing a pinned phase. The symmetry breaking is revealed by measuring the relative axial distance Φ between the ions of the different layers as a function of the trap aspect ratio. The results of the measurement are shown in Fig. 52(b). Figure 52(c) reports the measurement of the frequency of the lowest vibrational mode, which is detected by a second laser performing vibrational spectroscopy. The smoothing of the transition is attributed to thermal fluctuations and is reproduced by both molecular dynamics simulations and a microscopic model that incorporates thermal effects (Kiethe *et al.*, 2021).

Despite the analogy with the FK model, the two chains in Fig. 52 mutually interact. Hence, proper modeling of their dynamics must take into account the backaction of the elastic crystal on the surface to which it is dragged. This is indeed closer to the typical scenario of nanofriction, where the substrate is deformable, than the idealized FK model. Another implementation of deformable substrates is realized when the ion chains interact with the standing-wave field of an optical cavity (Guthöhrlein *et al.*, 2001; Keller *et al.*, 2004; Linnet *et al.*, 2012; Cetina *et al.*, 2013; Casabone *et al.*, 2015). For sufficiently large couplings, the cavity optical lattice depth depends nonlinearly on the ion density, such that it is constant in the sliding phase and can become steeper (or shallower, depending on the experimental parameters) in the pinned phase (Cormick and Morigi, 2012, 2013; Fogarty *et al.*, 2015). For this setup the sliding and pinned phases are separated by bistable regions where superlubric and stick-slip dynamics coexist (Fogarty *et al.*, 2015). Moreover, photon scattering into the cavity mode can cool the chain vibrations even down to the zero-point motion (Fogarty *et al.*, 2016). Entanglement in the pinned phase was theoretically studied by Kahan and Cormick (2024). The phase, temperatures, and correlations can be measured in the spectrum of the intensity at the cavity output (Cormick and Morigi, 2013; Fogarty *et al.*, 2016).

F. Kink dynamics and quantum sliding

Kinks of the FK model are quasiparticles of tunable mass and velocity that can be revealed by resonance fluorescence (Chelpanova *et al.*, 2023). Gangloff, Bylinskii, and Vuletić (2020) created a kink at one end of a five-ion chain. Its dynamics as a function of the misfit p_0 was measured. In the sliding phase, the kink travels through the chain with a velocity that increases with decreasing p_0, while it fades away in the commensurate phase (Gangloff, Bylinskii, and Vuletić, 2020). This behavior is qualitatively reproduced in numerical simulations (Chelpanova *et al.*, 2023, 2024). Semiclassical simulations of sudden quenches from the commensurate into the incommensurate phase indicate that, deep in the quantum regime, the dislocation can tunnel into the chain such that the chain is a transient superposition between a commensurate and an incommensurate (sliding) structure (Chelpanova *et al.*, 2023, 2024).

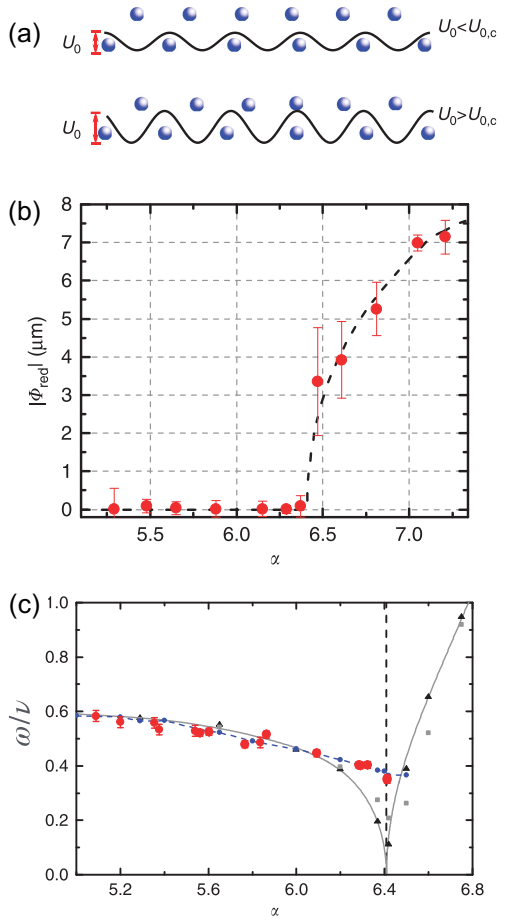

FIG. 52. (a) Illustration of the sliding phase (extended kink; top row) and pinned phase (zigzag chain; bottom row). The Coulomb potential of one row of ions acts as the corrugation potential for the other row. The depth of the corrugation U_0, which is controlled by the trap aspect ratio, determines the dynamics of the system. Below a critical corrugation depth U_{0c}, the system displays horizontal mirror symmetry. Above the critical value, the symmetry is broken. (b) Experiment performed with $^{172}Yb^+$ ions in a linear Paul trap laser cooled at about 1 mK. The absolute value of the order parameter $|\Phi|$, which characterizes the horizontal mirror symmetry, is plotted against the aspect ratio transverse to the axial frequencies, $\alpha = \nu_t/\nu$. In the pinned phase, the symmetry is broken ($|\Phi| > 0$). The experimental data (red circles) are shown in comparison to numerically obtained values for $T = 0$ K (dashed black line). The error bars are 1 standard deviation estimates. (c) Frequency of the soft mode in a 30-ion crystal. The experimental data are shown in red circles, and the error bars are given by uncertainties of the measured soft mode and common mode frequencies. The solid line displays the numerically calculated dispersion relation at $T = 0$ K. Frequencies extracted via a Fourier transformation from the molecular dynamics simulation are given by black triangles at $T = 5$ μK, gray squares at $T = 50$ μK, and blue circles at $T = 1$ mK. The dashed blue line is a guide for the eye. All frequencies are plotted in units of the axial secular frequency $\nu = 2\pi \times (25.6 \pm 0.2)$ kHz. The pinning transition is marked with a vertical line. Adapted from Kiethe *et al.*, 2017.

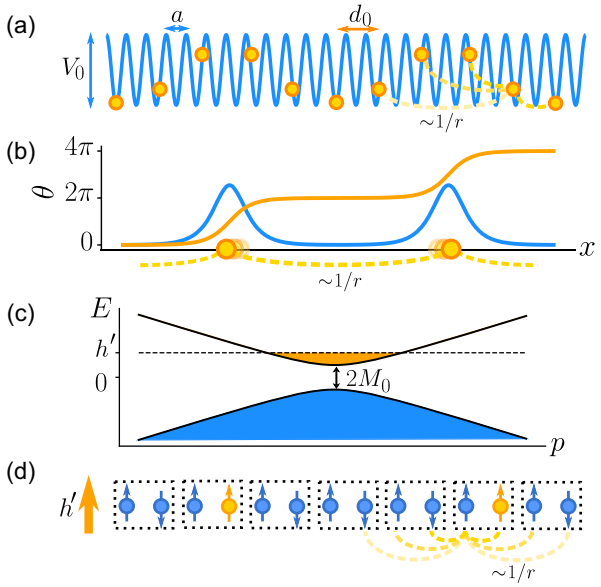

FIG. 53. (a) Schematic of the Wigner crystal in the presence of an externally applied optical lattice mimicking a substrate potential. The substrate potential leads to dislocations of the ions from the crystal's equilibrium position. (b) Dislocations (solitons) displayed as phase shift $\theta(x)$ along the chain axis x (monotonic orange curve). The first-order derivative of $\theta(x)$ (blue curve) exhibits local maxima where the solitons are located. The dashed yellow curves illustrate that the solitons behave as interacting charges. (c) Schematic showing that in the Thirring model, the solitons are positive-energy excitations over a filled Dirac sea where the gap is twice the soliton mass M_0. The phase is commensurate when the chemical potential h' (controlled by the mismatch) falls within the gap. For $h' > M_0$ the solitons proliferate and the phase is incommensurate. (d) Interpretation of the spin-fermion equivalence in the discretized Thirring model corresponding to a long-range interacting XXZ antiferromagnetic spin chain: Solitons are defects (copolarized adjacent spins highlighted in orange) in the staggered ordering of a spin chain. From Menu *et al.*, 2024a.

The experimental level of control suggests that it could be possible to observe quantum dynamics of kinks. This question is at the center of studies in material science of quantum lubrication, where sliding is initiated by quantum tunneling (Krajewski and Müser, 2004; Vanossi *et al.*, 2013). Path integral quantum Monte Carlo simulations identified the regime of parameters where quantum-induced sliding phases could be observed in chains of five ions (Bonetti *et al.*, 2021). Semiclassical analysis discussed the dynamics of tunneling of the kink in the platform of Kiethe *et al.* (2017); see Timm *et al.* (2021, 2023).

A general framework for quantum lubrication in ion chains, developed by Landa, Cormick, and Morigi (2020) and Menu *et al.* (2024a, 2024b), permits one to derive a quantum field theory for the solitons as quasiparticles. These researchers showed that the long-range Coulomb interactions substantially modify the features of the topological kinks with respect to the short-range FK model, favoring soliton formation in long chains (Menu *et al.*, 2024a, 2024b).

Figure 53(a) sketches a chain displaying two kinks. The kink configuration is described by the finite displacement δx_j from the position of the commensurate configuration and can be cast in terms of a phase $\theta_j = 2\pi\delta x_j/a$ such that a change by 2π corresponds to a kink; see Fig. 53(b) and Chelpanova *et al.*

(2024). For long chains and $d_0 \gg a$, the phase θ_j is captured by the field $\theta(x,t)$, which is the solution of the modified sine-Gordon equation (Braun, Kivshar, and Zelenskaya, 1990; Landa, Cormick, and Morigi, 2020),

$$\frac{1}{v_s^2}\partial_t^2\theta = \partial_x^2\theta - M^2\sin\theta + \frac{1}{3}\partial_x\int_1^{N/2}\frac{\partial_x\theta(x+u)+\partial_x\theta(x-u)}{u}\mathrm{d}u, \quad (70)$$

where x is rescaled by a. Equation (70) is parametrized by the velocity $v_s = \sqrt{3K_0/(2m)}$ and the mass term $M = \sqrt{8\pi^2 U/(3K_0 a^2)}$, with $K_0 = 2Q^2/(4\pi\epsilon_0 d_0^3)$. The solutions of Eq. (70) are constrained to satisfy the mismatch $\delta = \min_{n_0\in\mathbb{N}}(d_0 - n_0 a)/a$. In the short-range FK model the integral term vanishes and the solution is a sine-Gordon soliton with sound velocity v_s and a length proportional to d_0/M, while the mass M scales the energy of a kink. The Coulomb interactions give rise to the integral term. As a consequence, the kink's center has the form of a sine-Gordon soliton whose width now scales with the size of the chain as $\log N$ while it asymptotically decays as $1/r$ with the distance r from its center (Landa, Cormick, and Morigi, 2020). This asymptotic decay gives rise to Coulomb-like interactions between distant solitons (Menu *et al.*, 2024a).

Equation (70) permits the dynamics of a frustrated ion chain to be mapped to a quantum field-theoretical model, the massive Thirring model, where the commensurate phase is an effective Dirac sea and the solitons are charged fermionic excitations, as illustrated in Fig. 53(c). The chemical potential is proportional to the mismatch and shows that, when this exceeds the gap, excitations (solitons) are generated. Because of the Coulomb interactions, the chemical potential also depends on the chain's size: $h' \propto \delta \ln N$. This scaling of h' indicates that the Coulomb interactions dictate the order in the thermodynamic limit. Correspondingly, the critical mismatch δ_c shrinks as $1/\ln N$, giving rise to interaction-induced sliding (Menu *et al.*, 2024a, 2024b). An equivalent spin model can be derived from the Thirring Hamiltonian, which is amenable to numerical analysis. This is a long-range XXZ Hamiltonian of spin-1/2 particles in an external field. The solitons are mapped onto long-range interacting defects, as shown in Fig. 53(d). In these models quantum effects in the soliton's dynamics scale with the effective Planck constant β^2 (Menu *et al.*, 2024a),

$$\beta^2 = \left(\frac{2\pi d_0}{a}\right)^2\sqrt{\frac{2\hbar^2/(3md_0^2)}{2Q^2/(4\pi\epsilon_0 d_0)}}, \quad (71)$$

which is proportional to the square root of the ratio between kinetic and Coulomb energy. This quantity is proportional to $\tilde{\hbar}$, which was introduced in Sec. II.A.5 and which determines the size of quantum effects at the linear-zigzag transition. The proportionality factor contains the ratio $(d_0/a)^2$ between the characteristic length scales of the chain and lattice and suggests that the size of the quantum effects can be tuned by changing the trap aspect ratio and/or the wavelength of the confining lattice. Taking experimentally accessible parameters, the effective Planck constant can range from $\sim 10^{-4}$ deep in the mean-field regime to ~ 0.1 at a point where quantum sliding can be measured (Menu *et al.*, 2024a, 2024b).

A mean-field study predicted the regions of stability of the commensurate configurations at fixed N as a function of the mismatch δ and the temperature T (Menu *et al.*, 2024b). Using the parameters of Bylinskii *et al.* (2016) for a chain of 100 $^{173}Yb^+$ ions with an interparticle distance $d_0 = 6$ μm and a lattice periodicity $a = 185$ nm, commensurate phases can be observed at temperatures $T \lesssim 1$ mK (Menu *et al.*, 2024b). Quantum sliding could be revealed by means of spectroscopic measurements for relative precisions below the effective Planck constant β^2.

IV. CONCLUDING REMARKS AND OUTLOOK

This review reports on advances with ion Coulomb chains and crystals, starting with the state of the art of more than two decades ago, when the non-neutral plasma phase was at the center of the studies (Dubin and O'Neil, 1999). It draws from progress by the quantum optics and quantum information communities that, through advances in laser-cooling techniques and quantum engineering, exploited the utility of ion chains and crystals for quantum sensing and information processing. In the review, we emphasize the physical properties of ion Coulomb crystals and examine several studies of out-of-equilibrium dynamics carried out with ion Coulomb crystals.

In contrast to electronic systems in condensed matter, ion Coulomb crystals give access to a regime that is dominated by interactions rather than the kinetic energy of the particles. Their equilibrium and out-of-equilibrium dynamics is strongly shaped by the long-range potential, where the dominant energy contribution is nonadditive, thus breaking crucial principles of textbook statistical mechanics such as ensemble equivalence (Campa, Dauxois, and Ruffo, 2009). This makes ion Coulomb crystals a prominent laboratory for testing theoretical hypotheses formulated for astrophysical and plasma systems (Campa, Dauxois, and Ruffo, 2009). Moreover, the experimental progress opens the possibility of accessing presently unexplored regimes that can shed light on the onset of equilibrium (Defenu, Lerose, and Pappalardi, 2024) and on quantum phases (Defenu *et al.*, 2023) in the presence of long-range, nonadditive forces.

Exotic quantum phases and critical phenomena are, for instance, the zigzag and buckling structural phase transitions, as well as the topological features of frustrated geometries, such as the Aubry and commensurate-incommensurate transition in ion chains. These are also examples of how discrete internal degrees of freedom, such as spins, are naturally encoded in the structure of a low-dimensional crystal. This paradigm could be generalized to multilayer crystals where the layer index is a discrete degree of freedom that serves as an effective spin, mapping the dynamics to models analogous to antiferromagnetism in frustrated geometries. The long-range nature of topological defects, such as dislocations and kinks, is only partially characterized in one dimension and is unexplored in higher dimensions. One question involves how the coupling between lattice vibrations and topological defects

(dislocations, disclinations, kinks, vortices, etc.) might give rise to metastable structures and novel phases in frustrated geometries with long-range Coulomb forces. This can be seen as an exotic realization of quantum magnetism in dynamic Wigner lattices; see Nath *et al.* (2015) for a related proposal. Such a realization holds the promise for simulating dynamical features of lattice-field theory with trapped ions (Bauer *et al.*, 2023; Băzăvan *et al.*, 2024; Menu *et al.*, 2024a; Kahan *et al.*, 2025). It would be interesting to investigate how the influence of the coupling to the lattice vibrations and defects affects the nature of the magnetic phases (and thus of the layer ordering), as well as the transitions between them (Shamai and Podolsky, 2018; Abutbul and Podolsky, 2022; Samanta, Shimshoni, and Podolsky, 2022; Sarkar *et al.*, 2023).

One peculiar aspect of these systems is that exchange interaction and quantum statistics are small and generally not measurable. Yet, an ingenious experiment measured the Aharonov-Bohm effect in the macroscopic tunneling of a chain of three ions realizing a quantum rotor (Noguchi *et al.*, 2014). Protocols have been proposed for revealing quantum statistics in ion Coulomb crystals (Roos *et al.*, 2017), indicating an avenue for unveiling these phenomena with larger crystals.

The progress reported in this review focused on fundamental aspects of ion Coulomb crystals while intentionally leaving aside the remarkable advances in their use for engineered quantum dynamics in quantum simulation (Blatt and Roos, 2012; Britton *et al.*, 2012; Monroe *et al.*, 2021), quantum computing (Cirac and Zoller, 1995; Bruzewicz *et al.*, 2019; Moses *et al.*, 2023), and quantum metrology and sensing, which we later discuss. Closely related developments include fundamental insights into tailoring correlations between ions with photons by means of optical elements and cavities (Eschner *et al.*, 2001; Casabone *et al.*, 2015) and advanced detection schemes (Moehring *et al.*, 2007; Slodička *et al.*, 2013; Richter *et al.*, 2021), which underpin powerful applications in quantum communication (Duan and Monroe, 2010; Saha *et al.*, 2025). Note that the advances reported here have evolved hand in hand with the development of these applications, leading to a strong cross-fertilization of methods and physical insights.

This interplay suggests that both the scientific reach and the technological impact of ion Coulomb crystals will continue to grow. Many of these applications are rooted in the fact that the internal states of individual ions in a Coulomb crystal are only weakly perturbed by the presence of other ions, making these systems a highly interesting platform for high-resolution spectroscopy, sensing, and metrology (Mehlstäubler *et al.*, 2018). Representative examples in quantum sensing include extremely accurate optical atomic ion clocks (Huntemann *et al.*, 2012; Tofful *et al.*, 2024; Marshall *et al.*, 2025), ultrahigh-resolution spectroscopy of molecular ions (Chou *et al.*, 2020; Kortunov *et al.*, 2021), and precision sensing of weak electromagnetic fields (Kotler *et al.*, 2011; Ruster *et al.*, 2017; Gilmore *et al.*, 2021; McKay *et al.*, 2021). Notably, a recent multi-ion clock based on a linear chain of 4 $^{115}In^{+}$ ions sympathetically cooled by eight $^{172}Yb^{+}$ ions demonstrated a fractional frequency instability of 9.2×10^{-16} at 1 s averaging time (Hausser *et al.*, 2025).

These quantum sensing capabilities can in turn be used as powerful probes of fundamental physics, enabling tests of Lorentz invariance (Megidish *et al.*, 2019; Dreissen *et al.*, 2022), searches for temporal variations of fundamental constants (Rosenband *et al.*, 2008; Dzuba, Flambaum, and Mansour, 2024), searches for particles beyond the standard model (Gebert *et al.*, 2015; Counts *et al.*, 2020; Solaro *et al.*, 2020; Door *et al.*, 2025), and searches for signatures of potential extensions to quantum mechanics (Lenler-Eriksen, Drewsen, and Carlesso, 2024).

We thus expect many further developments in this field, where atomic, molecular, optical, statistical, and, most recently, condensed-matter physics merge in verifying hypotheses and providing novel insights into the physics of Wigner crystallization with trapped ions. This progress will open new paths toward understanding the onset and stability of long-range interacting quantum structures and will offer exciting perspectives for technological advances in the quantum control of complex systems.

ACKNOWLEDGMENTS

We are indebted to our close collaborators Daniel Dubin, Shmuel Fishman, Herbert Walther, and David Wineland, with whom we had the privilege to work over the years on this fascinating subject. We further had the privilege to share many useful discussions and insights with a number of colleagues and collaborators. Owing to space limitations, we refrain from mentioning them all and explicitly list our collaborators on ion Coulomb crystal work: Matt Affolter, Francois Anderegg, Jens Baltrusch, Rainer Blatt, Joseph Britton, Andreas Buchleitner, Tommaso Calarco, Florian Cartarius, Allison Carter, Caroline Champenois, Oksana Chelpanova, Maria-Luisa Chiofalo, Cecilia Cormick, Gabriele De Chiara, Adolfo del Campo, J. Ignacio Cirac, Aurelien Dantan, C. Fred Driscoll, Jürgen Eschner, Thomas Fogarty, James Freericks, Jeffrey S. Hangst, Jan-Petter Hansen, Peter Horak, Liv Hornekær, X.-P. Huang, Wayne Itano, Endre Kajari, Martina Knoop, Jan Kiethe, Niels Kjærgaard, Haggai Landa, Thomas Lauprêtre, Dietrich Leibfried, Ian D. Leroux, Jamir Marino, Thierry Matthey, Tanja E. Mehlstäubler, Raphael Menu, Travis Mitchell, Simone Montangero, Ramil Nigmatullin, Thomas O'Neil, Scott Parker, Martin Plenio, Dirk Reiß, Alex Retzker, Ana Maria Rey, Benni Reznik, Brian Sawyer, Tobias Schätz, Ferdinand Schmidt-Kaler, John P. Schiffer, Wolfgang Schleich, Athreya Shankar, Pietro Silvi, Cyrille Solaro, Bruno Taketani, Joseph Tan, Lars Timm, Vladan Vuletić, Christof Wunderlich, and Jorge Yago-Malo. We are grateful to Daniel Dubin and Jennifer Lilieholm for their critical reading of the manuscript.

DATA AVAILABILITY

There are no publicly available research data or software supporting this manuscript. Requests for further information or data should be sent to the authors.

REFERENCES

Abdelrahman, A., *et al.*, 2017, Nat. Commun. **8**, 15712.
Abutbul, D., and D. Podolsky, 2022, Phys. Rev. Lett. **128**, 255501.
Anderegg, F., C. F. Driscoll, D. H. E. Dubin, and T. M. O'Neil, 2010, Phys. Plasmas **17**, 055702.

Anderegg, F., D. H. E. Dubin, T. M. O'Neil, and C. F. Driscoll, 2009, Phys. Rev. Lett. **102**, 185001.

Andrei, E. Y., G. Deville, D. C. Glattli, F. I. B. Williams, E. Paris, and B. Etienne, 1988, Phys. Rev. Lett. **60**, 2765.

Andresen, G. B., *et al.* (ALPHA Collaboration), 2011, Nat. Phys. **7**, 558.

Arias Espinoza, J. D., M. Mazzanti, K. Fouka, R. X. Schüssler, Z. Wu, P. Corboz, R. Gerritsma, and A. Safavi-Naini, 2021, Phys. Rev. A **104**, 013302.

Ashcroft, N. W., and N. D. Mermin, 1976, *Solid State Physics* (Saunders, Philadelphia).

Baiko, D. A., 2009, Phys. Rev. E **80**, 046405.

Baiko, D. A., A. Y. Potekhin, and D. G. Yakovlev, 2001, Phys. Rev. E **64**, 057402.

Ball, H., C. D. Marciniak, R. N. Wolf, A. T.-H. Hung, K. Pyka, and M. J. Biercuk, 2019, Rev. Sci. Instrum. **90**, 053103.

Baltrusch, J. D., C. Cormick, G. De Chiara, T. Calarco, and G. Morigi, 2011, Phys. Rev. A **84**, 063821.

Baltrusch, J. D., C. Cormick, and G. Morigi, 2012, Phys. Rev. A **86**, 032104.

Baltrusch, J. D., C. Cormick, and G. Morigi, 2013, Phys. Rev. A **87**, 032116.

Baltrusch, J. D., A. Negretti, J. M. Taylor, and T. Calarco, 2011, Phys. Rev. A **83**, 042319.

Bauer, C. W., *et al.*, 2023, PRX Quantum **4**, 027001.

Baughman, R. H., S. O. Dantas, S. Stafström, A. A. Zakhidov, T. B. Mitchell, and D. H. E. Dubin, 2000, Science **288**, 2018.

Baus, M., and J.-P. Hansen, 1980, Phys. Rep. **59**, 1.

Băzăvan, O., S. Saner, E. Tirrito, G. Araneda, R. Srinivas, and A. Bermudez, 2024, Commun. Phys. **7**, 229.

Bechinger, C., M. Brunner, and P. Leiderer, 2001, Phys. Rev. Lett. **86**, 930.

Benassi, A., A. Vanossi, and E. Tosatti, 2011, Nat. Commun. **2**, 236.

Bergeson, S. D., S. D. Baalrud, C. L. Ellison, E. Grant, F. R. Graziani, T. C. Killian, M. S. Murillo, J. L. Roberts, and L. G. Stanton, 2019, Phys. Plasmas **26**, 100501.

Bermudez, A., J. Almeida, K. Ott, H. Kaufmann, S. Ulm, U. Poschinger, F. Schmidt-Kaler, A. Retzker, and M. B. Plenio, 2012, New J. Phys. **14**, 093042.

Bermudez, A., M. Bruderer, and M. B. Plenio, 2013, Phys. Rev. Lett. **111**, 040601.

Birkl, G., S. Kassner, and H. Walther, 1992, Nature (London) **357**, 310.

Birkl, G., J. A. Yeazell, R. RÃŒckerl, and H. Walther, 1994, Europhys. Lett. **27**, 197.

Blatt, R., and C. F. Roos, 2012, Nat. Phys. **8**, 277.

Block, M., A. Drakoudis, H. Leuthner, P. Seibert, G. Werth, M. Block, A. Drakoudis, H. Leuthner, and P. Seibert, 2000, J. Phys. B **33**, L375.

Blümel, R., C. Kappler, W. Quint, and H. Walther, 1989, Phys. Rev. A **40**, 808.

Bohnet, J. G., B. C. Sawyer, J. W. Britton, M. L. Wall, A. M. Rey, M. Foss-Feig, and J. J. Bollinger, 2016, Science **352**, 1297.

Bollinger, J. J., D. J. Heinzen, F. L. Moore, W. M. Itano, D. J. Wineland, and D. H. E. Dubin, 1993, Phys. Rev. A **48**, 525.

Bollinger, J. J., T. B. Mitchell, X.-P. Huang, W. M. Itano, J. N. Tan, B. M. Jelenković, and D. J. Wineland, 2000, Phys. Plasmas **7**, 7.

Bonetti, P. M., A. Rucci, M. L. Chiofalo, and V. Vuletić, 2021, Phys. Rev. Res. **3**, 013031.

Braiman, Y., J. Baumgarten, J. Jortner, and J. Klafter, 1990, Phys. Rev. Lett. **65**, 2398.

Braun, O., and Y. Kivshar, 2004, *The Frenkel-Kontorova Model: Concepts, Methods, and Applications* (Springer, New York).

Braun, O. M., Y. S. Kivshar, and I. I. Zelenskaya, 1990, Phys. Rev. B **41**, 7118.

Brewer, L. R., J. D. Prestage, J. J. Bollinger, W. M. Itano, D. J. Larson, and D. J. Wineland, 1988, Phys. Rev. A **38**, 859.

Brillouin, L., 1945, Phys. Rev. **67**, 260.

Britton, J. W., B. C. Sawyer, A. C. Keith, C.-C. J. Wang, J. K. Freericks, H. Uys, M. J. Biercuk, and J. J. Bollinger, 2012, Nature (London) **484**, 489.

Brown, K. R., C. Ospelkaus, Y. Colombe, A. C. Wilson, D. Leibfried, and D. J. Wineland, 2011, Nature (London) **471**, 196.

Brown, L. S., and G. Gabrielse, 1986, Rev. Mod. Phys. **58**, 233.

Brox, J., P. Kiefer, M. Bujak, T. Schaetz, and H. Landa, 2017, Phys. Rev. Lett. **119**, 153602.

Brush, S. G., H. L. Sahlin, and E. Teller, 1966, J. Chem. Phys. **45**, 2102.

Bruzewicz, C. D., J. Chiaverini, R. McConnell, and J. M. Sage, 2019, Appl. Phys. Rev. **6**, 021314.

Bubeck, R., C. Bechinger, S. Neser, and P. Leiderer, 1999, Phys. Rev. Lett. **82**, 3364.

Bylinskii, A., D. Gangloff, I. Counts, and V. Vuletić, 2016, Nat. Mater. **15**, 717.

Bylinskii, A., D. Gangloff, and V. Vuletić, 2015, Science **348**, 1115.

Calvo, F., E. Yurtsever, and D. J. Wales, 2012, J. Chem. Phys. **136**, 024303.

Campa, A., T. Dauxois, and S. Ruffo, 2009, Phys. Rep. **480**, 57.

Cartarius, F., C. Cormick, and G. Morigi, 2013, Phys. Rev. A **87**, 013425.

Casabone, B., K. Friebe, B. Brandstätter, K. Schüppert, R. Blatt, and T. E. Northup, 2015, Phys. Rev. Lett. **114**, 023602.

Cetina, M., A. Bylinskii, L. Karpa, D. Gangloff, K. M. Beck, Y. Ge, M. Scholz, A. T. Grier, I. Chuang, and V. Vuletić, 2013, New J. Phys. **15**, 053001.

Chabrier, G., N. W. Ashcroft, and H. E. DeWitt, 1992, Nature (London) **360**, 48.

Champenois, C., 2009, J. Phys. B **42**, 154002.

Champenois, C., M. Marciante, J. Pedregosa-Gutierrez, M. Houssin, M. Knoop, and M. Kajita, 2010, Phys. Rev. A **81**, 043410.

Chelpanova, O., S. P. Kelly, G. Morigi, F. Schmidt-Kaler, and J. Marino, 2023, Europhys. Lett. **143**, 25002.

Chelpanova, O., S. P. Kelly, F. Schmidt-Kaler, G. Morigi, and J. Marino, 2024, Phys. Rev. B **109**, 214107.

Chen, J.-S., S. M. Brewer, C. W. Chou, D. J. Wineland, D. R. Leibrandt, and D. B. Hume, 2017, Phys. Rev. Lett. **118**, 053002.

Chen, S.-J., and D. H. E. Dubin, 1993, Phys. Rev. Lett. **71**, 2721.

Chou, C. W., A. L. Collopy, C. Kurz, Y. Lin, M. E. Harding, P. N. Plessow, T. Fortier, S. Diddams, D. Leibfried, and D. R. Leibrandt, 2020, Science **367**, 1458.

Chu, S., 1998, Rev. Mod. Phys. **70**, 685.

Cirac, J. I., and P. Zoller, 1995, Phys. Rev. Lett. **74**, 4091.

Clark, C. B., 1958, Phys. Rev. **109**, 1133.

Cohen-Tannoudji, C. N., 1998, Rev. Mod. Phys. **70**, 707.

Cormick, C., and G. Morigi, 2012, Phys. Rev. Lett. **109**, 053003.

Cormick, C., and G. Morigi, 2013, Phys. Rev. A **87**, 013829.

Cormick, C., T. Schaetz, and G. Morigi, 2011, New J. Phys. **13**, 043019.

Cosco, F., M. Borrelli, P. Silvi, S. Maniscalco, and G. De Chiara, 2017, Phys. Rev. A **95**, 063615.

Counts, I., J. Hur, D. P. L. Aude Craik, H. Jeon, C. Leung, J. C. Berengut, A. Geddes, A. Kawasaki, W. Jhe, and V. Vuletić, 2020, Phys. Rev. Lett. **125**, 123002.

Dantan, A., J. P. Marler, M. Albert, D. Guénot, and M. Drewsen, 2010, Phys. Rev. Lett. **105**, 103001.

Davidson, R. C., 2001, *Physics of Nonneutral Plasmas*, 2nd ed. (Imperial College Press, London).

Debnath, S., N. M. Linke, S.-T. Wang, C. Figgatt, K. A. Landsman, L.-M. Duan, and C. Monroe, 2018, Phys. Rev. Lett. **120**, 073001.

De Chiara, G., T. Calarco, S. Fishman, and G. Morigi, 2008, Phys. Rev. A **78**, 043414.

De Chiara, G., A. del Campo, G. Morigi, M. B. Plenio, and A. Retzker, 2010, New J. Phys. **12**, 115003.

Defenu, N., T. Donner, T. Macrì, G. Pagano, S. Ruffo, and A. Trombettoni, 2023, Rev. Mod. Phys. **95**, 035002.

Defenu, N., A. Lerose, and S. Pappalardi, 2024, Phys. Rep. **1074**, 1.

deGrassie, J. S., and J. H. Malmberg, 1977, Phys. Rev. Lett. **39**, 1077.

deGrassie, J. S., and J. H. Malmberg, 1980, Phys. Fluids **23**, 63.

del Campo, A., G. De Chiara, G. Morigi, M. B. Plenio, and A. Retzker, 2010, Phys. Rev. Lett. **105**, 075701.

del Campo, A., T. W. B. Kibble, and W. H. Zurek, 2013, J. Phys. Condens. Matter **25**, 404210.

Delfau, J.-B., C. Coste, and M. Saint Jean, 2013, Phys. Rev. E **87**, 062135.

DeWitt, H., and W. Slattery, 1999, Contrib. Plasma Phys. **39**, 97.

Diedrich, F., J. C. Bergquist, W. M. Itano, and D. J. Wineland, 1989, Phys. Rev. Lett. **62**, 403.

Diedrich, F., E. Peik, J. M. Chen, W. Quint, and H. Walther, 1987, Phys. Rev. Lett. **59**, 2931.

Ding, S., G. Maslennikov, R. Hablützel, H. Loh, and D. Matsukevich, 2017, Phys. Rev. Lett. **119**, 150404.

D'Onofrio, M., Y. Xie, A. J. Rasmusson, E. Wolanski, J. Cui, and P. Richerme, 2021, Phys. Rev. Lett. **127**, 020503.

Door, M., *et al.*, 2025, Phys. Rev. Lett. **134**, 063002.

Dreissen, L. S., C.-H. Yeh, H. A. Fürst, K. C. Grensemann, and T. E. Mehlstäubler, 2022, Nat. Commun. **13**, 7314.

Drewsen, M., 2015, Physica B (Amsterdam) **460**, 105.

Drewsen, M., C. Brodersen, L. Hornekær, J. S. Hangst, and J. P. Schifffer, 1998, Phys. Rev. Lett. **81**, 2878.

Drewsen, M., and A. Brøner, 2000, Phys. Rev. A **62**, 045401.

Drewsen, M., I. S. Jensen, N. Kjærgaard, J. Lindballe, A. Mortensen, K. Mølhave, and D. Voigt, 2003, J. Phys. B **36**, 525.

Drewsen, M., T. Matthey, A. Mortensen, and J. P. Hansen, 2012, arXiv:1202.2544.

Driscoll, C. F., J. H. Malmberg, and K. S. Fine, 1988, Phys. Rev. Lett. **60**, 1290.

Duan, L.-M., and C. Monroe, 2010, Rev. Mod. Phys. **82**, 1209.

Dubin, D. H. E., 1989, Phys. Rev. A **40**, 1140.

Dubin, D. H. E., 1990, Phys. Rev. A **42**, 4972.

Dubin, D. H. E., 1991, Phys. Rev. Lett. **66**, 2076.

Dubin, D. H. E., 1993, Phys. Rev. Lett. **71**, 2753.

Dubin, D. H. E., 1997, Phys. Rev. E **55**, 4017.

Dubin, D. H. E., 2013, Phys. Rev. A **88**, 013403.

Dubin, D. H. E., 2020, Phys. Plasmas **27**, 102107.

Dubin, D. H. E., and T. M. O'Neil, 1988, Phys. Rev. Lett. **60**, 511.

Dubin, D. H. E., and T. M. O'Neil, 1999, Rev. Mod. Phys. **71**, 87.

Dubin, D. H. E., and J. P. Schiffer, 1996, Phys. Rev. E **53**, 5249.

Dyson, F. J., 1953, Phys. Rev. **92**, 1331.

Dzuba, V. A., V. V. Flambaum, and A. J. Mansour, 2024, Phys. Rev. D **110**, 055022.

Earnshaw, S., 1842, Trans. Cambridge Philos. Soc. **7**, 97, https://archive.org/details/transactionsofca07camb/page/96/mode/2up.

Ejtemaee, S., and P. C. Haljan, 2013, Phys. Rev. A **87**, 051401.

Enderlein, M., T. Huber, C. Schneider, and T. Schaetz, 2012, Phys. Rev. Lett. **109**, 233004.

Enzer, D. G., *et al.*, 2000, Phys. Rev. Lett. **85**, 2466.

Eschner, J., G. Morigi, F. Schmidt-Kaler, and R. Blatt, 2003, J. Opt. Soc. Am. B **20**, 1003.

Eschner, J., C. Raab, F. Schmidt-Kaler, and R. Blatt, 2001, Nature (London) **413**, 495.

Farouki, R. T., and S. Hamaguchi, 1993, Phys. Rev. E **47**, 4330.

Feldker, T., L. Pelzer, M. Stappel, P. Bachor, R. Steinborn, D. Kolbe, J. Walz, and F. Schmidt-Kaler, 2014, Appl. Phys. B **114**, 11.

Feng, L., W. L. Tan, A. De, A. Menon, A. Chu, G. Pagano, and C. Monroe, 2020, Phys. Rev. Lett. **125**, 053001.

Fishman, S., G. De Chiara, T. Calarco, and G. Morigi, 2008, Phys. Rev. B **77**, 064111.

Fogarty, T., C. Cormick, H. Landa, V. M. Stojanović, E. Demler, and G. Morigi, 2015, Phys. Rev. Lett. **115**, 233602.

Fogarty, T., E. Kajari, B. G. Taketani, A. Wolf, T. Busch, and G. Morigi, 2013, Phys. Rev. A **87**, 050304.

Fogarty, T., H. Landa, C. Cormick, and G. Morigi, 2016, Phys. Rev. A **94**, 023844.

Gabrielse, G., *et al.* (ATRAP Collaboration), 2012, Phys. Rev. Lett. **108**, 113002.

Gajewski, M., W. Li, S. Wolf, W. Hahn, C. E. Düllmann, D. Budker, G. Morigi, and F. Schmidt-Kaler, 2022, Phys. Rev. A **106**, 033108.

Gangloff, D., A. Bylinskii, I. Counts, W. Jhe, and V. Vuletić, 2015, Nat. Phys. **11**, 915.

Gangloff, D. A., A. Bylinskii, and V. Vuletić, 2020, Phys. Rev. Res. **2**, 013380.

Gann, R. C., S. Chakravarty, and G. V. Chester, 1979, Phys. Rev. B **20**, 326.

Garcia-Mata, I., O. V. Zhirov, and D. L. Shepelyansky, 2007, Eur. Phys. J. D **41**, 325.

Gärttner, M., J. G. Bohnet, A. Safavi-Naini, M. L. Wall, J. J. Bollinger, and A. M. Rey, 2017, Nat. Phys. **13**, 781.

Gebert, F., Y. Wan, F. Wolf, C. N. Angstmann, J. C. Berengut, and P. O. Schmidt, 2015, Phys. Rev. Lett. **115**, 053003.

Gerlich, D., 1992, in *Advances in Chemical Physics*, edited by C.-Y. Ng, M. Baer, I. Prigogine, and S. A. Rice (John Wiley & Sons, New York), pp. 1–176, 10.1002/9780470141397.ch1.

Gerlich, D., 1995, Phys. Scr. 256.

Ghosh, P. K., 1995, *Ion Traps* (Oxford University Press, New York), https://academic.oup.com/book/0/chapter/422683010/chapter-pdf/52583496/isbn-9780198539957-front-matter-part-1.pdf.

Gilbert, S. L., J. J. Bollinger, and D. J. Wineland, 1988, Phys. Rev. Lett. **60**, 2022.

Gilmore, K. A., M. Affolter, R. J. Lewis-Swan, D. Barberena, E. Jordan, A. M. Rey, and J. J. Bollinger, 2021, Science **373**, 673.

Gong, Z.-X., G.-D. Lin, and L.-M. Duan, 2010, Phys. Rev. Lett. **105**, 265703.

Gorman, D. J., B. Hemmerling, E. Megidish, S. A. Moeller, P. Schindler, M. Sarovar, and H. Häffner, 2018, Phys. Rev. X **8**, 011038.

Gorman, D. J., P. Schindler, S. Selvarajan, N. Daniilidis, and H. Häffner, 2014, Phys. Rev. A **89**, 062332.

Grimes, C., and G. Adams, 1980, Surf. Sci. **98**, 1.

Grimm, R., M. Weidemüller, and Y. B. Ovchinnikov, 2000, Adv. At. Mol. Opt. Phys., **42**, 95.

Guo, S.-A., *et al.*, 2024, Nature (London) **630**, 613.

Guthöhrlein, G. R., M. Keller, K. Hayasaka, W. Lange, and H. Walther, 2001, Nature (London) **414**, 49.

Häffner, H., C. Roos, and R. Blatt, 2008, Phys. Rep. **469**, 155.

Hakelberg, F., P. Kiefer, M. Wittemer, U. Warring, and T. Schaetz, 2019, Phys. Rev. Lett. **123**, 100504.

Harlander, M., R. Lechner, M. Brownnutt, R. Blatt, and W. Hänsel, 2011, Nature (London) **471**, 200.

Hasse, R. W., 1992, Phys. Rev. A **46**, 5189.

Hasse, R. W., 2003, J. Phys. B **36**, 1011.

Hasse, R. W., and V. V. Avilov, 1991, Phys. Rev. A **44**, 4506.

Hasse, R. W., and J. P. Schiffer, 1990, Ann. Phys. (N.Y.) **203**, 419.
Hausser, H. N., *et al.*, 2025, Phys. Rev. Lett. **134**, 023201.
Hawaldar, S., P. Shahi, A. L. Carter, A. M. Rey, J. J. Bollinger, and A. Shankar, 2024, Phys. Rev. X **14**, 031030.
Haze, S., Y. Tateishi, A. Noguchi, K. Toyoda, and S. Urabe, 2012, Phys. Rev. A **85**, 031401.
Heinzen, D. J., J. J. Bollinger, F. L. Moore, W. M. Itano, and D. J. Wineland, 1991, Phys. Rev. Lett. **66**, 2080.
Hoenig, D., F. Thielemann, L. Karpa, T. Walker, A. Mohammadi, and T. Schaetz, 2023, arXiv:2306.12518.
Hohenberg, P. C., 1967, Phys. Rev. **158**, 383.
Home, J. P., 2013, in *Advances in Atomic, Molecular, and Optical Physics*, Vol. 62, edited by E. Arimondo, P. R. Berman, and C. C. Lin (Academic Press, New York), pp. 231–277.
Home, J. P., D. Hanneke, J. D. Jost, D. Leibfried, and D. J. Wineland, 2011, New J. Phys. **13**, 073026.
Horak, P., A. Dantan, and M. Drewsen, 2012, Phys. Rev. A **86**, 043435.
Hornekær, L., and M. Drewsen, 2002, Phys. Rev. A **66**, 013412.
Hornekær, L., N. Kjærgaard, A. M. Thommesen, and M. Drewsen, 2001, Phys. Rev. Lett. **86**, 1994.
Hou, P.-Y., J. J. Wu, S. D. Erickson, G. Zarantonello, A. D. Brandt, D. C. Cole, A. C. Wilson, D. H. Slichter, and D. Leibfried, 2024, Phys. Rev. X **14**, 021003.
Huang, X.-P., F. Anderegg, E. M. Hollmann, C. F. Driscoll, and T. M. O'Neil, 1997, Phys. Rev. Lett. **78**, 875.
Huang, X.-P., J. J. Bollinger, T. B. Mitchell, and W. M. Itano, 1998, Phys. Rev. Lett. **80**, 73.
Huang, X.-P., J. J. Bollinger, T. B. Mitchell, W. M. Itano, and D. H. E. Dubin, 1998, Phys. Plasmas **5**, 1656.
Huntemann, N., M. Okhapkin, B. Lipphardt, S. Weyers, C. Tamm, and E. Peik, 2012, Phys. Rev. Lett. **108**, 090801.
Ichimaru, S., 1982, Rev. Mod. Phys. **54**, 1017.
Ichimaru, S., H. Iyetomi, and S. Tanaka, 1987, Phys. Rep. **149**, 91.
Imajo, H., K. Hayasaka, R. Ohmukai, U. Tanaka, M. Watanabe, and S. Urabe, 1997, Phys. Rev. A **55**, 1276.
Itano, W. M., J. J. Bollinger, J. N. Tan, B. Jelenković, X.-P. Huang, and D. J. Wineland, 1998, Science **279**, 686.
Jain, S., J. Alonso, M. Grau, and J. P. Home, 2020, Phys. Rev. X **10**, 031027.
Jain, S., *et al.*, 2024, Nature (London) **627**, 510.
James, D. F. V., 1998, Appl. Phys. B **66**, 181.
Jensen, M. J., T. Hasegawa, and J. J. Bollinger, 2004, Phys. Rev. A **70**, 033401.
Johanning, M., A. F. Varón, and C. Wunderlich, 2009, J. Phys. B **42**, 154009.
Johnson, W., A. Shankar, J. Zaris, J. J. Bollinger, and S. E. Parker, 2024, Phys. Rev. A **109**, L021102.
Jordan, E., K. A. Gilmore, A. Shankar, A. Safavi-Naini, J. G. Bohnet, M. J. Holland, and J. J. Bollinger, 2019, Phys. Rev. Lett. **122**, 053603.
José, J. V., L. P. Kadanoff, S. Kirkpatrick, and D. R. Nelson, 1977, Phys. Rev. B **16**, 1217.
Joshi, M. K., A. Fabre, C. Maier, T. Brydges, D. Kiesenhofer, H. Hainzer, R. Blatt, and C. F. Roos, 2020, New J. Phys. **22**, 103013.
Kahan, A., and C. Cormick, 2024, Phys. Rev. A **110**, 012461.
Kahan, A., P. Vinas, T. V. Zache, and A. Bermudez, 2025, arXiv:2512.07748.
Kamsap, M. R., C. Champenois, J. Pedregosa-Gutierrez, S. Mahler, M. Houssin, and M. Knoop, 2017, Phys. Rev. A **95**, 013413.
Kato, A., A. Goel, R. Lee, Z. Ye, S. Karki, J. J. Liu, A. Nomerotski, and B. B. Blinov, 2022, Phys. Rev. A **105**, 023101.
Kaufmann, H., S. Ulm, G. Jacob, U. Poschinger, H. Landa, A. Retzker, M. B. Plenio, and F. Schmidt-Kaler, 2012, Phys. Rev. Lett. **109**, 263003.
Keller, J., *et al.*, 2024, J. Phys. Conf. Ser. **2889**, 012050.
Keller, M., B. Lange, K. Hayasaka, W. Lange, and H. Walther, 2004, Nature (London) **431**, 1075.
Kibble, T., 1980, Phys. Rep. **67**, 183.
Kiesenhofer, D., H. Hainzer, A. Zhdanov, P. C. Holz, M. Bock, T. Ollikainen, and C. F. Roos, 2023, PRX Quantum **4**, 020317.
Kiethe, J., R. Nigmatullin, D. Kalincev, T. Schmirander, and T. E. Mehlstäubler, 2017, Nat. Commun. **8**, 15364.
Kiethe, J., R. Nigmatullin, T. Schmirander, D. Kalincev, and T. E. Mehlstäubler, 2018, New J. Phys. **20**, 123017.
Kiethe, J., L. Timm, H. Landa, D. Kalincev, G. Morigi, and T. E. Mehlstäubler, 2021, Phys. Rev. B **103**, 104106.
Kittel, C., 1991, *Quantum Theory of Solids*, 2nd ed. (Wiley, New York).
Kjærgaard, N., and M. Drewsen, 2003, Phys. Rev. Lett. **91**, 095002.
Kortunov, I. V., S. Alighanbari, M. G. Hansen, G. S. Giri, V. I. Korobov, and S. Schiller, 2021, Nat. Phys. **17**, 569.
Kotler, S., N. Akerman, Y. Glickman, A. Keselman, and R. Ozeri, 2011, Nature (London) **473**, 61.
Koulakov, A. A., and B. I. Shklovskii, 1998, Phys. Rev. B **57**, 2352.
Krajewski, F. R., and M. H. Müser, 2004, Phys. Rev. Lett. **92**, 030601.
Kriesel, J. M., J. J. Bollinger, T. B. Mitchell, L. B. King, and D. H. E. Dubin, 2002, Phys. Rev. Lett. **88**, 125003.
Landa, H., C. Cormick, and G. Morigi, 2020, Condens. Matter **5**, 35.
Landa, H., M. Drewsen, B. Reznik, and A. Retzker, 2012a, J. Phys. A **45**, 455305.
Landa, H., M. Drewsen, B. Reznik, and A. Retzker, 2012b, New J. Phys. **14**, 093023.
Landa, H., S. Marcovitch, A. Retzker, M. B. Plenio, and B. Reznik, 2010, Phys. Rev. Lett. **104**, 043004.
Landa, H., A. Retzker, T. Schaetz, and B. Reznik, 2014, Phys. Rev. Lett. **113**, 053001.
Landa, H., B. Reznik, J. Brox, M. Mielenz, and T. Schaetz, 2013, New J. Phys. **15**, 093003.
Langin, T. K., G. M. Gorman, and T. C. Killian, 2019, Science **363**, 61.
Larson, D. J., J. C. Bergquist, J. J. Bollinger, W. M. Itano, and D. J. Wineland, 1986, Phys. Rev. Lett. **57**, 70.
Lauprêtre, T., R. B. Linnet, I. D. Leroux, H. Landa, A. Dantan, and M. Drewsen, 2019, Phys. Rev. A **99**, 031401.
Lechner, R., C. Maier, C. Hempel, P. Jurcevic, B. P. Lanyon, T. Monz, M. Brownnutt, R. Blatt, and C. F. Roos, 2016, Phys. Rev. A **93**, 053401.
Lenler-Eriksen, E., M. Drewsen, and M. Carlesso, 2024, New J. Phys. **26**, 113008.
Li, H., *et al.*, 2024, Science **385**, 86.
Li, H.-K., *et al.*, 2017, Phys. Rev. Lett. **118**, 053001.
Li, J., L. L. Yan, L. Chen, Z. C. Liu, F. Zhou, J. Q. Zhang, W. L. Yang, and M. Feng, 2019, Phys. Rev. A **99**, 063402.
Li, W., and I. Lesanovsky, 2012, Phys. Rev. Lett. **108**, 023003.
Li, W., S. Wolf, L. Klein, D. Budker, C. E. Dullmann, and F. Schmidt-Kaler, 2022, New J. Phys. **24**, 043028.
Lin, G.-D., and L.-M. Duan, 2011, New J. Phys. **13**, 075015.
Lin, G.-D., S.-L. Zhu, R. Islam, K. Kim, M.-S. Chang, S. Korenblit, C. Monroe, and L.-M. Duan, 2009, Europhys. Lett. **86**, 60004.
Lin, Y., J. P. Gaebler, T. R. Tan, R. Bowler, J. D. Jost, D. Leibfried, and D. J. Wineland, 2013, Phys. Rev. Lett. **110**, 153002.
Linnet, R. B., I. D. Leroux, M. Marciante, A. Dantan, and M. Drewsen, 2012, Phys. Rev. Lett. **109**, 233005.
Liu, B., and J. Goree, 2005, Phys. Rev. E **71**, 046410.

Lou, J., A. W. Sandvik, and L. Balents, 2007, Phys. Rev. Lett. **99**, 207203.
Lysne, N. K., J. F. Niedermeyer, A. C. Wilson, D. H. Slichter, and D. Leibfried, 2024, Phys. Rev. Lett. **133**, 033201.
Mallweger, M., N. Kuk, V. Shankar, R. Thomm, H. Parke, I. Straka, W. Li, I. Lesanovsky, and M. Hennrich, 2025, arXiv:2507.23631.
Malmberg, J. H., and T. M. O'Neil, 1977, Phys. Rev. Lett. **39**, 1333.
Marshall, M. C., *et al.*, 2025, Phys. Rev. Lett. **135**, 033201.
Martins, W. S., M. Hennrich, F. Schmidt-Kaler, and I. Lesanovsky, 2026, arXiv:2601.01626.
Maslennikov, G., S. Ding, R. Hablützel, J. Gan, A. Roulet, S. Nimmrichter, J. Dai, V. Scarani, and D. Matsukevich, 2019, Nat. Commun. **10**, 202.
Matthey, T., J. P. Hansen, and M. Drewsen, 2003, Phys. Rev. Lett. **91**, 165001.
Mavadia, S., J. F. Goodwin, G. Stutter, S. Bharadia, D. R. Crick, D. M. Segal, and R. C. Thompson, 2013, Nat. Commun. **4**, 2571.
Mazzanti, M., R. X. Schüssler, J. D. Arias Espinoza, Z. Wu, R. Gerritsma, and A. Safavi-Naini, 2021, Phys. Rev. Lett. **127**, 260502.
McKay, K. S., D. A. Hite, P. D. Kent, S. Kotler, D. Leibfried, D. H. Slichter, A. C. Wilson, and D. P. Pappas, 2021, Phys. Rev. A **104**, 052610.
McMahon, B. J., K. R. Brown, C. D. Herold, and B. C. Sawyer, 2024, Phys. Rev. Lett. **133**, 173201.
Megidish, E., J. Broz, N. Greene, and H. Häffner, 2019, Phys. Rev. Lett. **122**, 123605.
Mehlstäubler, T. E., G. Grosche, C. Lisdat, P. O. Schmidt, and H. Denker, 2018, Rep. Prog. Phys. **81**, 064401.
Menu, R., J. Y. Malo, V. Vuletić, M. L. Chiofalo, and G. Morigi, 2024a, Phys. Rev. B **110**, 155121.
Menu, R., J. Yago Malo, V. Vuletić, M. L. Chiofalo, and G. Morigi, 2024b, Phys. Rev. B **110**, 224103.
Mermin, N. D., and H. Wagner, 1966, Phys. Rev. Lett. **17**, 1133.
Mielenz, M., J. Brox, S. Kahra, G. Leschhorn, M. Albert, T. Schaetz, H. Landa, and B. Reznik, 2013, Phys. Rev. Lett. **110**, 133004.
Mielenz, M., *et al.*, 2016, Nat. Commun. **7**, ncomms11839.
Mihalcea, B. M., V. S. Filinov, R. A. Syrovatka, and L. M. Vasilyak, 2023, Phys. Rep. **1016**, 1.
Mitchell, T. B., J. J. Bollinger, D. H. E. Dubin, X.-P. Huang, W. M. Itano, and R. H. Baughman, 1998, Science **282**.
Mitchell, T. B., J. J. Bollinger, X.-P. Huang, and W. M. Itano, 1998, Opt. Express **2**, 314.
Mitchell, T. B., J. J. Bollinger, W. M. Itano, and D. H. E. Dubin, 2001, Phys. Rev. Lett. **87**, 183001.
Moehring, D. L., P. Maunz, S. Olmschenk, K. C. Younge, D. N. Matsukevich, L. M. Duan, and C. Monroe, 2007, Nature (London) **449**, 68.
Mølhave, K., and M. Drewsen, 2000, Phys. Rev. A **62**, 011401.
Monroe, C., D. M. Meekhof, B. E. King, S. R. Jefferts, W. M. Itano, D. J. Wineland, and P. Gould, 1995, Phys. Rev. Lett. **75**, 4011.
Monroe, C., *et al.*, 2021, Rev. Mod. Phys. **93**, 025001.
Morigi, G., 2003, Phys. Rev. A **67**, 033402.
Morigi, G., and J. Eschner, 2001, Phys. Rev. A **64**, 063407.
Morigi, G., and J. Eschner, 2003, J. Phys. B **36**, 1041.
Morigi, G., J. Eschner, and C. H. Keitel, 2000, Phys. Rev. Lett. **85**, 4458.
Morigi, G., and S. Fishman, 2004a, Phys. Rev. E **70**, 066141.
Morigi, G., and S. Fishman, 2004b, Phys. Rev. Lett. **93**, 170602.
Morigi, G., and S. Fishman, 2006, J. Phys. B **39**, S221.
Morigi, G., and H. Walther, 2001, Eur. Phys. J. D **13**, 261.
Mortensen, A., E. Nielsen, T. Matthey, and M. Drewsen, 2006, Phys. Rev. Lett. **96**, 103001.
Mortensen, A., E. Nielsen, T. Matthey, and M. Drewsen, 2007, J. Phys. B **40**, F223.
Moses, S. A., *et al.*, 2023, Phys. Rev. X **13**, 041052.
Murphy, T. J., and C. M. Surko, 1992, Phys. Rev. A **46**, 5696.
Nagai, T., and H. Fukuyama, 1982, J. Phys. Soc. Jpn. **51**, 3431.
Nam, Y. S., E. B. Jones, and R. Blümel, 2014, Phys. Rev. A **90**, 013402.
Nath, R., M. Dalmonte, A. W. Glaetzle, P. Zoller, F. Schmidt-Kaler, and R. Gerritsma, 2015, New J. Phys. **17**, 065018.
Niedermeyer, J. F., *et al.*, 2025, arXiv:2512.08037.
Nigmatullin, R., A. del Campo, G. De Chiara, G. Morigi, M. B. Plenio, and A. Retzker, 2016, Phys. Rev. B **93**, 014106.
Noguchi, A., Y. Shikano, K. Toyoda, and S. Urabe, 2014, Nat. Commun. **5**, 3868.
Ogata, S., and S. Ichimaru, 1987, Phys. Rev. A **36**, 5451.
Ohira, R., S. Kume, K. Takayama, S. Muralidharan, H. Takahashi, and K. Toyoda, 2021, Phys. Rev. A **103**, 012612.
Okada, K., T. Takayanagi, M. Wada, S. Ohtani, and H. A. Schuessler, 2009, Phys. Rev. A **80**, 043405.
Okada, K., M. Wada, T. Takayanagi, S. Ohtani, and H. A. Schuessler, 2010, Phys. Rev. A **81**, 013420.
Oshikawa, M., 2000, Phys. Rev. B **61**, 3430.
Ostendorf, A., C. B. Zhang, M. A. Wilson, D. Offenberg, B. Roth, and S. Schiller, 2006, Phys. Rev. Lett. **97**, 243005.
Pagano, G., *et al.*, 2018, Quantum Sci. Technol. **4**, 014004.
Partner, H. L., R. Nigmatullin, T. Burgermeister, K. Pyka, J. Keller, A. Retzker, M. B. Plenio, and T. E. Mehlstäubler, 2013, New J. Phys. **15**, 103013.
Paul, W., and H. Steinwedel, 1953, Z. Naturforsch. A **8**, 448.
Pedregosa-Gutierrez, J., C. Champenois, M. R. Kamsap, G. Hagel, M. Houssin, and M. Knoop, 2018, J. Mod. Opt. **65**, 529.
Pham, J. H., J. Y. Z. Jee, A. Rischka, M. J. Biercuk, and R. N. Wolf, 2024, Adv. Quantum Technol. **7**, 2400086.
Phillips, E. S., R. J. Hendricks, A. M. Abdulla, H. Ohadi, D. R. Crick, K. Koo, D. M. Segal, and R. C. Thompson, 2008, Phys. Rev. A **78**, 032307.
Phillips, W. D., 1998, Rev. Mod. Phys. **70**, 721.
Piacente, G., F. M. Peeters, and J. J. Betouras, 2004, Phys. Rev. E **70**, 036406.
Piacente, G., I. V. Schweigert, J. J. Betouras, and F. M. Peeters, 2004, Phys. Rev. B **69**, 045324.
Podolsky, D., E. Shimshoni, G. Morigi, and S. Fishman, 2016, Phys. Rev. X **6**, 031025.
Podolsky, D., E. Shimshoni, P. Silvi, S. Montangero, T. Calarco, G. Morigi, and S. Fishman, 2014, Phys. Rev. B **89**, 214408.
Poindron, A., J. Pedregosa-Gutierrez, and C. Champenois, 2023, Phys. Rev. A **108**, 013109.
Pollock, E. L., and J. P. Hansen, 1973, Phys. Rev. A **8**, 3110.
Porras, D., and J. I. Cirac, 2004, Phys. Rev. Lett. **93**, 263602.
Potekhin, A. Y., and G. Chabrier, 2000, Phys. Rev. E **62**, 8554.
Poulsen, G., Y. Miroshnychenko, and M. Drewsen, 2012, Phys. Rev. A **86**, 051402.
Prestage, J. D., G. J. Dick, and L. Maleki, 1989, J. Appl. Phys. **66**, 1013.
Prestage, J. D., A. Williams, L. Maleki, M. J. Djomehri, and E. Harabetian, 1991, Phys. Rev. Lett. **66**, 2964.
Pruttivarasin, T., M. Ramm, I. Talukdar, A. Kreuter, and H. Häffner, 2011, New J. Phys. **13**, 075012.
Puebla, R., R. Nigmatullin, T. E. Mehlstäubler, and M. B. Plenio, 2017, Phys. Rev. B **95**, 134104.
Pyka, K., *et al.*, 2013, Nat. Commun. **4**, 2291.
Qiao, M., *et al.*, 2022, arXiv:2204.07283.

Raizen, M. G., J. M. Gilligan, J. C. Bergquist, W. M. Itano, and D. J. Wineland, 1992, Phys. Rev. A **45**, 6493.
Ramm, M., T. Pruttivarasin, and H. Häffner, 2014, New J. Phys. **16**, 063062.
Retzker, A., R. C. Thompson, D. M. Segal, and M. B. Plenio, 2008, Phys. Rev. Lett. **101**, 260504.
Richerme, P., 2016, Phys. Rev. A **94**, 032320.
Richter, S., S. Wolf, J. von Zanthier, and F. Schmidt-Kaler, 2021, Phys. Rev. Lett. **126**, 173602.
Roos, C. F., A. Alberti, D. Meschede, P. Hauke, and H. Häffner, 2017, Phys. Rev. Lett. **119**, 160401.
Roos, C. F., D. Leibfried, A. Mundt, F. Schmidt-Kaler, J. Eschner, and R. Blatt, 2000, Phys. Rev. Lett. **85**, 5547.
Roos, C. F., T. Monz, K. Kim, M. Riebe, H. Häffner, D. F. V. James, and R. Blatt, 2008, Phys. Rev. A **77**, 040302.
Rosenband, T., *et al.*, 2008, Science **319**, 1808.
Roßnagel, J., K. N. Tolazzi, F. Schmidt-Kaler, and K. Singer, 2015, New J. Phys. **17**, 045004.
Rüffert, L.-A., E. A. Dijck, L. Timm, J. R. C. López-Urrutia, and T. E. Mehlstäubler, 2024, Phys. Rev. A **110**, 063110.
Ruiz, A., D. Alonso, M. B. Plenio, and A. del Campo, 2014, Phys. Rev. B **89**, 214305.
Ruster, T., H. Kaufmann, M. A. Luda, V. Kaushal, C. T. Schmiegelow, F. Schmidt-Kaler, and U. G. Poschinger, 2017, Phys. Rev. X **7**, 031050.
Sachdev, S., 2011, *Quantum Phase Transitions*, 2nd ed. (Cambridge University Press, Cambridge, England).
Safavi-Naini, A., R. J. Lewis-Swan, J. G. Bohnet, M. Gärttner, K. A. Gilmore, J. E. Jordan, J. Cohn, J. K. Freericks, A. M. Rey, and J. J. Bollinger, 2018, Phys. Rev. Lett. **121**, 040503.
Saha, S., M. Shalaev, J. O'Reilly, I. Goetting, G. Toh, A. Kalakuntla, Y. Yu, and C. Monroe, 2025, Nat. Commun. **16**, 2533.
Samanta, A., E. Shimshoni, and D. Podolsky, 2022, Phys. Rev. B **106**, 035154.
Sarkar, S., L. Franke, N. Grivas, and M. Garst, 2023, Phys. Rev. B **108**, 235126.
Sawyer, B. C., J. W. Britton, and J. J. Bollinger, 2014, Phys. Rev. A **89**, 033408.
Sawyer, B. C., J. W. Britton, A. C. Keith, C.-C. J. Wang, J. K. Freericks, H. Uys, M. J. Biercuk, and J. J. Bollinger, 2012, Phys. Rev. Lett. **108**, 213003.
Schiffer, J. P., 1993, Phys. Rev. Lett. **70**, 818.
Schiffer, J. P., 2003, J. Phys. B **36**, 511.
Schiffer, J. P., M. Drewsen, J. S. Hangst, and L. Hornekaer, 2000, Proc. Natl. Acad. Sci. U.S.A. **97**, 10697.
Schindler, P., *et al.*, 2013, New J. Phys. **15**, 123012.
Schmid, F., J. Weitenberg, J. Moreno, T. W. Hänsch, T. Udem, and A. Ozawa, 2022, Phys. Rev. A **106**, L041101.
Schmidt, J., A. Lambrecht, P. Weckesser, M. Debatin, L. Karpa, and T. Schaetz, 2018, Phys. Rev. X **8**, 021028.
Schmidt, P. O., T. Rosenband, C. Langer, W. M. Itano, J. C. Bergquist, and D. J. Wineland, 2005, Science **309**, 749.
Schmidt-Kaler, F., J. Eschner, G. Morigi, C. F. Roos, D. Leibfried, A. Mundt, and R. Blatt, 2001, Appl. Phys. B **73**, 807.
Schmied, R., J. H. Wesenberg, and D. Leibfried, 2009, Phys. Rev. Lett. **102**, 233002.
Schneider, C., D. Porras, and T. Schaetz, 2012, Rep. Prog. Phys. **75**, 024401.
Schulz, H. J., 1993, Phys. Rev. Lett. **71**, 1864.
Schwerdt, D., *et al.*, 2024, Phys. Rev. X **14**, 041017.
Serafini, A., A. Retzker, and M. B. Plenio, 2009, New J. Phys. **11**, 023007.
Shamai, I., and D. Podolsky, 2018, arXiv:1801.08131.
Shankar, A., E. Jordan, K. A. Gilmore, A. Safavi-Naini, J. J. Bollinger, and M. J. Holland, 2019, Phys. Rev. A **99**, 023409.
Shankar, A., C. Tang, M. Affolter, K. Gilmore, D. H. E. Dubin, S. Parker, M. J. Holland, and J. J. Bollinger, 2020, Phys. Rev. A **102**, 053106.
Shapir, I., A. Hamo, S. Pecker, C. P. Moca, O. Legeza, G. Zarand, and S. Ilani, 2019, Science **364**, 870.
Shimshoni, E., G. Morigi, and S. Fishman, 2011a, Phys. Rev. A **83**, 032308.
Shimshoni, E., G. Morigi, and S. Fishman, 2011b, Phys. Rev. Lett. **106**, 010401.
Silvi, P., T. Calarco, G. Morigi, and S. Montangero, 2014, Phys. Rev. B **89**, 094103.
Silvi, P., G. De Chiara, T. Calarco, G. Morigi, and S. Montangero, 2013, Ann. Phys. (Berlin) **525**, 827.
Silvi, P., G. Morigi, T. Calarco, and S. Montangero, 2016, Phys. Rev. Lett. **116**, 225701.
Slattery, W. L., G. D. Doolen, and H. E. DeWitt, 1982, Phys. Rev. A **26**, 2255.
Slodička, L., G. Hétet, N. Röck, P. Schindler, M. Hennrich, and R. Blatt, 2013, Phys. Rev. Lett. **110**, 083603.
Solaro, C., S. Meyer, K. Fisher, J. C. Berengut, E. Fuchs, and M. Drewsen, 2020, Phys. Rev. Lett. **125**, 123003.
Sosnova, K., A. Carter, and C. Monroe, 2021, Phys. Rev. A **103**, 012610.
Splatt, F. E., 2009, Ph.D. thesis (University of Innsbruck).
Stenholm, S., 1986, Rev. Mod. Phys. **58**, 699.
Stern, F., 1967, Phys. Rev. Lett. **18**, 546.
Stutter, G., P. Hrmo, V. Jarlaud, M. K. Joshi, J. F. Goodwin, and R. C. Thompson, 2018, J. Mod. Opt. **65**, 549.
Szymanski, B., R. Dubessy, B. Dubost, S. Guibal, J.-P. Likforman, and L. Guidoni, 2012, Appl. Phys. Lett. **100**, 171110.
Taketani, B. G., T. Fogarty, E. Kajari, T. Busch, and G. Morigi, 2014, Phys. Rev. A **90**, 012312.
Tamura, M., T. Mukaiyama, and K. Toyoda, 2020, Phys. Rev. Lett. **124**, 200501.
Tan, J. N., J. J. Bollinger, B. Jelenkovic, and D. J. Wineland, 1995, Phys. Rev. Lett. **75**, 4198.
Tang, C., A. Shankar, D. Meiser, D. H. E. Dubin, J. J. Bollinger, and S. E. Parker, 2021, Phys. Rev. A **104**, 023325.
Tarnas, J. D., Y. S. Nam, and R. Blümel, 2013, Phys. Rev. A **88**, 041401.
Taylor, J. M., and T. Calarco, 2008, Phys. Rev. A **78**, 062331.
Thomas, H., G. E. Morfill, V. Demmel, J. Goree, B. Feuerbacher, and D. Möhlmann, 1994, Phys. Rev. Lett. **73**, 652.
Thompson, R. C., 2015, Contemp. Phys. **56**, 63.
Timm, L., L. A. Rüffert, H. Weimer, L. Santos, and T. E. Mehlstäubler, 2021, Phys. Rev. Res. **3**, 043141.
Timm, L., H. Weimer, L. Santos, and T. E. Mehlstäubler, 2020, Phys. Rev. Res. **2**, 033198.
Timm, L., H. Weimer, L. Santos, and T. E. Mehlstäubler, 2023, Phys. Rev. B **108**, 134302.
Tofful, A., *et al.*, 2024, Metrologia **61**, 045001.
Torrisi, S. B., J. W. Britton, J. G. Bohnet, and J. J. Bollinger, 2016, Phys. Rev. A **93**, 043421.
Totsuji, H., T. Kishimoto, C. Totsuji, and K. Tsuruta, 2002, Phys. Rev. Lett. **88**, 125002.
Ulm, S., *et al.*, 2013, Nat. Commun. **4**, 2290.
Urban, E., N. Glikin, S. Mouradian, K. Krimmel, B. Hemmerling, and H. Häffner, 2019, Phys. Rev. Lett. **123**, 133202.
[Usov, N. A., Y. B. Grebenschikov, and F. R. Ulinich, 1980, Zh. Eksp. Teor. Fiz. **78**, 296 [Sov. Phys. JETP **51**, 148 (1980)].
Van Horn, H. M., 1991, Science **252**, 384.

Vanossi, A., N. Manini, M. Urbakh, S. Zapperi, and E. Tosatti, 2013, Rev. Mod. Phys. **85**, 529.
Van Winkle, D. H., and C. A. Murray, 1986, Phys. Rev. A **34**, 562.
Vogel, M., 2018, *Particle Confinement in Penning Traps—An Introduction* (Springer, New York).
Vybornyi, I., L. S. Dreissen, D. Kiesenhofer, H. Hainzer, M. Bock, T. Ollikainen, D. Vadlejch, C. F. Roos, T. E. Mehlstäubler, and K. Hammerer, 2023, PRX Quantum **4**, 040346.
Waki, I., S. Kassner, G. Birkl, and H. Walther, 1992, Phys. Rev. Lett. **68**, 2007.
Wang, C.-C. J., A. C. Keith, and J. K. Freericks, 2013, Phys. Rev. A **87**, 013422.
Wang, Y., *et al.*, 2020, Adv. Quantum Technol. **3**, 2000068.
Wigner, E., 1934, Phys. Rev. **46**, 1002.
Wineland, D. J., J. C. Bergquist, W. M. Itano, J. J. Bollinger, and C. H. Manney, 1987, Phys. Rev. Lett. **59**, 2935.
Wineland, D. J., and W. M. Itano, 1979, Phys. Rev. A **20**, 1521.
Wipfli, O., H. F. Passagem, C. Fischer, M. Grau, and J. P. Home, 2023, Rev. Sci. Instrum. **94**, 083204.
Wolf, R. N., J. H. Pham, J. Y. Z. Jee, A. Rischka, and M. J. Biercuk, 2024, Phys. Rev. Appl. **21**, 054067.
Wu, Q., Y. Shi, and J. Zhang, 2023, Phys. Rev. Res. **5**, 023022.
Wunderlich, C., G. Morigi, and D. Reiß, 2005, Phys. Rev. A **72**, 023421.
Yannouleas, C., and U. Landman, 2007, Rep. Prog. Phys. **70**, 2067.
Yin, J., and J. Javanainen, 1995, Phys. Rev. A **51**, 3959.
Zawierucha, M. J., T. Rehmert, J. Keller, T. E. Mehlstäubler, P. O. Schmidt, and F. Wolf, 2024, Phys. Rev. A **110**, 013107.
Zhang, J., B. T. Chow, S. Ejtemaee, and P. C. Haljan, 2023, npj Quantum Inf. **9**, 68.
Zurek, W. H., 1985, Nature (London) **317**, 505.